LASER
& PHOTONICS
REVIEWS

Laser Photonics Rev. **9,** No. 2, 129–171 (2015) / **DOI** 10.1002/lpor.201400181

Abstract The generation of sub-optical-cycle, carrier–envelope phase-stable light pulses is one of the frontiers of ultrafast optics. The two key ingredients for sub-cycle pulse generation are bandwidths substantially exceeding one octave and accurate control of the spectral phase. These requirements are very challenging to satisfy with a single laser beam, and thus intense research activity is currently devoted to the coherent synthesis of pulses generated by separate sources. In this review we discuss the conceptual schemes and experimental tools that can be employed for the generation, amplification, control, and combination of separate light pulses. The main techniques for the spectrotemporal characterization of the synthesized fields are also described. We discuss recent implementations of coherent waveform synthesis: from the first demonstration of a single-cycle optical pulse by the addition of two pulse trains derived from a fiber laser, to the coherent combination of the outputs from optical parametric chirped-pulse amplifiers.

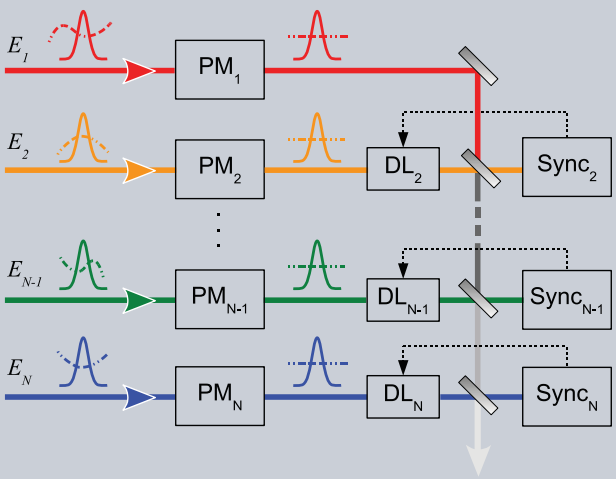

REVIEW ARTICLE

Coherent pulse synthesis: towards sub-cycle optical waveforms

Cristian Manzoni[1,*], Oliver D. Mücke[2], Giovanni Cirmi[2], Shaobo Fang[2,3], Jeffrey Moses[4], Shu-Wei Huang[5], Kyung-Han Hong[6], Giulio Cerullo[1], and Franz X. Kärtner[2,6]

1. Introduction

The availability of light pulses with the shortest possible duration is of the greatest interest from both fundamental and applied standpoints. Since the invention of the laser and the discovery of mode locking [1, 2], there has been a constant effort directed at the generation of ever-shorter light pulses, in a quest to approach (and overcome) the limit set by the period of the optical carrier wave. The two key ingredients for a short light pulse are broad bandwidth, dictated by the Fourier theorem, and accurate control of the dispersion, i.e. of the relative arrival time of the different frequency components, so as to achieve transform-limited (TL) pulse widths. Already in the 1980s, it was possible to generate ultrabroadband nearly TL pulses, comprising just a few cycles of the carrier wave under the envelope [3]. Nowadays few-optical-cycle pulses are routinely produced by different means: directly from the laser oscillator [4, 5], by nonlinear spectral broadening in a guiding medium [6–8], by filamentation in gases and concomitant pulse self-compression [9–12], or by optical parametric amplifiers (OPAs) [13, 14]. All these sources have been carefully optimized and have reached their optimum performance in terms of bandwidth and dispersion compensation; further significant improvements in pulse duration appear therefore unlikely. The best strategy for a significant increase in bandwidth, allowing one to shorten the pulse duration reaching and overcoming the single-cycle limit, appears therefore to be coherent combination, or synthesis, of pulses with different colors generated from separate sources.

When the light pulse duration approaches a single optical cycle, not only the pulse envelope, which is connected to its intensity profile, but also the carrier wave becomes of key importance in determining its interaction with matter [15]. Generation of optical pulses with predetermined electric field $E(t)$ calls for the control of the phase of the carrier wave with respect to the envelope, called the carrier–envelope phase (CEP), which has become technically feasible in the past decade [16, 17]. CEP control enables one to generate light pulses for which the electric (and magnetic) field is a precise, user-defined function of time, and thus to extend the concept of a waveform generator, which

[1] IFN-CNR, Dipartimento di Fisica, Politecnico di Milano, Piazza Leonardo da Vinci 32, 20133, Milan, Italy
[2] Center for Free-Electron Laser Science, Deutsches Elektronen-Synchrotron DESY and Hamburg Center for Ultrafast Imaging, Notkestraße 85, 22607, Hamburg, Germany
[3] Beijing National Laboratory for Condensed Matter Physics, Institute of Physics, Chinese Academy of Sciences, Beijing 100190, China
[4] School of Applied and Engineering Physics, Cornell University, Ithaca, NY, 14853, USA
[5] Optical Nanostructures Laboratory, Center for Integrated Science and Engineering, Solid-State Science and Engineering, and Mechanical Engineering, Columbia University, New York, NY, 10027, USA
[6] Department of Electrical Engineering and Computer Science and Research Laboratory of Electronics, MIT, Cambridge, MA, USA
*Corresponding author: e-mail: cristian.manzoni@polimi.it

is commonplace at radio frequencies, to the optical domain, entering the era of optical waveform electronics. An electronic waveform generator is a device which produces a prescribed electric waveform, i.e. a time-varying voltage or current, and works on the (sub-)nanosecond timescale, i.e. over bandwidths up to tens of gigahertz. An optical waveform generator aims at scaling this concept to the femtosecond timescale of the light-field oscillation, corresponding to petahertz bandwidths.

The generation of ever-shorter CEP-controlled light pulses, corresponding to bursts of the electric field lasting less than one optical cycle, is of great interest not only because it overcomes a technological barrier, but also because it allows one to enter a completely new regime of light–matter interaction. The emerging field of "waveform nonlinear optics" [18,19] aims at the study and control of the nonlinear interaction of matter with extremely short optical waveforms, having an electric field profile custom-tailored within an optical cycle of light. Several new applications arise in strong-field physics, the most relevant of which are related to high-harmonic generation (HHG) and to the generation of intense isolated attosecond extreme ultraviolet (XUV) pulses [20, 21]. According to the three-step model of HHG [22–24], within an optical cycle electrons are: (i) removed by tunneling from an atom or molecule; (ii) accelerated in the continuum by the laser electric field; and (iii) driven back to the parent ion in order to generate an XUV continuum via recombination into the ground state. The capability to tailor the electric field waveform at the sub-cycle level enables control of both the tunnel ionization step and the motion of the electron in the continuum, and thus its kinetic energy and the energy cutoff extent of the XUV emission, realizing the so-called "perfect waveform" for HHG [25–27]; most importantly, it allows one to limit the electron tunneling–recollision process to one event per driving pulse, resulting in the emission of a single XUV continuum corresponding to an isolated attosecond pulse (IAP) [28, 29]. The extension of the energy cutoff and the development of chirped mirrors in the XUV spectral range [30] allow one to reduce the duration of the IAP. Typically IAPs are generated by spectrally filtering the HHG cutoff radiation or by using gating techniques [31], leading to limitations of the generated IAP pulse energy. The availability of a synthesized optical waveform with sub-cycle control would allow the generation of IAPs without the use of any gating techniques, and thus to significantly increase their energy, as demonstrated in recent experiments [20, 21].

If suitably scaled in energy [32], the synthesized sub-cycle waveforms could be used to drive relativistic laser–plasma interactions and laser wakefield electron acceleration, which produces quasi-monoenergetic electron bunches with orders of magnitude higher accelerating gradients and much shorter electron pulses than standard radio-frequency accelerators [33–35]. Such electron pulses, with energy reaching the multi-GeV range, can be used to drive table-top ultrashort X-ray sources with unprecedented brilliance and to probe photoinduced dynamics by ultrafast electron/X-ray diffraction. A strong longitudinal electric field can be obtained by tightly focusing a radially polarized (TM01) ultrashort laser pulse [36,37]: in a low-density gas and at high laser intensities, this field accelerates the electrons along the propagation axis, while the transverse field components (electric and magnetic) help to maintain the particles close to the beam propagation axis. The intensity of the resulting longitudinal field strongly depends upon the peak power of the pulse, the laser wavelength, and the numerical aperture of the focusing optics [38].

The same (sub-)femtosecond control of the motion of photoemitted electrons can be extended from the gas phase to the solid state, and in particular to metal nanostructures. Sharp metal nanotips illuminated with CEP-controlled optical waveforms can generate attosecond electron wavepackets localized on the scale of a few nanometers [39–41], enabling novel applications in time-resolved electron microscopy and diffraction. Another fascinating application of optical waveforms is the control of electric currents in semiconductors [42] and insulators on the sub-cycle scale, which may have promise in extending the signal processing capabilities of electronic devices up to the petahertz range, by reversibly switching a semiconductor or insulator into a metal on the timescale of the optical period [43–45].

Tailored optical waveforms can also be applied to the generation and control of electronic coherences in molecules and atoms [46]. Sub-femtosecond temporal confinement of the ionization process allows launching with unprecedented accuracy valence electron wavepackets [47], whose dynamics can be followed by a synchronized IAP. This capability has already been demonstrated in pioneering experiments, in which a sub-cycle pulse was used to field-ionize krypton atoms within a single half-cycle and launch an electron wavepacket into a valence-shell orbit with a well-defined initial phase [48]. Half-cycle field excitation and attosecond probing reveal fine details of atomic-scale electron motion, such as the instantaneous rate of tunneling, the initial charge distribution of a valence-shell wavepacket, the attosecond dynamic shift (instantaneous ac Stark shift) of its energy levels, and its few-femtosecond coherent oscillations.

The broad range of applications presented in the previous paragraphs strongly motivates the efforts aimed at the synthesis of ultrabroadband, sub-cycle optical waveforms. In this paper we review the basic principles and the current state of the art of coherent optical waveform synthesis. In particular, we focus on the work aiming at synthesizing an optical waveform with a continuous spectrum, which corresponds, in the time domain, to an isolated pulse (within of course the repetition rate of the laser). One should however mention significant related research efforts aimed at synthesizing optical waveforms, which are not covered in this review because they do not give rise to isolated pulses but rather to high-repetition-rate pulse trains. Due to their relevance, these techniques are briefly described in the next section, devoted to the main conceptual schemes for waveform synthesis.

The paper is organized as follows. In Section 2 we review the main conceptual approaches to waveform synthesis. Section 3 discusses the experimental tools required for coherent synthesis, giving details of various techniques

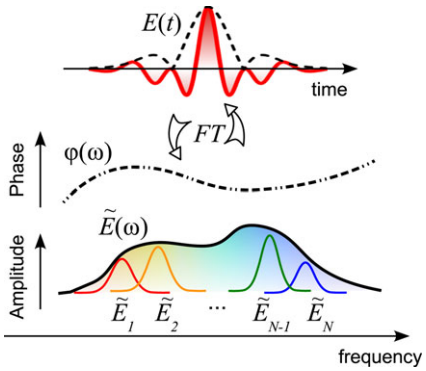

Figure 1 Representation of a pulse in time and frequency domain. The spectrum $\tilde{E}(\omega)$, obtained by Fourier transform (FT), can be seen as superposition of narrow sub-bands $\tilde{E}_i(\omega)$, a concept at the core of coherent waveform synthesis.

for the control of pulse relative delay and CEP, and the tailoring of their spectral phase. Section 4 is devoted to the main techniques for the temporal characterization of ultrashort pulses, applied to the synthesized electric fields. Section 5 presents various practical implementations of coherent waveform synthesis: from the first demonstration of an isolated single-cycle optical pulse by addition of two pulse trains derived from the same fiber laser, to the coherent combination of the outputs from ultrabroadband optical parametric chirped-pulse amplifiers (OPCPAs).

2. Paradigms of waveform synthesis

As we suggested in the previous section, one promising strategy for shortening the duration of light pulses is coherent combination, or synthesis, of longer pulses from separate sources. At first sight, it may appear paradoxical that the overlap of multiple longer signals leads to a shorter one; this effect can be understood considering the wave description of light, supported by the mathematical tool of Fourier transform. On the one hand, indeed, the wave approach benefits from the concept of interference, which depicts a light pulse as the result of constructive interference between waves at different frequencies; in this sense, overlap of several pulses with different carrier frequencies may further reduce their constructive interaction to shorter time intervals, thus resulting in a shorter light transient. On the other hand, as depicted in Fig. 1, any signal $E(t)$ is associated with a complex spectrum $\tilde{E}(\omega)$ in the reciprocal frequency domain, such that

$$E(t) = \int_{-\infty}^{+\infty} \tilde{E}(\omega)\, \mathrm{e}^{j\omega t}\, \mathrm{d}\omega = \int_{-\infty}^{+\infty} |\tilde{E}(\omega)|\, \mathrm{e}^{j\varphi(\omega)} \cdot \mathrm{e}^{j\omega t}\, \mathrm{d}\omega. \quad (1)$$

This equation, the inverse Fourier transform or Fourier integral, states that any signal, even those extending over a limited time domain, can be seen as the coherent overlap of infinitely long time-domain sinusoids or cosinusoids, with weight and phase given by the complex function $\tilde{E}(\omega)$. The duration of the synthesized signal, i.e. the time interval over which constructive interference occurs, depends on two important parameters: (i) it is inversely related to the amount of interacting waves, namely the bandwidth; and (ii) it is strongly affected by the relative phase of each component, i.e. by the spectral phase $\varphi(\omega)$. The spectral phase is particularly relevant, since it can be shown that for a given bandwidth the shortest pulse is achieved only when the spectral phase is linear with frequency, which happens when the phase shift between two adjacent components is constant. Figure 1 also shows that the spectrum can be seen as the overlap of separate narrower sub-bands $\tilde{E}_i(\omega)$, so that

$$\begin{aligned}\tilde{E}(\omega) &= \tilde{E}_1(\omega) + \tilde{E}_2(\omega) + \cdots + \tilde{E}_N(\omega) \\ &= |\tilde{E}_1(\omega)|\, \mathrm{e}^{j\varphi_1(\omega)} + |\tilde{E}_2(\omega)|\, \mathrm{e}^{j\varphi_2(\omega)} \\ &\quad + \cdots + |\tilde{E}_N(\omega)|\, \mathrm{e}^{j\varphi_N(\omega)}. \end{aligned} \quad (2)$$

Due to the linearity of the Fourier transform operator, this also means that

$$E(t) = E_1(t) + E_2(t) + \cdots + E_N(t), \quad (3)$$

where each transient $E_i(t)$, corresponding to $\tilde{E}_i(\omega)$, may be significantly longer than the overall synthesized field $E(t)$. Equations (2) and (3) naturally introduce the concept of pulse synthesis as coherent superposition of longer signals in different spectral sub-bands. In combination with Fig. 1 they also clarify some of the main prerequisites for coherent waveform synthesis:

1. Since ultrashort waveforms can be obtained only from broadband spectra, the parent sub-bands need to span *a wide spectral region*; the sub-bands may be narrowband, and not necessarily adjacent. As a consequence, broadband waveform synthesis requires the combination of *several sources* providing the set of parent sub-bands.
2. The spectral phases of the sub-bands must be suitably stitched together, which requires *phase manipulation* techniques. Among the various aspects of phase manipulation, we also include the challenging issue of *synchronization*, which is required to compensate for any relative delay accumulated by the parent sub-bands.

The simple concept expressed by Eq. (1) is also at the core of mode-locked operation of lasers [1,2,49]. The ultrashort pulses emitted from mode-locked lasers result from the superposition of a large number of fields $\tilde{E}_i(\omega)$; each of them is a monochromatic cavity mode, with suitably locked phase (hence the name "mode locking"). In addition, the pulse train emitted by mode-locked lasers is at a constant repetition rate, imposed by the cavity round-trip time. This is in accordance with another property of the Fourier operator: any periodic function $E(t)$ can be represented by a series of discrete sinusoidal functions having integrally related frequencies and fixed phase relationships. In a mode-locked laser the discrete modes are defined by the

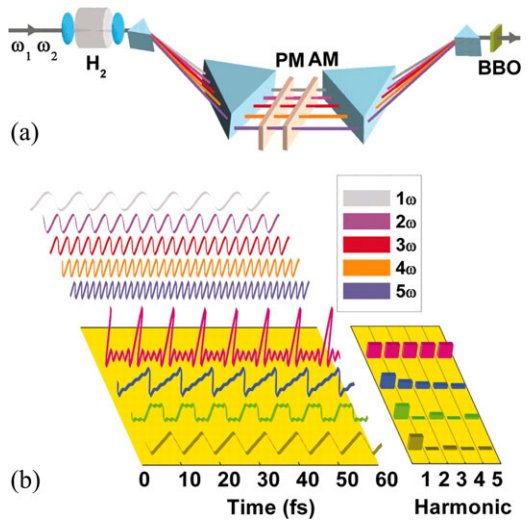

Figure 2 (a) Experimental scheme for the generation and manipulation of discrete harmonics from the H_2 cell. AM and PM: liquid crystal spatial light modulators for the modulation of the amplitude and phase of each harmonic; BBO: β-barium borate crystal that mixes the harmonics to produce heterodyne signals used to adjust the phases and to set the CEP. (b) Pictorial demonstration of ultrafast waveforms (below) obtained by the coherent superposition of the harmonics (above). The panel at lower right depicts the spectral field amplitudes corresponding to the waveforms on the left. Image from [55].

Fabry–Pérot resonances of the cavity, while the phase relationship is imposed by the nonlinearities triggering the mode-locked regime; the spacing between the discrete modes is typically of the order of 10–100 MHz. The pulse duration depends on the number of amplified cavity modes, which is mainly imposed by the bandwidth of the gain medium; sub-cycle pulses can be obtained if the bandwidth spans more than one octave [50]. The operation of mode-locked lasers suggests that one route for the generation of a train of ultrashort pulses is the coherent combination of a series of sine (cosine) waves with constant frequency spacing. One alternative way of generating such a comb of frequencies is via molecular modulation, which consists of driving a molecular medium with two narrowband pulses with frequency difference matching a specific vibrational transition, and generating a series of cascaded Stokes and anti-Stokes Raman sidebands [51,52]. By using two driving pulses with commensurate frequencies, i.e. both exact multiples of the molecular vibration ω_0, one obtains a comb of frequencies $\omega_n = n\omega_0$, leading to a train of pulses with constant CEP [53]. In the case of the H_2 molecule, 3.5 ns pulses at 2.406 μm and at its second harmonic are used to drive the Q(1) band in a cell at 1 bar, generating a commensurate comb of higher-order harmonics [54]. By manipulating independently, with suitable modulators, the amplitudes and phases of five discrete harmonics spanning from the mid-IR to the blue (see Fig. 2), it is possible to synthesize optical fields in the shape of squares, sawtooths, and sub-cycle sine and cosine pulses, at a repetition rate of 125 THz [55].

A further upgrade of this system is a compact all-solid-state optical waveform generator, consisting of a segmented periodically poled lithium tantalate crystal, with a sequence of poling periods allowing the cascaded generation of higher-order harmonics up to the fifth, followed by an acousto-optic programmable dispersive filter introducing independent control of the amplitudes and phases of each spectral component [56]. An additional waveform synthesis activity worth mentioning is optical arbitrary waveform generation (OAWG), which combines frequency comb and pulse shaping technologies [57, 58]. The idea is to shape individually, in amplitude and phase, all lines of the comb, generated by a mode-locked laser or by a microresonator [59]; this requires a shaper with a spectral resolution which is high enough to match the spacing between adjacent comb lines. This allows in principle the generation of a pulse with duration matching the period between successive pulses, i.e. a pulse which "fills time". So far this has been accomplished with static masks [60]; the capability to update the shaper with a repetition rate matching that of the laser would enable one to update the shape for every successive pulse, and thus to generate truly arbitrary optical waveforms [57]. Applications of OAWG are very broad and range from coherent control experiments to high-speed optical communications and LIDARS. In all these examples, the components $\tilde{E}_i(\omega)$ are monochromatic waves with suitable amplitude and phase characteristics. In its general form, Eq. (2) states that $\tilde{E}_i(\omega)$ can be broadband, and $E_i(t)$ can be individual ultrashort pulses. This is the case of coherent synthesis from independent pulsed sources, which is the main subject of this paper. In this case, we can identify two main approaches: the *parallel scheme*, schematically represented in Fig. 3, and the *sequential scheme*, shown in Fig. 4. Both schemes require amplitude (AMP) and phase (PM) manipulation modules, which are arranged in different ways. Typically, the AMP module is an amplification stage, while PM includes spectral phase correction and carrier-phase control.

In the parallel scheme, each sub-band first undergoes amplitude and phase manipulation in separate dedicated modules; subsequently, the channels are delayed through the delay line driven by the synchronization module, and finally they are combined. In the sequential scheme, in contrast, the sub-bands propagate and are manipulated as a whole. The two approaches are used for different applications and exhibit specific trade-offs: the parallel scheme offers the greater flexibility to manipulate the amplitude and phase of each sub-band independently and without constraints given by the other channels. The control of the spectral phase is typically easier when performed over narrower bandwidth: working on many narrowband sub-bands allows a highly accurate tailoring of the spectral shape and phase in each frequency region, which may lead to the synthesis of potentially broader waveforms by combination of many independent channels; as a drawback, since the sub-bands travel over optical paths which may be very different, a synchronization module is required in order to compensate for any relative delay and phase jitter. As we will see in Section 3, both phase and delay jitter must be kept considerably smaller than one optical cycle, which makes

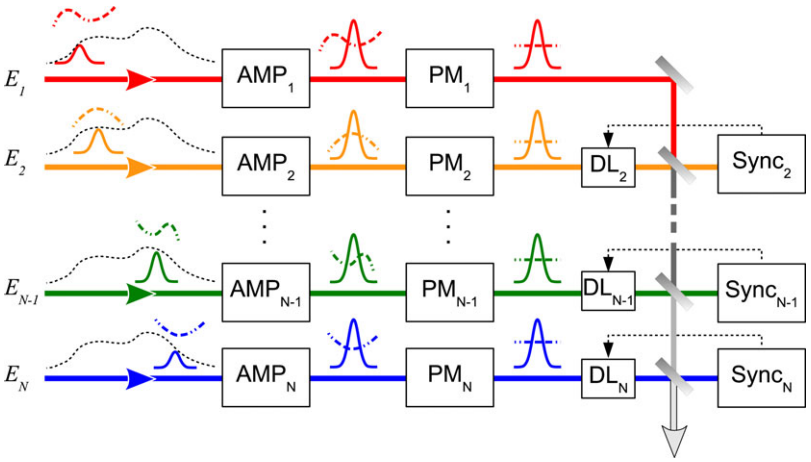

Figure 3 Parallel scheme for pulse synthesis. AMP: amplification module; PM: phase manipulation; DL: delay line; Sync: synchronization module, which detects the time jitter of the pulses and compensates for it through the delay line. The spectral phase is indicated as a dash-dotted line on top of each spectrum.

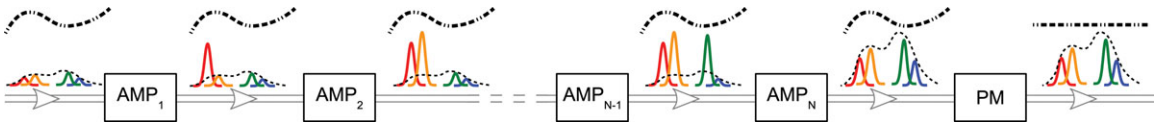

Figure 4 Sequential scheme for pulse synthesis. AMP: amplification module; PM: phase manipulation, schematically condensed in one stage only. The spectral phase is indicated as dash-dotted lines on top of each spectrum.

synchronization particularly challenging. In the sequential scheme, since the sub-pulses travel over a common optical path, they do not accumulate relative time and phase jitters, but only linear dispersion. For this reason, no synchronization module is required; however, phase manipulation needs to be performed on the whole synthesized spectrum, and therefore an ultrabroadband phase compensator is required. This typically limits the achievable bandwidth of sequential schemes significantly below that realizable in parallel schemes; in addition, each AMP stage, although acting only on a limited bandwidth, changes the overall spectral phase, and therefore dispersion control may be required also in between stages to optimize the following steps.

Depending on the properties of the laser source and the synthesized pulse, both approaches have been applied successfully. The parallel approach was applied to the coherent synthesis of pulse trains from independent mode-locked lasers [61–63]; here the cavities acted as AMP and PM modules, while the challenging synchronization of the two sources and the locking of their repetition rates had to be adjusted externally. Alternative schemes start from one master oscillator which defines the repetition rate of the whole system and seeds two independent parallel arms. In [64], for example, each arm generates broadband pulses, which are subsequently manipulated in dedicated AMP and PM modules, and finally synchronized and recombined. Pulse synthesis schemes can be also exploited to manipulate only the spectral phase of an ultrabroadband source; when a high-energy ($> 800\ \mu$J) 25 fs pulse from a Ti:sapphire laser is focused into a hollow-core fiber [6], it generates an ultrabroadband, super-octave spanning spectrum. If the spectral phase is suitably adjusted, this spectrum can support sub-cycle pulse durations. One route to control the spectral phase over the whole bandwidth is to apply the parallel approach: the huge bandwidth is separated into several spectral channels, which are individually compressed by dedicated dispersive delay line PMs and coherently recombined [48]. In this scheme, there are no AMP modules, since neither amplification nor filtering is applied, apart from the attenuation of the strong near-infrared (NIR) part to equalize the spectrum; on the contrary, other schemes may include, in each arm, dedicated amplification modules such as OPAs [65] or OPCPAs [66]. One example of the sequential scheme is the device developed by Morgner's group [67], in which two serial OPAs are used to amplify two different portions of an ultrabroadband seed light; a similar approach at much higher energy and lower repetition rate was reported by Veisz *et al.* [32]. More detailed descriptions of sequential and parallel schemes are provided in Section 5, where we report on the most recent achievements in optical waveform synthesis technology.

3. Requirements for pulse synthesis

In the previous section, we outlined the various approaches for the generation of ultrabroadband waveforms, based on the superposition of different sources covering separate spectral regions. According to Fourier theory, a broad synthesized bandwidth is one of the prerequisites for the generation of ultrashort waveforms. The other parameter is the spectral phase: in the Fourier picture of a light transient, the spectral phase is related to the delay of each frequency component, which strongly influences the temporal profile of the light pulse resulting from the superposition of the components. In Fig. 5, we show the resulting waveforms, if pulses with different colors are combined. The ideal configuration, delivering the shortest pulse, is shown in Fig. 5a; the other

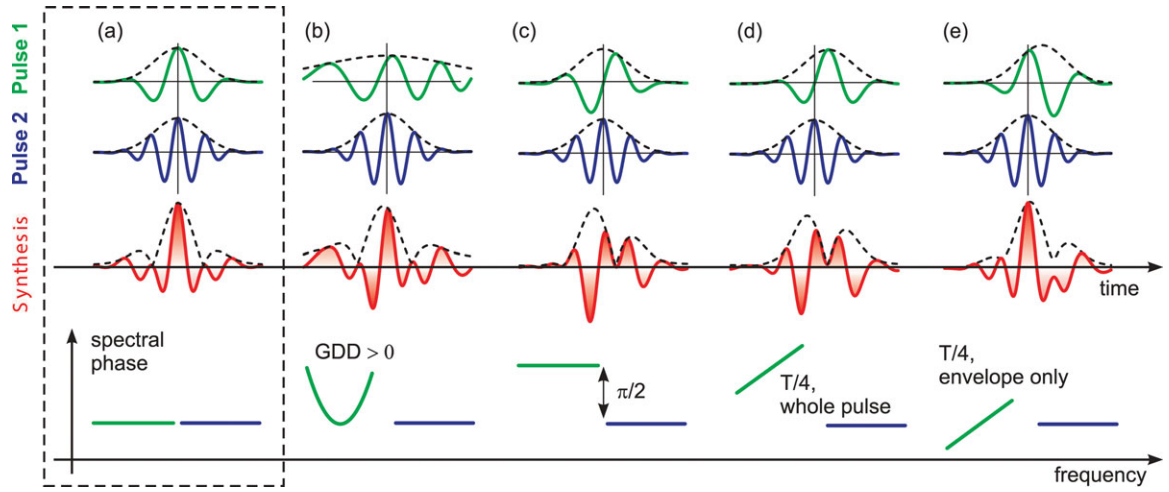

Figure 5 Dependence of the synthesized electric field on the spectral phases of the individual pulses. Top: electric fields $E(t)$ in the time domain; bottom: corresponding spectral phases. In all configurations, only the characteristics of the low-frequency pulse (pulse 1, green line) are changed. (a) The optimum configuration, corresponding to the shortest synthesized waveform, and being a reference for the other configurations. (b) The low-frequency pulse is chirped to three times its TL duration. (c) Pure CEP slip by a quarter of the optical cycle. (d) Delay of the pulse by a quarter of the optical cycle. (e) Pure delay of the envelope by a quarter of the optical cycle.

parts of the figure show the shape of the synthesized waveform for various spectral phases of the low-frequency pulse (green line, upper row): we consider the effect of group-delay dispersion (GDD) (parabolic phase profile, Fig. 5b), pure carrier shift (jump of the spectral phase, Fig. 5c), pulse shift (sloped and up-shifted phase, Fig. 5d), and envelope shift (sloped phase, Fig. 5e). Inspection of the synthesized waveforms reveals that Fig. 5b corresponds to a very long pulse; Fig. 5c and d present very similar dramatic distortions; and Fig. 5e is the closest to the optimal configuration. These examples demonstrate that synthesis of ultrashort pulses calls for careful manipulation of three parameters: (i) the *spectral phase*; (ii) the *carrier phase*; and (iii) the *relative delay* between the sources. These parameters hence deserve accurate discussion, which is provided in the following sections.

The control of the *spectral phase* typically involves techniques which manipulate components extended over large bandwidths; if one of the two pulses is chirped, the resulting synthesized waveform shown in Fig. 5b suggests that short pulses can be synthesized only if the group delay is constant with frequency, corresponding to constant or linear spectral phase and leading to TL pulses.

We now assume that the parent sub-pulses are TL and we discuss the other parameters for optimal pulse synthesis. Since waveform synthesis arises from the interference between the fields of the parent pulses, the manipulation and control of the *carrier phase* is the most important task. In general, the carrier phase of a pulse may be described by two different concepts: the *absolute phase* (AP) and the *CEP*. The AP is the phase of a pulse carrier wave with respect to an absolute frame of reference; the CEP is the phase of the carrier wave with respect to the pulse envelope. The two concepts may look very similar, since the CEP coincides with the AP when the frame of reference is the pulse itself; but in many cases, such as when two or more pulses are superposed, AP and CEP play very different roles. Considering the waveform synthesis process, Fig. 5c,d,e highlight all possible variations of the carrier phase of the low-frequency pulse. In Fig. 5c, we preserve the pulse delay and we apply a CEP shift of $\pi/2$, so that the electric field presents a minimum at time 0; as expected, this affects the interference between the parent pulses, leading to a dramatic deformation of the synthesized pulse. This suggests that minimization of CEP shifts is necessary to produce stable synthesized waveforms; but CEP stabilization alone is not enough, as shown in Fig. 5d. Here we preserve the CEP, but change the relative delay by a quarter of the optical cycle; also in this case, the profile of the synthesized pulse is distorted with respect to the optimal shape. The pulse delay applied in Fig. 5d produces the same AP shift as the pure carrier delay of Fig. 5c: the electric field again presents a minimum at time 0 and this explains why the synthesized waveforms of Fig. 5c and d are very similar. We deduce that it is the carrier shift that influences the synthesized electric field. To confirm this important concept, in the configuration shown in Fig. 5e we apply both a group delay and a CEP shift. Their amount is chosen so that the resulting electric field has a maximum at time 0; the synthesized pulse is now closer to the optimal configuration of Fig. 5a. These examples indicate that coherent pulse synthesis, arising from interference, is mostly influenced by the carriers' shifts, described by their AP: couples of Fig. 5a and e and Fig. 5c and d are very similar because they correspond to pulses with the same AP shift. Locking of the APs of the parent sub-pulses is therefore necessary for coherent waveform synthesis, even though it may not be straightforward. Figure 5c,d,e suggest that AP shift always accompanies CEP or delay drifts; for this reason, control of the AP shift is obtained in practice by locking the CEP and

by controlling the *relative delay*. The accuracy required for both CEP and relative delay is of the order of fractions of the optical cycle. In the following subsections we discuss the techniques to adjust the spectral phase (Section 3.1) and to control the relative delay (Section 3.2) and the CEP (Section 3.3) for full tailoring of the synthesized optical waveforms reaching the transform limit. When the parent pulses have spectral overlap, AP fluctuations can be directly detected using Fourier transform spectral interferometry. This technique is described in Section 4.2.1.

3.1. Control of spectral phase: linear techniques for pulse compression

To describe the spectral and temporal properties of a pulse, it is useful to expand the spectral phase in a Taylor series around the carrier frequency ω_0:

$$\phi(\omega) = \phi(\omega_0) + \phi'(\omega_0)(\omega - \omega_0) + \frac{1}{2}\phi''(\omega_0)(\omega - \omega_0)^2 + \frac{1}{6}\phi'''(\omega_0)(\omega - \omega_0)^3 + \cdots \quad (4)$$

The derivative of the spectral phase with respect to frequency is the *group delay* $\tau_g(\omega) = \mathrm{d}\phi/\mathrm{d}\omega$, which represents the relative arrival time within the pulse of a quasi-monochromatic wavepacket at frequency ω. $D_2 = \phi''(\omega_0)$ is the second-order dispersion or GDD and $D_3 = \phi'''(\omega_0)$ is the third-order dispersion (TOD). Using this expansion, one can express the group delay as

$$\tau_g(\omega) = \phi'(\omega_0) + D_2(\omega - \omega_0) + \frac{1}{2}D_3(\omega - \omega_0)^2 + \ldots \quad (5)$$

When $D_2 = 0, D_3 = 0, \cdots$ one has $\tau_g(\omega) = \text{const.}$, i.e. all the frequency components of the pulse arrive at the simultaneous group delay. In this case the pulse is TL and it has the shortest possible duration compatible with its spectrum. If the dispersion terms are non-zero, the frequency components of the pulse arrive at different times and the pulse is *chirped*. In particular, if $D_2 > 0$ the blue components are delayed with respect to the red ones and the pulse is said to have *positive chirp*, while if $D_2 < 0$ the red components are delayed with respect to the blue ones and the pulse is said to have *negative chirp*. A pulse can acquire second- and third-order dispersion by linear propagation or as a consequence of nonlinear interactions [68,69]. Positive second-order dispersion is accumulated upon propagation in all transparent materials in the visible wavelength range, while it becomes negative (or anomalous) in the NIR (e.g. in fused silica $D_2 < 0$ for $\lambda > 1.3\ \mu$m).

Dispersion control is a key issue in the generation and exploitation of ultrashort pulses. In the anomalous dispersion regime, linear propagation in dispersive materials is sufficient to reach the transform limit, which in the case of ultrabroadband spectra results in few-optical-cycle pulses [70]. In the visible frequency range, where materials provide a positive dispersion, it is important to have optical systems providing negative dispersion, the so-called *pulse compressors*. Some of the systems introduced to manipulate the spectral phase by linear processes are shown in Fig. 6. Table 1 summarizes the performances of some linear dispersion-control schemes, together with their capabilities to produce few-cycle pulses in various spectral regions:

1. A pair of prisms at distance L [71,72]. The angular dispersion of the first prism creates a longer path through the second prism material for red wavelengths with respect to blue ones, thus providing negative dispersion. Single pass in the prism pair introduces spatial dispersion and pulse-front tilt, which can be removed by

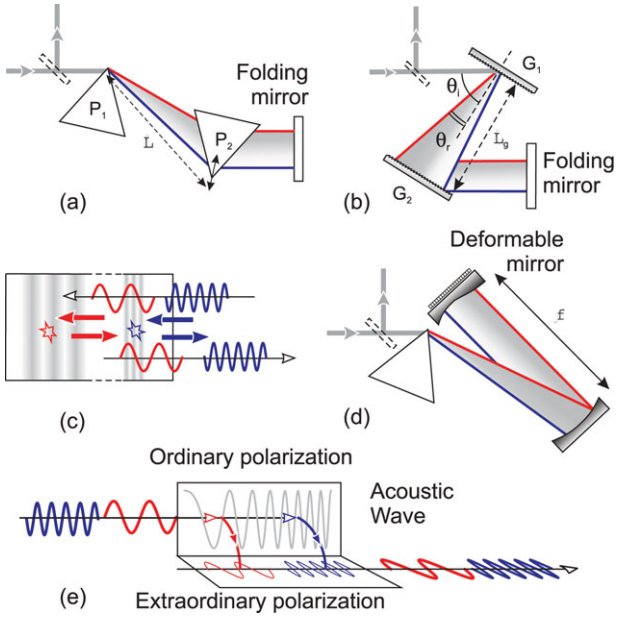

Figure 6 Basic schemes for the manipulation of the spectral phase of a pulse: (a) prism pair; (b) grating pair; (c) chirped mirrors; (d) adaptive pulse shaper, with a deformable mirror in the Fourier plane; (e) acousto-optic programmable dispersive filter.

Table 1 Pulse durations obtained with linear compression systems.

System	Wavelength (μm)	Duration (fs) (cycles)	Ref.
BK7 prism pair	0.55–0.7	14 (6.5)	[73]
Prisms + grating	0.7–1	4.7 (1.7)	[8]
Chirped mirrors	0.5–1.1	4.7 (2)	[83]
Shaper with SLM	0.65–1.1	4.3 (1.6)	[88]
Shaper with DM	1.1–2	8.5 (1.8)	[92]
Shaper with AOM	4.5–5.5	70 (4.2)	[89]
AOPDF	0.58–1.02	5 (2)	[104]

folding the setup in a double-pass configuration. When the prism is Brewster-cut and the beam incidence occurs at the Brewster angle, there is virtually no reflection for the correct linear polarization and the system is essentially loss free. This compressor introduces not only a GDD, but also a large negative TOD, which cannot be independently controlled. Since both D_2 and D_3 are proportional to the prism separation L, the ratio D_3/D_2 is a characteristic of the prism material and the wavelength, and can be minimized by choosing materials with low dispersion (such as fused silica, MgF_2 or CaF_2). In this case, however, the prism distance required to achieve a given value of D_2 increases. For these reasons, the prism pair is a very simple compressor, but cannot be used with very broadband pulses, due to the residual TOD and higher-order dispersion terms. With prism-pair compressors, pulses as short as 14 fs (see Table 1) can routinely be achieved in the visible spectral range [73], resulting as a compromise between pulse bandwidth and residual uncompensated dispersion.

2. A pair of parallel and identical gratings [74]. For an incidence angle θ_i on the grating, the diffracted beam direction is given by the grating equation:

$$\sin\theta_d = \sin\theta_i + m\frac{\lambda}{d}, \tag{6}$$

where d is the grating period and m is the diffraction order. The red frequencies travel a longer path with respect to the blue ones (see Fig. 6b), resulting in negative dispersion. The GDD of a grating pair can be expressed as

$$D_2 = -\frac{m^2\lambda_0^3 L_g}{2\pi^2 c^2 d^2}\frac{1}{[1-(\sin\theta_i + m\lambda_0/d)^2]^{3/2}}, \tag{7}$$

where λ_0 is the carrier wavelength and L_g the grating distance. Also for the grating pair, spatial dispersion can be removed by a double pass after reflection from a folding mirror. Grating pairs provide, for a given separation, much greater dispersion with respect to prism pairs and are thus suitable for introducing large frequency chirps. A grating pair introduces a positive TOD, so that a combined prism–grating compressor can cancel both GDD and TOD [3, 8, 75, 76].

3. *Chirped mirrors* (CMs) [77,78]. These are multilayer dielectric mirrors, consisting of a large number (≈ 50) of alternating low- and high-refractive-index layers, suitably designed so that the layer thickness increases going towards the substrate. In this way, the high-frequency components of the laser spectrum are reflected first, while the low-frequency components penetrate deeper into the multilayer, thus acquiring an additional group delay. Suitable analytical predesigns [79–81] and computer optimization [82] allow one to avoid spurious resonances and to design a custom-tailored frequency-dependent spectral phase; a complete discussion of the recent advances in CM design is reported in [83] and in references therein. CMs have several advantages: the dispersion can be almost arbitrarily controlled over very broad bandwidths (approaching an octave [84] and even more [85]), and their performances are less sensitive to misalignment. On the other hand, their fabrication is not trivial, since very tight tolerances on the layer thicknesses are required, achievable only by sophisticated coating techniques such as ion beam sputtering. In addition, the negative GDD obtainable from a single bounce is typically rather small ($\approx -50\,\mathrm{fs}^2$), so that many bounces are required to achieve the required overall GDD.

4. Adaptive pulse shapers, in which the spectral phase is actively controlled and optimized for the application, including pulse compression. The shaper, sketched in Fig. 6c, is used in the so-called 4-*f* arrangement [86]: after a dispersive element, a lens performs a spatial Fourier transform which converts the angular dispersion to a spatial separation at the back focal plane, where a phase and/or intensity modulator is located. A grating or a prism can be used as a dispersive element, and a spherical mirror avoids chromatic aberrations and dispersion introduced by the lens. Using the 4-*f* arrangement, many different pulse-shaping techniques have been developed in the past, differing in the modulator located in the Fourier plane; in all cases, the modulator can be actively controlled to apply a given phase and amplitude modulation, and therefore these shapers are referred to as programmable. These devices can be based, for example, on liquid crystal spatial light modulators (LC-SLMs) [87, 88], acousto-optic modulators (AOMs) [89, 90], or deformable mirrors (DMs) [91–93], leading to the successful control of the pulse shape in the visible and NIR spectral regions. LC-SLMs are made of a sequence of liquid crystal cells. In the absence of an electric field, the molecules are aligned along the cell surface, which behaves as a birefringent plate; light polarized along the axis of the molecules experiences large refractive index. When an electric field is applied, the molecules get tilted, reducing the birefringence and the refractive index seen by the polarized light. As a result the phase of light transmitted through each cell is controlled by the local electric field; the maximum phase shift introduced by the cell is proportional to the cell thickness. The transmission of LC-SLMs ranges from the ultraviolet [94] to the NIR bands; the discretization introduced by the cell structure produces spurious periodic structures in the transmitted spectrum. In an AOM, a traveling acoustic wave induces a transient refractive index grating which diffracts the light beam; the amplitude and phase of the diffracted beam directly reflect the amplitude and phase of the acoustic wave. AOM-based pulse shapers exhibit transmission from 260 nm [95] to 10 μm [89]. DMs can introduce smooth phase variations by the deformation of a thin membrane or of a semipassive bimorph structure [96]. DMs can be used for phase-only modulation, with the important advantages of high throughput and of being substantially achromatic. In DM-based pulse shapers a phase shift ϕ at a wavelength λ requires a mirror deformation $\Delta z = \lambda\cdot\phi/4\pi$. Typical phase shifts are as high

as 5–10 optical cycles, whereas the resolution is in the range of fractions of a cycle. Therefore, according to the spectral range of operation, the DM has to be designed to meet the minimum and maximum deformation at the given carrier wavelength. These pulse shapers give the advantage of adapting the spectral phase to the specific application. In combination with fast pulse measurement techniques and closed feedback loop, they allow the active compensation of the dispersion of an optical system [97]. Pulse shapers based on the 4-*f* arrangement have been applied to the compression of pulses from the visible to the IR spectral range [98].

5. An acousto-optic programmable dispersive filter (AOPDF) [99, 100] is another device based on acousto-optics technology, but with a different approach with respect to the 4-*f* pulse shapers. As sketched in Fig. 6d, in an AOPDF, the modulator is not positioned in the Fourier plane of a dispersive delay line, but the acoustic wave and the light beam propagate collinearly, with the advantage of maximizing the interaction length. At phase matching between the acoustic wave and the ordinary and extraordinary modes of a light frequency, part of the ordinary mode is diffracted into the extraordinary plane, and propagates at a different velocity. The acoustic frequency is a function of time and can be carved so that any frequency component ω is diffracted at a given propagation length z; in this way it is possible to almost arbitrarily shape the pulse emerging at the extraordinary plane. The AOPDF technique can be applied to the NIR [100], visible [101], and UV [102] regions. Recently, amplitude and phase shaping was extended to 20 μm by employing calomel (mercurous chloride) as acousto-optic substrate [103]. Unfortunately, due to their principle of operation, AOPDFs are (at least at present) commercially available only for pulse repetition rates up to approximately 30 kHz.

3.2. Control of relative delay

In the parallel synthesis scheme the beams are derived from a common (seed) source, which is suitably split into two or more channels. The beams then follow different paths where they can undergo amplification, compression, or other spectral manipulations, and finally are recombined. The distance between the splitting and the recombination points can be several meters. To achieve a good pulse synthesis it is therefore necessary to compensate for environmental drifts and fluctuations that can cause timing jitter. The drifts can be due to temperature, humidity, and mechanical instabilities depending on the experimental conditions. It is important to minimize the drifts by stabilizing the environmental conditions, enclosing the setup to avoid air fluctuations, and using stable optomechanics. Once these precautions aimed at optimizing the passive stability have been taken, it is possible to actively compensate for the residual timing jitter within certain limits through optical techniques.

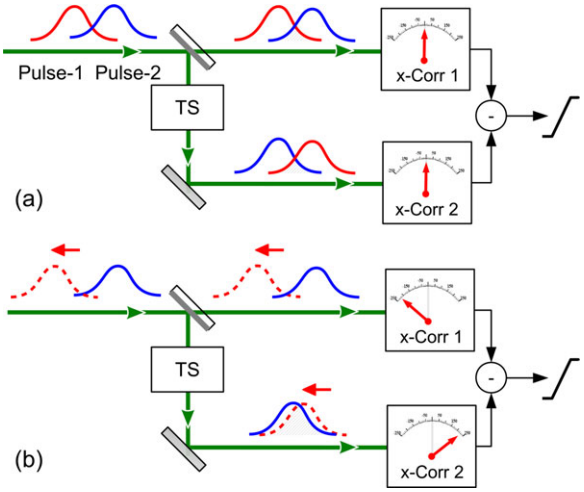

Figure 7 General scheme of BOC for the measurement of the variation of the relative delay between two pulses. X-Corr: cross-correlator for the measurement of temporal overlap; TS: time-swap module, reversing the order between the pulses. (a) BOC is balanced, producing a negligible differential signal. (b) A change in the relative delay, indicated as an arrow on the dashed pulse, changes the overlap between the pulses, unbalancing the output of the BOC.

Balanced optical cross-correlation (BOC) is the most established and robust technique for timing jitter compensation. The BOC scheme was initially implemented in laser technology for the challenging synchronization necessary to generate broadband light pulses from different oscillators [62]; in this case, the signal from the BOC was used to lock the repetition rates of the two lasers and hence the delay between the two pulse trains. The same BOC scheme was then successfully applied for the control of timing drifts of two pulses derived from the same source and therefore sharing the same repetition rate. The technique is based on the balanced detection of an optical cross-correlation between the two pulses to be synthesized, which is highly sensitive to their delay; when it is close to zero, the correlator produces a signal linearly proportional to the relative time delay, which can then be used for feedback compensation of the pulse delay. The beauty of the BOC scheme is that amplitude fluctuations of the pulses are effectively canceled out in the balanced detection scheme (high common mode rejection), such that the measurement of phase changes is not affected by amplitude fluctuations.

In the general BOC scheme, sketched in Fig. 7, the two pulses to be synchronized, namely pulse 1 and pulse 2, are delayed before being collinearly combined. A beam splitter then prepares two replicas of the combined beam: in the path of one of the replicas a time-swap module (TS) is inserted to swap the two pulses in time, so that in one path pulse 1 arrives before pulse 2, and in the other path pulse 2 arrives before pulse 1. In each arm, the delayed replicas are nonlinearly mixed, for example through sum-frequency generation, producing a cross-correlation signal proportional to their temporal overlap (shaded areas of Fig. 7). The pulse

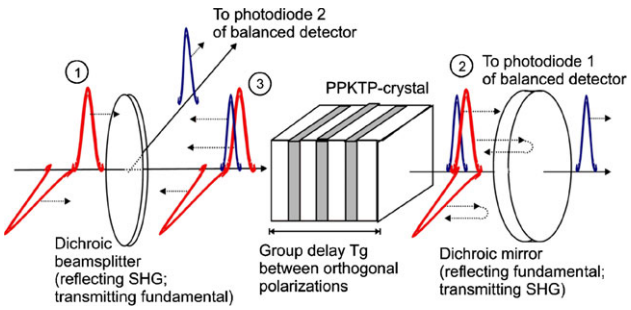

Figure 8 Scheme of a single-crystal BOC. Image from [105].

intensities and initial delays can be adjusted to balance the cross-correlation signals from the two arms (Fig. 7a). If the delay between the pulses changes before the synthesis (Fig. 7b, dashed pulse), the overlap between them is different for the two arms, and the cross-correlation signals become unbalanced. Within certain limits in the vicinity of zero delay, the BOC output signal is linearly proportional to the time delay between the two pulses, which can be used to compensate for it in a feedback loop. The scheme can successfully be applied for the synchronization of pulses both at the same wavelength and in different spectral regions. In the following we provide examples of these cases, with the experimental arrangements required to obtain the cross-correlation signal and the time-swap between the pulses.

In [105, 106] the authors showed a compact setup employing a single-crystal balanced cross-correlator, used for large-scale timing distribution systems, sketched in Fig. 8. In this case, the two pulses to be synchronized are in the same wavelength region; here the delay necessary for time-swap is introduced via birefringence experienced by the two cross-polarized pulses. The input cross-polarized pulses undergo second-harmonic generation (SHG) in a thick type-II phase-matched periodically poled potassium titanyl phosphate (PPKTP) crystal. A dichroic mirror reflects back the fundamental beams and transmits the second-harmonic light, detected by one photodiode of a balanced detector. The reflected fundamental light travels back in the PPKTP crystal and is again frequency doubled. This second harmonic (SH) light is now reflected by a second dichroic harmonic separator and detected by the second photodiode of the balanced detector. This double pass in the PPKTP crystal has the twofold role of delaying the two cross-polarized fundamental beams and of generating the cross-correlation signal by SHG. With this compact scheme, the authors demonstrated recently < 2.5 fs precision stabilization of an approximately 3.5 km long fiber link over a continuous unaided operation of 40 hours [107].

In [62] the BOC method was used to synchronize two independent Ti:sapphire and Cr:forsterite mode-locked lasers, emitting in different spectral regions; the scheme is the optical equivalent of a balanced microwave phase detector [108]. The two beams are combined by a metallic

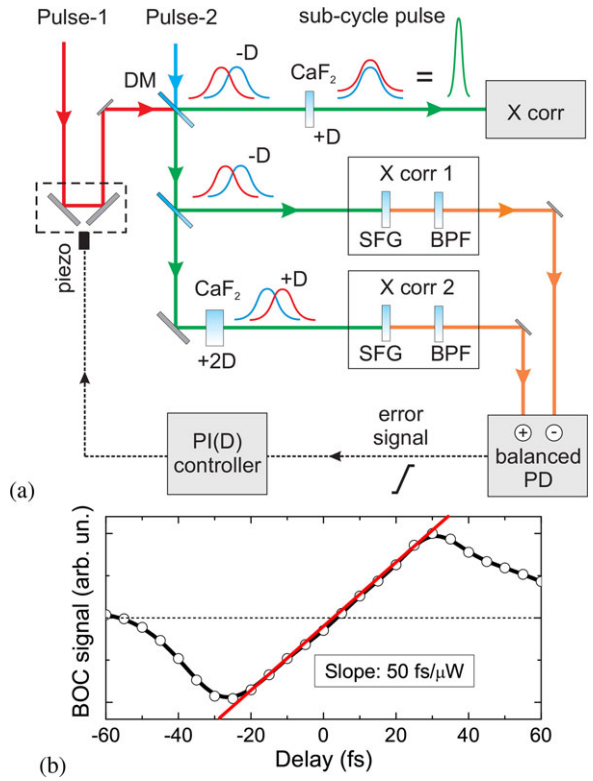

Figure 9 (a) The setup of BOC used for the synthesis from pulses in different spectral regions. DM: dichroic mirror used for recombination; SFG: sum-frequency generation crystal; BPF: band pass filter; PD: photodiode; D: spectral dispersion. (b) BOC output signal versus delay between the pulses. Scheme and data from [66].

beam splitter. One part of the combined beam is directed to two nearly identical cross-correlators, equipped with 1 mm thick lithium triborate crystals phase matched for sum-frequency generation (SFG) between 833 nm light from the Ti:sapphire laser and 1225 nm light from the Cr:forsterite laser. The exchange in time order between the pulses in one of the two arms is obtained by propagation in a 3 mm thick fused silica window. The authors demonstrated a timing jitter as low as 300 attoseconds over the frequency range from 10 mHz to 2.3 MHz. In Section 5.5 we review some of the setups that are typically used for sub-cycle synthesis of femtosecond OPAs/OPCPAs working in different spectral regions [65, 66]. All these schemes implemented the double-crystal setup [62]; in practice, although less compact than the single-crystal scheme, this approach is easier to use and align. The beams from the two parametric amplifiers are spatially combined on an imperfect dichroic mirror reflecting the short wavelengths and transmitting the long wavelengths (we will call them blue and red for brevity). The leakage of the combiner produces a beam made of the reflected red and the transmitted blue components, which feeds the BOC setup. In Fig. 9a we sketch a scheme of BOC; here the blue and red pulses correspond to two different frequency components of each pulse. When the pulses belong to different spectral regions, the time swap required in one

arm of the correlator can be simply introduced by linear dispersion.

To this end, the chirp of the two pulses is initially negative (−D), so that propagation in a plate of CaF_2 with thickness d (introducing dispersion +D) is sufficient to compress and synchronize the pulses at the experimental point, indicated as X-corr. The time swap required in one arm of the BOC can be obtained by a glass plate adding dispersion +2D, i.e. a plate of CaF_2 with thickness $2d$.

The cross-correlation between the two pulses is the sum-frequency (SF) light obtained in a nonlinear crystal, which is then narrowband filtered and measured by the two photodiodes of the balanced detector. The cross-correlation signals are adjusted in order to be perfectly balanced when the pulses are synchronized. When the delay between the two pulses changes, in one arm the SF signal increases due to the increased temporal overlap between the blue and red components, while in the other arm it decreases; the cross-correlator is no longer balanced, and the detector produces a differential signal (error signal) which is, within certain limits, linearly proportional to the delay between the pulses (Fig. 9b). Furthermore, because of the balanced scheme, in the vicinity of the zero crossing the amplitude noises of the pulses cancel each other. The error signal, after electronic filtering and amplification, is sent to a PI(D) filter, which provides a feedback signal acting on a delay line equipped with a piezoelectric actuator, on the separate path of one of the two pulses before the synthesis. In [66] the SHG crystal is a 200-μm-thick β-barium borate (BBO) crystal, phase-matched for SFG of 870 nm light and 2.15 μm light. Use of the OPCPA delay stage and a 4 mm thick CaF_2 window in the BOC sets the group delay between pulses to +25 fs in one cross-correlator arm and −25 fs in the other. An additional 2-mm-thick CaF_2 window in the synthesized beam path ensures zero group delay at the combined output. With this choice of optical elements, the response of the BOC as a function of delay is shown in Fig. 9b; as expected, the differential signal is maximum at ±25 fs, and is linear for delays up to ±20 fs. The resolution of the BOC is evaluated as the product between the slope of the linear region and the noise equivalent power (NEP) of the detector. In the case of [66], the resolution was 50 fs/μW (slope) × 2.5 nW (NEP) = 12.5 as. The initial delay between the pulses, the thickness of the nonlinear crystal, and the dispersion introduced in one or both of the two branches (which can be achieved with bulk materials, chirped mirrors, or other methods) determine the slope of the linear region. A steep linear region means high time resolution, but also a narrower time window in which the signal is linear with the delay, which makes it easier to drop out of the linear region. Should this happen, the feedback system would detect a wrong delay, which would lead to loss of the locking; for this reason, measuring the open-loop jitter is very important for choosing the correct dispersion. In the case where the timing jitter is too high, such that the resolution would not be sufficient, it is possible to use two consecutive feedback loops, one for the coarse jitter and one for the fine jitter compensation. The delays in the two branches should be approximately opposite to each other (e.g. ±20 fs). The crystal thickness, the frequencies which produce the SF (in the case where the spectrum is broad), and their intensities need to be chosen in such a way that the SF signals are as high as possible; in addition, the thickness of the nonlinear crystals introduces linear dispersion, which needs to be taken into account in the delay calculation. Finally, the optical filters for the SF signal, and the polarizers should be chosen to have a good suppression of the fundamental frequencies, a good transmission of the SF signals, and a bandwidth that does not limit the time resolution.

3.3. Control of the carrier–envelope phase: active and passive phase locking

The control of the CEP plays a key role in the generation of optical transients with a reproducible electric field $E(t)$. In the case of waveform synthesis, control of the CEP is twofold: on the one hand, as explained in Section 3, the control of the AP of the interacting pulses required to preserve their constructive interference asks for the locking of their CEP and of their relative delay. On the other hand, even in the case of a perfect relative timing lock, it is the CEP of the synthesized pulse which has to be carefully controlled. For these reasons it is necessary to monitor the CEP of at least one of the parent pulses and their relative phases. To this end, we describe here the main techniques allowing the stabilization and control of the CEP; in Section 4.2 we also focus on the absolute phase characterization.

The CEP of a light pulse can be manipulated both by linear and nonlinear processes. In linear processes, such as propagation in a dispersive medium, the difference between the group and phase velocities leads to a slip of the carrier with respect to the envelope. By means of wedged glass plates of variable thickness, it is possible to exploit this effect to set the CEP and to compensate for drifts. If nonlinear optical processes occur, they lead to the mixing of the optical frequencies and of the spectral phases. In the following, we briefly explain how nonlinear processes allow manipulating the CEP and measuring its fluctuations. We first consider the case of nonlinear three-wave mixing, in which three waves of frequencies ω_1, ω_2, and ω_3, with $\omega_3 = \omega_1 + \omega_2$, are coupled in a second-order nonlinear crystal. Similarly to the frequency conservation, the CEPs of the three waves are also linked by the relationship $\varphi_3 = \varphi_1 + \varphi_2 + \text{const}$. To show this, let us study the interaction of three linearly polarized quasi-monochromatic plane waves which collinearly propagate in the z-direction:

$$E_i = A_i \exp[j(\omega_i t - k_i z)] + \text{c.c.}, \tag{8}$$

where A_i are the complex amplitudes, k_i are the wave vectors, and ω_i denote the angular frequencies ($i = 1, 2, 3$).

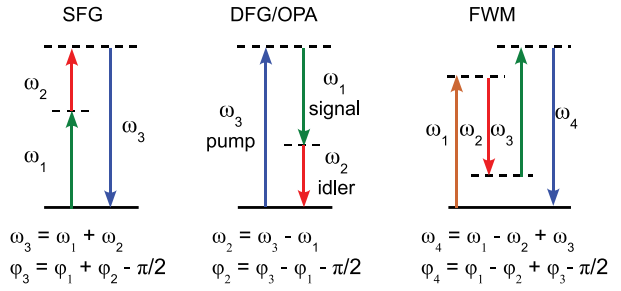

Figure 10 Frequency and phase summation rules for (a) sum-frequency generation (SFG), (b) difference-frequency generation (DFG), equivalent to the generation of the idler wave in an OPA, and (c) four-wave mixing (FWM) process.

We follow the usual treatment by a system of three coupled equations in the absence of absorption [109]:

$$\begin{cases} \dfrac{\partial A_1}{\partial z} = -j\sigma_1 A_3 A_2^* \, \mathrm{e}^{j\Delta k z} \\ \dfrac{\partial A_2}{\partial z} = -j\sigma_2 A_3 A_1^* \, \mathrm{e}^{j\Delta k z} \\ \dfrac{\partial A_3}{\partial z} = -j\sigma_3 A_1 A_2 \, \mathrm{e}^{-j\Delta k z} \end{cases}, \tag{9}$$

where σ_i are the nonlinear coupling coefficients and $\Delta k = k_3 - k_2 - k_1$ is the phase mismatch. Introducing $A_i = B_i \exp(j\varphi_i)$, where $B_i = |A_i|$ are the amplitudes and φ_i are the phases of the respective waves, the real and imaginary parts of Eq. (9) are transformed to

$$\begin{cases} \dfrac{\partial B_1}{\partial z} = \sigma_1 B_2 B_3 \sin\Psi \\ \dfrac{\partial B_2}{\partial z} = \sigma_2 B_1 B_3 \sin\Psi \\ \dfrac{\partial B_3}{\partial z} = -\sigma_3 B_1 B_2 \sin\Psi \\ \dfrac{\partial \Psi}{\partial z} = \Delta k + \left(\sigma_1 \dfrac{B_2 B_3}{B_1} + \sigma_2 \dfrac{B_1 B_3}{B_2} - \sigma_3 \dfrac{B_1 B_2}{B_3}\right) \cos\Psi, \end{cases} \tag{10}$$

where $\Psi = \varphi_3 - \varphi_2 - \varphi_1 + \Delta k z$ is the so-called generalized phase. Assuming perfect phase matching, $\Delta k z = 0$, system (10) leads to simple solutions for different boundary conditions. Let us first consider the case of SFG, i.e. the generation of a field at $\omega_3 = \omega_1 + \omega_2$. Assuming the boundary condition $B_3(z = 0) = 0$, the value of the generalized phase that maximizes the right-hand side in the third equation in (10) is $\Psi = -\pi/2$, which corresponds to the SFG phase $\varphi_{\mathrm{SFG}} = \varphi_3 = \varphi_1 + \varphi_2 - \pi/2$ (see Fig. 10a). For the case of SHG of a field at the fundamental frequency (FF), which is a degenerate SFG process with $\omega_1 = \omega_2 = \omega_{\mathrm{FF}}$ and $\omega_3 = \omega_{\mathrm{SH}} = 2\omega_{\mathrm{FF}}$, we get $\varphi_{\mathrm{SH}} = 2\varphi_{\mathrm{FF}} - \pi/2$. Let us now consider the case of difference-frequency generation (DFG), which is equivalent to the process of idler generation in an OPA, i.e. $\omega_2 = \omega_3 - \omega_1$: assuming the boundary condition $B_2(z = 0) = 0$, the value of the generalized phase that maximizes the right-hand side term in the second equation in (10) becomes $\Psi = \pi/2$. Consequently, $\varphi_{\mathrm{DFG}} = \varphi_2 = \varphi_3 - \varphi_1 - \pi/2$ (Fig. 10b). A very similar effect occurs in the third-order nonlinear process of four-wave mixing (FWM), in which four waves at frequencies ω_1, ω_2, ω_3, and ω_4, with $\omega_4 = \omega_1 - \omega_2 + \omega_3$, are coupled in a third-order nonlinear medium. The CEPs of the waves are linked by the relationship $\varphi_4 = \varphi_1 - \varphi_2 + \varphi_3 - \pi/2$ (Fig. 10c). Self-phase modulation (SPM), i.e. spectral broadening due to the instantaneous intensity-dependent variations of the index of refraction in a Kerr medium, can be regarded as a special case of FWM [110], in which a new frequency ω_{SPM} is generated starting from three frequencies ω_1, ω_2, and ω_3, all belonging to the pulse spectrum, by the FWM process $\omega_{\mathrm{SPM}} = \omega_1 - \omega_2 + \omega_3$. These new frequencies in turn contribute to subsequent FWM processes, causing a progressive broadening of the pulse spectrum as it propagates through the nonlinear medium. If we now consider that the mixing frequencies belong to the same pulse and hence share the same CEP $\varphi_1 = \varphi_2 = \varphi_3 = \varphi$, then the SPM pulse will have the CEP $\varphi_{\mathrm{SPM}} = \varphi_1 - \varphi_2 + \varphi_3 - \pi/2 = \varphi - \pi/2$. This demonstrates that, net $\pi/2$, the newly added frequency components of the broadened SPM spectrum inherit the original value of the CEP of the driving pulse. The SPM/FWM process is the dominant nonlinear interaction behind the spectral broadening in gas-filled hollow waveguides [6] and in gas filaments [11] and white-light continuum (WLC) generation in bulk materials [111]. CEP preservation in SPM/FWM can be exploited at various levels for waveform synthesis: (i) spectral broadening is one of the key mechanisms for the generation of ultrabroadband pulses; if different light fields are independently derived from spectral broadening of the same laser source, CEP preservation automatically ensures their relative phase locking, as required by the pulse synthesis scheme; (ii) when SPM is driven by a CEP-stable source, then the broadened light will inherit its constant CEP; the synthesis of CEP-stable light pulses therefore calls for the development of phase-stable laser sources; and (iii) since all components of the broadened light are phase-locked, CEP preservation can be exploited to generate passively phase-stable pulses by the scheme of difference-frequency mixing. In the following we review the basic principles and the most recent achievements of the active and the passive phase stabilization techniques for the generation of phase-stable pulse trains.

3.3.1. Active carrier–envelope phase locking

To understand active CEP stabilization, one must recall that a mode-locked laser can be schematically described in the time domain as a pulse propagating back and forth between the cavity mirrors and being partially transmitted every time it impinges on the output coupler. Accounting only for the gain crystal, in each round trip the CEP of the pulse changes by

$$\Delta\varphi = L_{\mathrm{eff}} \left(\frac{1}{v_{\mathrm{g}}} - \frac{1}{v_{\mathrm{p}}}\right) \omega_0, \tag{11}$$

where v_g and v_p are the group and phase velocities of the pulse, respectively, L_{eff} is double the thickness of the gain medium, and ω_0 is the carrier frequency; here $\Delta\varphi$ is understood modulo 2π. Therefore a free-running laser oscillator generates pulses with CEP that varies from shot to shot. The time interval between the emission of two pulses with the same CEP is called the carrier–envelope offset (CEO) time and is defined as

$$T_{CEO} = \frac{2\pi}{\Delta\varphi} T_r, \tag{12}$$

where T_r is the round-trip time. The resulting pulse train emitted by the laser can then be written as

$$\begin{aligned} E(t) &= \sum_n E_p(t - nT_r) \\ &= \sum_n A_p(t - nT_r) \exp\{j[\omega_0(t - nT_r) + \varphi_0 + n\Delta\varphi]\} \\ &\quad + c.c. \end{aligned} \tag{13}$$

where $A_p(t)$ is the pulse envelope and φ_0 the initial phase. In the frequency domain, the Fourier transform of the pulse train then becomes

$$\tilde{E}(\omega) = \sum_n \tilde{A}_p(\omega - \omega_0) \exp\{-j[n\omega T_r - \varphi_0 - n\Delta\varphi]\}, \tag{14}$$

which can be rewritten, using the rotating-vectors approach, as

$$\tilde{E}(\omega) = \tilde{A}_p(\omega - \omega_0) \exp(j\varphi_0) \sum_m \delta\left(\omega - m\frac{2\pi}{T_r} - \frac{\Delta\varphi}{T_r}\right) \tag{15}$$

showing that the spectrum of the mode-locked pulse train is a comb of discrete longitudinal modes at frequencies

$$\omega_m = \frac{2m\pi}{T_r} + \frac{\Delta\varphi}{T_r} \tag{16}$$

or equivalently

$$\nu_m = m\nu_r + \nu_{CEO}, \tag{17}$$

where $\nu_r = 1/T_r$ is the repetition frequency and $\nu_{CEO} = 1/T_{CEO} = (\Delta\varphi/2\pi)\nu_r$ is the CEO frequency, i.e. the extrapolated comb frequency closest to zero, which has a value ranging between zero and the laser repetition frequency ν_r. Both $\Delta\varphi$ and ν_{CEO} are generally not constant in time, but change due to fluctuations in the laser oscillator parameters.

The active approach to the generation of pulses with stable CEP consists of four steps, according to the scheme shown in Fig. 11:

1. Measure the CEO frequency ν_{CEO} using a nonlinear interferometer (see Section 4.2).
2. Stabilize ν_{CEO} by an active high-bandwidth feedback on the laser oscillator (fast loop), typically varying the laser pump power with an acousto-optic modulator. In this way one generates a train of pulses with constant $\Delta\varphi$, i.e. with reproducible shot-to-shot CEP evolution at a repetition rate of ν^*_{CEO} at an integer fraction of the oscillator frequency ν_r.
3. Pick pulses at the integer fraction of ν^*_{CEO} to generate a train of actively CEP-stabilized pulses. This naturally occurs in the pulse amplification process, which usually proceeds at a lower frequency with respect to that of the oscillator.
4. After amplification, measure the CEP φ of the pulses using a single-shot nonlinear interferometer and use an additional feedback loop (slow loop) to correct for fluctuations induced by the amplification process (and optionally external spectral broadening, e.g. in a hollow-core fiber compressor) and lock the CEP to φ^*. The slow feedback loop acts on the amplification stage, as exemplified in Fig. 11. Among the processes that may induce CEP fluctuations in the amplification chain, we mention the change of grating separation; for this reason, the slow feedback loop typically acts on the stretcher before the amplification [112]. In other schemes, the loop modulates the pump of the oscillator.

Using active stabilization methods, it is routinely possible to generate amplified pulses with root-mean-square (rms) CEP fluctuations of the order of 100–200 mrad over several hours of measurement time [113]. A completely different approach for active CEP stabilization of a laser oscillator is the feed-forward method [114], in which ν_{CEO} of the output of a free-running oscillator is first measured using a nonlinear interferometer and then used to drive an acousto-optic frequency shifter (AOFS) which imparts a shift equal to $-\nu_{CEO}$ in its first diffraction order. Advantages of the feed-forward method are the robustness, due to the absence of a feedback loop, the very large bandwidth (in excess of 300 kHz), and the capability to generate CEP-stable pulses, i.e. pulses with $\nu_{CEO} = 0$, directly from the oscillator. In Ref. [115] the system was further optimized, reducing the angular dispersion introduced in the AOFS process and the large frequency chirp caused by the AOFS. The feed-forward stabilization scheme is prone to slow CEP drifts due to, for example, changes of the relative humidity, which can be taken out using an additional slow feedback loop. Nonetheless, the rms phase error rarely exceeds 150 mrad within any given one-hour period.

3.3.2. Passive stabilization of carrier–envelope phase

The passive method is an alternative all-optical approach for the generation of CEP-stable pulses [116]. If a DFG process $\omega_{DF} = \omega_2 - \omega_1$ occurs between two pulses with the same shot-to-shot CEP fluctuations φ, so that $\varphi_1 = \varphi$ and $\varphi_2 = \varphi + c$, then $\varphi_{DF} = \varphi_2 - \varphi_1 - \pi/2 = c - \pi/2 =$

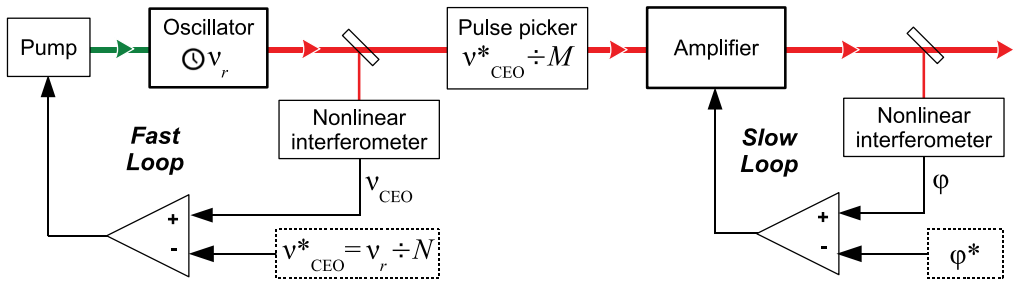

Figure 11 Scheme for active CEP stabilization; ν^*_{CEO} and φ^* are the target values of ν_{CEO} and φ, respectively.

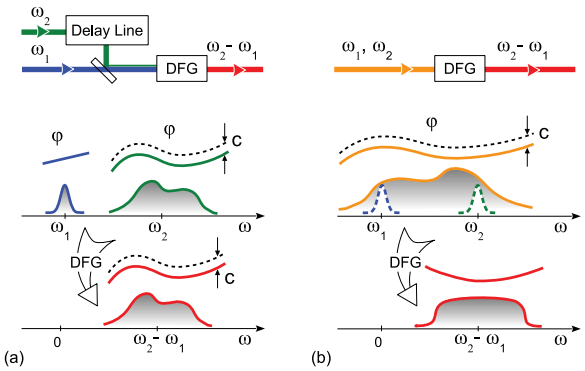

Figure 12 Comparison of (a) inter-pulse and (b) intra-pulse stabilization schemes. Lower panels show the evolution of both intensity and phase in the frequency domain; φ is the absolute phase, c denotes fluctuations of the CEP.

const., i.e. the fluctuations of φ are automatically canceled [117]. Passive CEP stabilization has some clear advantages with respect to active stabilization: (i) being an all-optical technique, it does not require any electronic feedback circuits imposing bandwidth limitations and (ii) it directly produces a train of CEP-stable pulses, avoiding the need to pick pulses at a fraction of ν_{CEO}.

There are two possible experimental implementations of this method. *Inter-pulse* DFG processes involve mixing of two separate CEP-locked frequency-shifted pulses synchronized by a delay line, as schematically represented in Fig. 12a. Inter-pulse DFG may also occur in OPAs, since DFG is equivalent to the process of idler generation in an OPA; when the signal and the pump of the OPA are derived from the same source, the idler is phase-stable. *Intra-pulse* schemes involve mixing between different frequency components of a single ultrabroadband pulse, as depicted in Fig. 12b [118, 119]; in this case, the frequencies are intrinsically CEP-locked. A similar effect is encountered in terahertz pulse generation by optical pulse rectification [120, 121], which may be viewed as a special case of a three-wave mixing process. In the case of inter-pulse DFG, the resulting spectral phase is influenced by the phase of the interacting input pulses and by any relative fluctuation c of the CEP; in the example shown in Fig. 12a, where the high-frequency pulse is broadband and the low-frequency one is narrowband, the DFG bandwidth is mainly due to the high-frequency pulse, and its spectral phase is transferred [122] to the DFG pulse. In the case of the intra-pulse scheme of Fig. 12b, the DFG spectrum and phase depend on the dispersion properties of the nonlinear crystal; since all interacting frequencies are phase locked, the absolute phase of the DFG pulse is not affected by fluctuations c.

4. Ultrabroadband pulse characterization techniques

In the previous sections we reviewed the techniques for the manipulation of the spectral phase and the CEP fluctuations of a pulse, and for the measurement of the delay jitter of the sub-pulses before their coherent combination. In this section, we now describe the main schemes for the full characterization of a synthesized pulse. In Section 4.1 we first review the techniques developed for the challenging spectrotemporal characterization of ultrabroadband pulses and that can be applied either to the sub-pulses or directly to the synthesized waveform. In Section 4.2 we discuss the techniques for the measurement of the CEP jitter and, in the case of spectral overlap between the sub-pulses, of the relative fluctuations of the AP.

4.1. Spectrotemporal characterization

Once extremely short and ultrabroadband waveforms are generated, one faces the next paramount challenge: how to perform a complete spectrotemporal characterization of such waveforms in both amplitude and phase. Fortunately, in recent years, several pulse characterization techniques have been developed for the full characterization of ultrashort pulses. An in-depth analysis and discussion of these techniques with all their intricacies is beyond the scope of this review on waveform synthesis; for this reason we will refer readers to several excellent treatments elaborating on these techniques. Instead, in this section we focus our attention on discussing the specific challenges and requirements emerging in the characterization of (multi-)octave single- or even sub-cycle waveforms.

4.1.1. Frequency-resolved optical gating

Since its first demonstration [123], frequency-resolved optical gating (FROG) has emerged as a powerful, reliable, and versatile technique for the complete spectrotemporal

Table 2 Various FROG characterization techniques.

Order	Nonlinearity	Signal field
2	SHG	$E_{\mathrm{sig}}^{\mathrm{SHG}}(t,\tau) = E(t)E(t-\tau)$
3	(surface) Third-harmonic generation	$E_{\mathrm{sig}}^{\mathrm{THG}}(t,\tau) = E^2(t)E(t-\tau)$
3	Self-diffraction	$E_{\mathrm{sig}}^{\mathrm{SD}}(t,\tau) = E^2(t)E^*(t-\tau)$
3	Transient grating	$E_{\mathrm{sig}}^{\mathrm{TG}}(t,\tau) = E^2(t)E^*(t-\tau)$
3	Polarization gating	$E_{\mathrm{sig}}^{\mathrm{PG}}(t,\tau) = E(t)\lvert E(t-\tau)\rvert^2$

characterization of ultrashort optical pulses in amplitude and phase [124, 125]. FROG measurements permit a time–frequency analysis of the electromagnetic pulse – in analogy to musical scores describing the frequency and intensity of each note versus time. A whole zoo of FROG versions have been developed [125], which differ, for example, in the optical nonlinearity used (see Table 2), geometry (standard non-collinear FROG versus collinear interferometric (i.e. fringe-resolved) FROG), inherently multi-shot apparatus with scanning delay lines versus single-shot FROG devices with no moving components [124, 125], etc. The choice of which FROG scheme to use in an experiment critically depends on the experimental situation, e.g. on the spectral range, bandwidth and energy of the pulses, the availability of suitable nonlinear crystals/glasses or optical spectrometer, the source pulse repetition rate, the question as to whether one intends to perform single-shot characterization of amplified pulses, or if fluctuations in the pulse parameters of the pulse train are present.

In general, a FROG measurement provides a spectrogram (FROG trace) $I_{\mathrm{FROG}}(\omega,\tau)$ that can be expressed as

$$I_{\mathrm{FROG}}(\omega,\tau) = \left| \int E(t)g(t-\tau)\exp(-j\omega t)\,\mathrm{d}t \right|^2 = \left| \int E_{\mathrm{sig}}(t,\tau)\exp(-j\omega t)\,\mathrm{d}t \right|^2 . \quad (18)$$

In this expression, $g(t-\tau)$ represents the gate function, which selects a portion of the field $E(t)$ around the delay τ. The signal fields $E_{\mathrm{sig}}(t,\tau)$ for the different FROG nonlinearities are summarized in Table 2. For the sake of simplicity, an instantaneous nonlinear response is assumed in our discussion. To be more specific in the following, we look at the most common SHG-FROG technique more closely with the aim of characterizing extremely short and ultrabroadband optical pulses. SHG-FROG is basically a spectrally resolved second-order field autocorrelation. The iterative FROG pulse-retrieval algorithm (for details of the algorithm, see [123–125]) can reconstruct, from the measured FROG trace and the known type of the optical nonlinearity, the pulse in both amplitude and phase (see, for example, retrieved spectral intensity and phase as well as the retrieved temporal intensity and phase profiles shown in Fig. 24 in Section 5.2). Note also that some FROG types have known ambiguities (e.g. for SHG-FROG, the direction of time and relative phase of multiple pulses). For the characterization of ultrabroadband waveforms, the following challenges need to be tackled. (1) The components of the optical setup must be carefully chosen to support the whole bandwidth and without introducing excessive dispersion (e.g. the beam splitters). (2) The type-I SHG crystal needs to be thin enough to provide sufficient phase-matching bandwidth to convert the whole fundamental spectrum into the spectral region of the second harmonic. (3) The non-collinearity angle needs to be small enough to keep geometric time-smearing effects (so-called "pancake effect") to a minimum. This is particularly challenging for larger beam diameters of high-energy pulses. (4) Ideally the spectral response of the spectrometer (due to the diffraction grating and CCD detector) should be flat over the full range of the SHG spectrum. Note that any spectrally non-flat response in the SHG process and of the spectrometer can be corrected by means of the marginal correction technique [125] as long as the measured FROG trace exhibits sufficient signal-to-noise ratio in that spectral region. Third-order FROG techniques, like surface third-harmonic generation FROG, are typically good choices for extremely broadband pulses, since they lack phase-matching constraints [126–128]. Ultrabroadband waveforms with bandwidth approaching or even exceeding two octaves can conveniently be characterized by third-order FROG techniques or by a *combination* of separate FROG measurements using different types of optical nonlinearities. Afterwards the challenge remains to retrieve also the missing synthesis parameters (delay time Δt, relative phase $\Delta\varphi$) as discussed in Section 5.2.

4.1.2. SPIDER and 2DSI

Interferometry is the most widely used technique to measure the difference of the optical phases between two waves. Thus, if one has a reference pulse with a well-known spectral phase, it is natural to characterize the spectral phase of the pulse under test by measuring the spectral interference between the pulse under test and the reference pulse. However, such a reference pulse is usually, if not always, unavailable. Spectral phase interferometry for direct electric field reconstruction (SPIDER) is a technique introduced in 1998 by Iaconis and Walmsley to solve the problem of unavailable reference pulse [129]. The idea is to generate, by means of nonlinear mixing processes, two spectra slightly shifted in frequency and to investigate the spectral interference of these two copies.

The technique is illustrated in Fig. 13: Fig. 13a shows the operation principle of SPIDER and Fig. 13b provides one of the numerous experimental implementations of the technique. The pulse under test is first split into two replicas by a beam splitter. Both replicas undergo nonlinear mixing such that the optical frequencies are shifted to ω from $\omega-\delta$ and $\omega-\delta-\Omega$, respectively. Ω is referred to as the *spectral shear* between the two replicas. The two replicas are then delayed by a delay line and combined into a spectrometer.

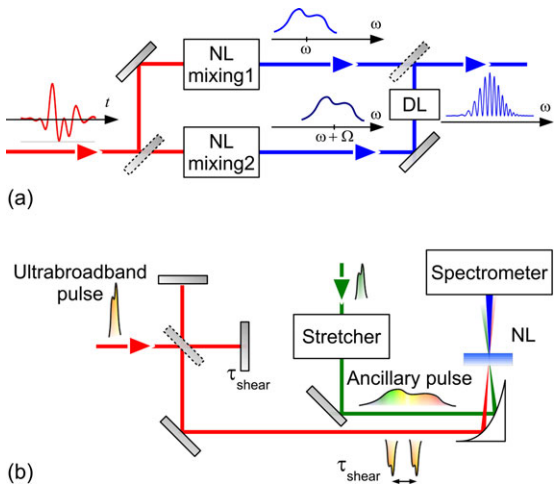

Figure 13 SPIDER pulse characterization. (a) Conceptual scheme of the technique. NL mixing: nonlinear mixing stages for the generation of frequency-shifted replicas of the input pulse; DL: delay line. (b) Layout of one experimental implementation of the conceptual scheme. NL: crystal for nonlinear mixing.

The spectrum can be expressed as

$$S(\omega) = \left| A_{\mathrm{R}}(\omega-\delta)\,\mathrm{e}^{j(\varphi(\omega-\delta)+\varphi_\delta)} + A_{\mathrm{S}}(\omega-\delta-\Omega)\,\mathrm{e}^{j(\omega\tau+\varphi(\omega-\delta-\Omega)+\varphi_{\delta+\Omega})}\right|^2 = S_{\mathrm{DC}}(\omega) + S^{+}(\omega)\,\mathrm{e}^{-j\omega\tau} + S^{-}(\omega)\,\mathrm{e}^{+j\omega\tau}. \quad (19)$$

When the delay τ is sufficiently large, $S^{+}(\omega)\,\mathrm{e}^{-j\omega\tau}$ can be isolated from the other two terms and its phase can be determined unambiguously:

$$\phi(\omega) = [\varphi(\omega-\delta) - \varphi(\omega-\delta-\Omega)] - \omega\tau + (\varphi_\delta - \varphi_{\delta+\Omega}) \approx \mathrm{GD}(\omega-\delta-\Omega/2)\cdot\Omega - \omega\tau + (\varphi_\delta - \varphi_{\delta+\Omega}), \quad (20)$$

where GD is the pulse group delay evaluated in $(\omega - \delta - \Omega/2)$, and the third term is a constant phase introduced during the nonlinear mixing. If the delay τ is determined with high precision, the linear phase $\omega\tau$ can be subtracted off and the remaining information of the wavelength-dependent group-delay is sufficient to determine, by integration, the spectral phase of the pulse. Figure 13b shows one way to generate the frequency-shifted replicas of the test pulse: a broadband ancillary pulse is stretched and synchronized to the pulse replicas so that the two replicas are overlapped with two frequency components of the ancilla, separated by Ω. A nonlinear mixing process, such as SFG or DFG, frequency shifts the test pulses. The resulting converted replicas are then coupled into a spectrometer for the detection of their interference pattern. The choice between SFG and DFG for the nonlinear mixing process depends on the frequency of the test pulse and on the constraints posed by phase matching, transparency range of the nonlinear crystal, and

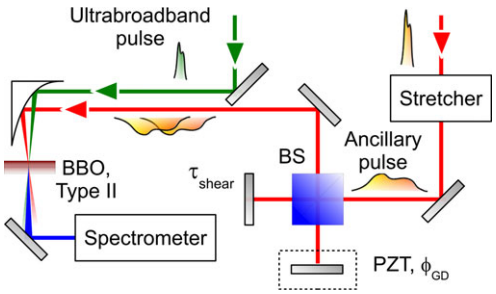

Figure 14 Scheme of 2DSI for characterizing the synthesized pulse. PZT: piezoelectric actuator.

the detector. SFG can be applied for the measurement of visible and IR test pulses; this process also offers the option to derive the ancilla from a replica of the pulse. For ultraviolet pulses, DFG can be used. Being a robust and direct method that avoids the need for iterative inversion algorithms, SPIDER has gained popularity since its inception and detailed design considerations are summarized in [130]. As is the case for many methods, however, challenges arise with standard SPIDER as bandwidths approach the single-cycle regime. The subtraction of $\omega\tau$ is the key to successful reconstruction of the spectral group delay. An error in determining the delay, $\delta\tau$, will result in a relative error in the measured pulse width, $\delta T/T \approx (\Delta\omega^2/2\Omega)\delta\tau$ [131]. The relative error scales quadratically with the bandwidth $\Delta\omega$ in an optical system. Such a catastrophic scaling makes the delay calibration increasingly hard for measurements of single-cycle or sub-cycle pulses. To eliminate such a hard calibration task, two novel delay-free self-referenced spectral interferometry techniques have been developed. Spatially encoded arrangement (SEA) SPIDER, developed first by Kosik *et al.* [132] and demonstrated recently for sub-4 fs pulses by Witting *et al.* [133], is a version of SPIDER that encodes the information of the wavelength-dependent group delay into the fringes in the spatial domain.

Another technique based on nonlinear mixing and spectral interferometry is two-dimensional spectral shearing interferometry (2DSI), developed by Birge *et al.* [134], which generates fringes in the time domain. Figure 14 shows a schematic representation of 2DSI. In its general implementation, the broadband pulse under test is guided via reflections only before being mixed in a type-II BBO crystal. The ancillary pulse, which may be a replica of the broadband pulse itself, is highly stretched before being split by a cube beam splitter, routed to the BBO crystal and mixed (by SFG or DFG) with the test pulse. Two collinear, temporally overlapped but spectrally sheared frequency-shifted pulses are then generated from the mixing of the pulse and the two chirped ancillae. The delay τ_{shear} between the chirped replicas fixes the spectral shear Ω. Since there are no temporal delay and spatial angle between the two spectrally shifted replicas, neither spectral nor spatial interference is present. To observe the interference between the two frequency-shifted pulses, which encodes the wavelength-dependent group delay information, the delay of one of the ancillary pulses is scanned over a few optical cycles. Due to the strong

chirp, the scanning of the delay over a few optical cycles can be approximated as a pure phase modulation ($\phi_{\rm gd}$). Detailed design considerations are summarized in [131]. The spectrum of the frequency-shifted signal is recorded as a function of this delay, yielding a two-dimensional intensity plot that is given by

$$\begin{aligned} I(\omega, \phi_{\rm gd}) &= |A(\omega-\delta) + A(\omega-\delta-\Omega)\,{\rm e}^{j\phi_{\rm gd}}|^2 \\ &= {\rm DC} + 2|A(\omega-\delta)A(\omega-\delta-\Omega)| \\ &\quad \times \cos[{\rm GD}(\omega-\delta-\Omega/2)\cdot\Omega + \phi_{\rm gd}]. \end{aligned} \quad (21)$$

An example of a 2DSI map is presented in Fig. 21 (Section 5.1). In this case, the ancilla is a replica of the test pulse, and the mixing process is SFG; the 2DSI setup is similar to the one illustrated in Fig. 37. The interpretation of the 2DSI data is relatively straightforward: each spectral component is vertically shifted by $\phi_{\rm gd}$, which is proportional to its group delay through the spectral shear Ω (see details in [131]). With the same criteria as in SPIDER, one can choose between SFG or DFG as mixing process. For ultraviolet pulses, DFG-based 2DSI has also been demonstrated [135]. It has been pointed out in [136, 137] that, for unstable pulse trains, multi-shot interferometric techniques like SPIDER and 2DSI only measure the nonrandom component ("coherent artifact"). Thus care must be taken to characterize shot-to-shot reproducible waveforms, and a comparison with other techniques (FROG, attosecond streaking) can furthermore exclude potential measurement errors.

4.1.3. Attosecond streaking and FROG-CRAB

If the synthesized waveforms have sufficient energy (above a couple of hundred microjoules) and are used for attoscience experiments involving HHG, then the waveforms plus the generated XUV pulses can directly and completely be characterized by attosecond ponderomotive streaking [138] using frequency-resolved optical gating for complete reconstruction of attosecond bursts (FROG-CRAB) [48, 139].

As shown in Fig. 28 in Section 5.3, we consider an attosecond streaking experiment, in which atoms of ionization potential $I_{\rm p}$ are exposed to an ionizing attosecond XUV pulse $\vec{E}_{\rm X}(t)$ in the presence of a time-delayed laser pulse $\vec{E}(t)$. Here, we assume that both XUV and laser pulses have parallel polarization. A time-of-flight (TOF) electron spectrometer measures the energy of photoelectrons ejected into the direction of the laser polarization dressed by the laser electric field versus time delay τ, yielding the streaking spectrogram ("FROG-CRAB trace"; see inset of Fig. 28) [140–142], which (within the single-active electron approximation) can be expressed as

$$\begin{aligned} &I_{\rm CRAB}(\vec{v}, \tau) \\ &\quad = \left| \int_{-\infty}^{\infty} {\rm d}t\, {\rm e}^{j\phi_{\rm G}(\vec{v},\tau)}\, \vec{E}_{\rm X}(t-\tau)\vec{d}\left[\vec{p}(t)\right]\, {\rm e}^{j(\vec{v}^2/2 + I_{\rm p})t} \right|^2 \end{aligned} \quad (22)$$

with $\vec{v}$ the final velocity of the photoelectrons, $\vec{A}(t)$ the vector potential of the laser field ($\vec{E}(t) = -\partial\vec{A}(t)/\partial t$), $\vec{p}(t) = \vec{v} + \vec{A}(t)$ the instantaneous momentum of the free electron in the laser field, and $\vec{d}$ the dipole transition matrix element from the ground state to the continuum state $|\vec{p}(t)\rangle$. In contrast to standard FROG described by Eq. (18), which uses an amplitude gate $g(t)$, in FROG-CRAB a pure phase gate $\phi_{\rm G}(\vec{v}, \tau) = -\int_t^{\infty} {\rm d}t' \left[\vec{v}\cdot\vec{A}(t') + \vec{A}^2(t')/2\right]$ is employed [140], which represents the quantum phase shift of the continuum electron interacting with the laser field. In order to use the generalized projections algorithm of FROG (see Eq. (18)) for pulse retrieval from the attosecond streaking spectrogram, no inseparable terms depending on both momentum $\vec{p}$ and time t are allowed [141]. For this reason, typically the central momentum approximation is made, which replaces $\vec{p}$ with the central momentum $\vec{p}_0$ of the photoelectrons. Neglecting the momentum dependence is valid as long as the bandwidth of the attosecond XUV pulse is much smaller than the center photon energy, but it fails for extremely short attosecond pulses with durations < 100 as [143]. For this extreme-duration limit, the phase retrieval algorithm by omega oscillation filtering (PROOF) was recently demonstrated [143].

Analysis of the streaking technique reveals that the shift of the photoelectron momentum directly reproduces the laser vector potential via $\Delta p(t) = -eA(t)$, which allows one to directly characterize the electric field waveform $E(t) = -\partial A(t)/\partial t$.

Note that a central assumption underlying FROG-CRAB (as for standard FROG) is that the input streaking spectrogram is composed of *single* wavepackets (created by single, unique pairs of XUV and laser fields), as opposed to an *ensemble* of them with different parameters of the XUV and laser fields changing from shot to shot. However, as a direct consequence of the small number of photoelectrons per laser shot, attosecond streaking is inherently a multi-shot pulse characterization technique (even if one could generate sufficient photoelectrons to perform a single-shot streaking measurement, such a measurement would suffer from enormous space-charge effects that would most probably result in the failure of the method). Thus *shot-to-shot reproducibility* of the waveforms is of utmost importance to obtain correct attosecond streaking results, because instabilities in the laser and XUV field parameters (photon energy, bandwidth, GDD, relative phases, timing of the different channels, etc.) can lead to substantial measurement errors, in particular an underestimation of the XUV pulse duration and of satellite XUV pulses [141, 142].

4.2. Characterization of carrier-phase fluctuations

In this section we review the different techniques used for the characterization of the AP and CEP of a pulse train and of $\nu_{\rm CEO}$ of a laser oscillator. All techniques rely on interferometry, and as inspection of the various implementations will reveal, it is not possible to have direct access to

the absolute value of the CEP or the AP, but only to their pulse-to-pulse fluctuations.

4.2.1. Linear phase measurement: Fourier transform spectral interferometry

The most straightforward technique for AP characterization is linear interferometry between two pulses. Typically this allows one to characterize the pulse under investigation by comparison with a reference pulse [144, 145], with a stable or known phase. The technique can also successfully be applied to compare the two parent pulses $E_1(t)$ and $E_2(t)$ of a synthesizer. Since this scheme reveals the relative phase difference between two pulse trains, it is successfully applied to characterize the AP shifts between the parent pulses of a synthesizer when their spectra partially overlap. When replicas of pulses $E_1(t)$ and $E_2(t)$ are recombined at a relative time delay τ and with a balanced intensity, they generate a spectral interference: any phase fluctuation will cause a shift in the fringe pattern of the interferogram. This spectrally resolved method has been named Fourier transform spectral interferometry (FTSI), and the generated interferogram can be expressed as

$$I(\omega) = |\tilde{E}_1(\omega)|^2 + |\tilde{E}_2(\omega)|^2 + 2|\tilde{E}_1(\omega)| \cdot |\tilde{E}_2(\omega)| \cos(\omega\tau + \Delta\varphi), \quad (23)$$

where τ is the time delay between the pulses and $\Delta\varphi = \varphi_2 - \varphi_1$ is the difference between the phases φ_1 and φ_2 of the pulses; $\Delta\varphi$ can be written as $\Delta\varphi = \Delta\varphi_{\mathrm{Amp}} + \Delta\varphi_{\mathrm{Noise}}$, which is the superposition of the phase fluctuations introduced, for example, by nonlinear processes in the generation and manipulation chains of each pulse ($\Delta\varphi_{\mathrm{Amp}}$) and the ambient phase noise caused by optical path-length variations ($\Delta\varphi_{\mathrm{Noise}}$). It should be stressed that FTSI does not provide information on the AP stability of the incoming pulses, but it allows a quantitative measurement of any possible relative phase noise introduced by any component in the paths of the pulses. This method can be employed with both temporal [146] and spectral interferometry [144], although the spectral variant is easier to align and does not require scanning like the temporal interference version. FTSI can be successfully applied to check the phase locking of the beams involved in the waveform synthesis process: provided that they have some spectral overlap, their interference pattern may directly detect some of the cases exemplified in Fig. 5. Since a relative change of the AP can be caused either by a CEP shift or by a group delay shift (see Fig. 5c and d), we will consider both possibilities. In Fig. 15 we show the interference patterns from the interaction of two pulses in adjacent spectral regions; we explore the effects due to changes of the CEP and the group delay of the low-frequency pulse. The time traces are provided in Fig. 15a and b, and the spectral interference is displayed in Fig. 15c and d. In Fig. 15, the dashed lines correspond to the field profiles providing the shortest synthesized pulse. In 15a, the *CEP* of the low-frequency pulse is shifted by

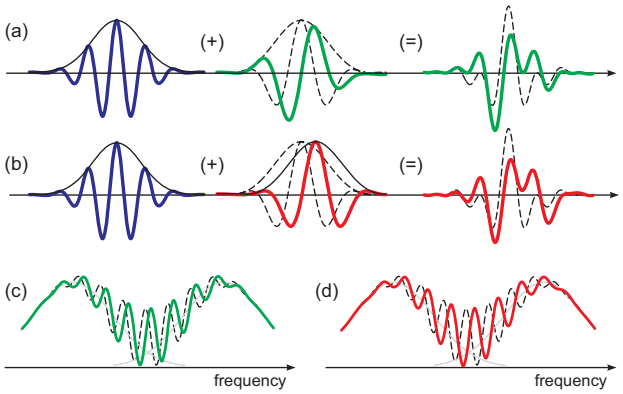

Figure 15 Sequence of interfering pulses and corresponding synthesized pulses and FTSI interferograms at the region of spectral overlap. For the low-frequency pulse, dashed lines are the reference profiles corresponding to the shortest synthesized pulse. Solid lines result from changes of (a) the CEP and (b) the group delay. (c) Thick solid line: inteferogram of configuration (a); (d) thick solid line: inteferogram of configuration (b); dashed lines: reference interferograms.

a quarter of the optical cycle (solid line). The corresponding spectral interferogram is illustrated as a solid line in Fig. 15c, and shows that a change of the CEP from the reference dashed line induces a clear shift from the dashed interference fringes. In Fig. 15b, instead, the *group delay* of the low-frequency pulse is increased by a quarter of the optical cycle, while the CEP is preserved, similarly to the case of Fig. 5d. The resulting interferogram is detailed in Fig. 15d; also in this case, the interference fringes shift from the reference pattern, showing that a group delay has the same effect as a phase shift. In general terms, this can be demonstrated by evaluating the group delay τ_{g} of a pulse as a function of its phase delay τ_{p}:

$$\tau_{\mathrm{g}} = \frac{\partial\varphi(\omega)}{\partial\omega} = \frac{\partial(\omega\tau_{\mathrm{p}})}{\partial\omega} = \tau_{\mathrm{p}} + \omega\frac{\partial\tau_{\mathrm{p}}}{\partial\omega}. \quad (24)$$

From this relation it is clear that in practice a change in group delay leads to a change in phase delay, with only small higher-order corrections. These examples demonstrate that FTSI is therefore sensitive to any AP shifts between the low- and high-frequency pulses, induced either by a CEP shift or by a change of the relative group delay, and responsible for dramatic changes of the synthesized waveform (Fig. 5). Whenever the two sub-pulse spectra have partial overlap, FTSI is a powerful tool for the measurement of fluctuations of their relative phase. By means of a suitable feedback loop, the measured phase shift can serve as the error signal for the active stabilization of the pulse relative delay. Examples of the application of the FTSI technique to the characterization of phase jitter are provided in Sections 5.3 and 5.5.

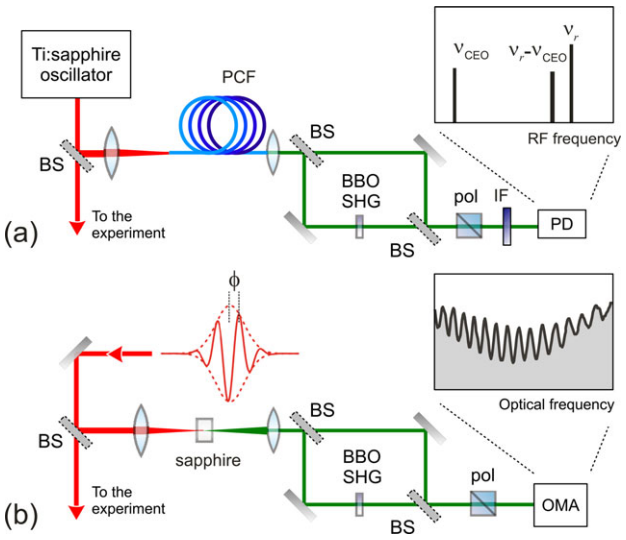

Figure 16 (a) *f*–2*f* interferometer for measuring ν_{CEO} of a laser oscillator. (b) Single-shot *f*–2*f* interferometer for measuring CEP fluctuations of an amplified laser pulse. BS: beam splitter; PD: photodiode; PCF: photonic crystal fiber; IF: narrowband interference filter; SHG: second-harmonic generation; pol: polarizer.

4.2.2. Self-referenced measurement of the carrier–envelope phase: *f*–2*f* interferometry

By *self-referenced* measurement we mean all those techniques which do not involve the comparison of a test pulse with a reference beam, but exploit the pulse to characterize itself. For this reason, self-referenced techniques allow the detection of CEP fluctuations, but are not able to assign them to AP shifts or group delay variations. Also these techniques are based on interferometry, but in this case the reference beam is derived from the test pulse itself by nonlinear processes. A typical nonlinear interferometer is the f–$2f$ interferometer, schematically illustrated in Fig. 16a.

The pulses under test are first spectrally broadened, until their bandwidth exceeds one octave. Sometimes this step is not necessary as the light already spans an octave of bandwidth, as in the case of broadband oscillators [147–150]. Subsequently, the red portion of the continuum is frequency doubled by a suitable SHG crystal, and spatially and spectrally overlapped with the blue portion of the continuum, projected along a common polarization by means of a polarizer. In the case of light from an oscillator, the FF, optionally broadened in a microstructured fiber, consists of a comb with frequencies $\nu_{FF} = \nu_{CEO} + m\nu_r$ while the SH consists of a comb with frequencies $\nu_{SH} = 2\nu_{CEO} + n\nu_r$. The FF and SH, projected along a common polarization, are sent to a fast photodetector; beating between FF and SH modes in the overlapping region produces notes at the radio frequencies ν_{CEO} and $\nu_r - \nu_{CEO}$, which can readily be detected by an RF spectrum analyzer. This scheme allows one to measure ν_{CEO}, as required in Section 3.3 (see Fig. 11). The f–$2f$ scheme requires a spectrum at the FF spanning an optical octave; when such a broad spectrum is not available, the overlap between other harmonics (such as $2f$–$3f$) can also be used. An alternative f–0 interferometer for the measurement of ν_{CEO} is based on the DFG and SPM processes [118]. In this approach, a frequency comb is generated by DFG between the high-frequency and the low-frequency portions of the broadband continuum. Considering two frequencies $\nu_1 = \nu_{CEO} + n\nu_r$ and $\nu_2 = \nu_{CEO} + m\nu_r$, the resulting difference frequency (DF) is given by $\nu_1 = \nu_{DF} = (n - m)\nu_r$, i.e. it is a frequency comb with $\nu_{CEO} = 0$. If the FF (also broadened by SPM) and the DF pulses are spectrally overlapping, by their interference one gets again a beat note at ν_{CEO}. When moving from high-repetition-rate oscillators to low-repetition-rate amplified systems, it is possible to directly measure the CEP on a shot-to-shot basis [151]. Figure 16b shows the typical setup of a single-shot f–$2f$ interferometer used for CEP characterization [152]. A fraction of the pulse energy (typically a few microjoules) is first focused into a sapphire plate or a photonic crystal fiber to generate a WLC, with a spectrum extending over more than an octave. A spectral portion of the WLC is then frequency doubled in a suitable nonlinear crystal so that the SH spectrally overlaps with a portion of the FF. The collinear FF and SH, with CEPs $\varphi_1 = \varphi$ and $\varphi_2 = 2\varphi$, respectively, are sent to a spectrometer through a polarizer, that projects both polarizations onto a common axis and also adjusts their relative intensities. In most implementations, the Mach–Zehnder interferometer conceptually indicated in the figure is replaced by an inline configuration, where the FF and the SH propagate collinearly and do not accumulate additional relative phase fluctuations.

In the frequency range in which the spectrally broadened FF and the SH overlap, a spectral interference pattern is observed. According to Eq. (23) one gets

$$I(\omega) = |\tilde{E}_{FF}(\omega)|^2 + |\tilde{E}_{SH}(\omega)|^2 + 2|\tilde{E}_{FF}(\omega)||\tilde{E}_{SH}(\omega)|\cos(\omega\tau + \Delta\varphi), \quad (25)$$

where τ is the delay between FF and SH pulses and $\Delta\varphi = \varphi_2 - \varphi_1 = \varphi$ is the CEP to be characterized. If the CEP is not stable, the fringes will move from shot to shot and will vanish upon averaging. A Fourier transform of the fringe pattern allows retrieval of the CEP fluctuations on a single-shot basis. Also in this case it is possible to use the overlap between different harmonics (f–0, $2f$–$3f$, f–$3f$). It is important to notice that the nonlinearities in these interferometers inevitably carry instabilities which affect the exact estimation of CEP fluctuations. The main source of non-ideality is the phase–energy coupling occurring in the supercontinuum generation process. In the case of white-light generation in bulk media, such as fused silica [153] and sapphire [154], the coupling can be easily explained by the fact that the intensity of the input pulse determines the propagation depth at which the broadening takes place; this influences the length of free propagation and hence the group delay of the emitted supercontinuum light. Phase–energy coupling has also been observed in hollow-core-fiber-based interferometers [155], where quantitative

measurements revealed CEP deviations of the order of 128 mrad per 1% driving-pulse energy change.

5. State of the art of coherent pulse synthesis

In this section we review the current state of the art of experiments on waveform synthesis. Since the main goal of these experiments was the generation of pulses, one of the very first attempts involved the synthesis from ultrabroadband oscillators for the generation of pulses in the low-energy, high-repetition-rate regime. These pioneering works allowed the identification of the main problems posed by combining different sources, and led to elegant solutions especially for the manipulation of pulse delays. As is detailed with the examples reviewed in Section 5.1, the main challenge of this approach was the repetition-rate synchronization of independent laser sources; also for this reason, alternative approaches were then developed, based on systems driven by only one master oscillator and arranged in order to generate many synchronized broadband channels to be merged. In the family of the numerous approaches driven by one master oscillator, one of the alternative routes towards nanojoule-level ultrashort waveforms is based on fiber technology; because of their inherent stability and high repetition rates, such fiber-based synthesizers are very attractive for many experiments in extreme nonlinear optics and attoscience in solids, nanophotonics, and quantum optics, as is discussed in Section 5.2. A quite different technique for the synthesis of specific waveforms is based on the passive approach, which was developed because of the recent availability of ultrabroadband sources from hollow-core fibers. In the passive strategy, which is discussed in detail in Section 5.3, pulses with super-octave spanning spectra undergo the division of their huge bandwidth into several spectral channels; these channels are individually compressed by suitable dispersive lines and coherently recombined to sculpt the desired sub-cycle optical waveforms. In principle, each channel can also be amplified in order to scale the energy of the synthesized pulse; this approach was also successfully followed by many groups, which combined their experience on parametric amplification with coherent waveform synthesis. This approach led to a variety of schemes, involving both OPCPA (Section 5.4) and OPA technology (Section 5.5). Finally, attosecond science in the strong-field regime and even in the relativistic regime requires ultrashort high-energy pulses with controlled electric field profile, which provide the capability of coherently manipulating high-energy electron trajectories. Pulse synthesis is a promising route for the generation of such light transients; however, these processes require very high fields, which ask for suitable pulse-energy scaling of the sources described so far. Section 5.6 is entirely devoted to the challenging task of energy scaling of OPCPA-based waveform synthesizers, due to their growing importance. The main results in the microjoule to millijoule regime of pulse synthesis are summarized in Table 3.

Table 3 Summary of relevant works on waveform synthesis.

Energy	Wavelength (μm)	Scheme	Ref.
15 μJ	0.75–2.5	OPCPAs	[66]
Few μJ	0.55–1	OPAs	[65]
1 μJ	0.55–1	OPCPAs	[67]
30–300 μJ	0.35–1.1	Hollow fiber	[48]
1.4 mJ	1.4–2.3	FOPA	[156]
$\approx$ 80 mJ	0.58–1	OPCPAs	[104]

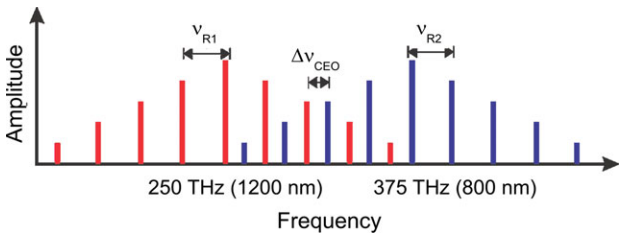

Figure 17 Requirements for coherent synthesis of pulse trains from two independent femtosecond lasers in the frequency domain.

5.1. Coherent synthesis of oscillators

Coherent synthesis of pulse trains from independent mode-locked lasers has been of great interest as a means of overcoming the bandwidth limitations of individual lasers set by the finite gain bandwidth [61–63]. Individual laser systems have already approached their gain bandwidth limit. Figure 17 shows the general principle of pulse synthesis from pulse trains in the frequency domain.

The frequency combs of both lasers have to be made equidistant, i.e. the two lasers need to be tightly synchronized and the CEO frequencies need to be matched by phase-locking a beatnote between the two frequency combs in the spectral overlap region. Shelton *et al.* were first in demonstrating the general principle by synchronizing and phase-locking two independent mode-locked sub-20 fs Ti:sapphire lasers both operating close to 800 nm [61]. They used microwave techniques for repetition rate locking and relative CEP locking. Temporal shortening of the resulting synthesized pulses, when compared to individual pulses, was observed. However, limited phase resolution, AM-to-PM conversion, and thermal drifts in microwave phase-lock loops (PLLs) limited the coherence of the synthesized pulse. Within a 160 Hz bandwidth, timing fluctuations of the pulse envelopes were suppressed to < 5 fs, a factor of about hundred below the state of the art at that time. Clearly, to achieve true synthesis of a pulse, which is indistinguishable from a pulse coming from a single source, much tighter and longer-term stable synchronization of the two sub-pulses is necessary. As guidance, a relative rms jitter equal to a tenth of an optical cycle at the center wavelength of the synthesized pulse when integrated from DC to the Nyquist frequency is a suitable specification for true

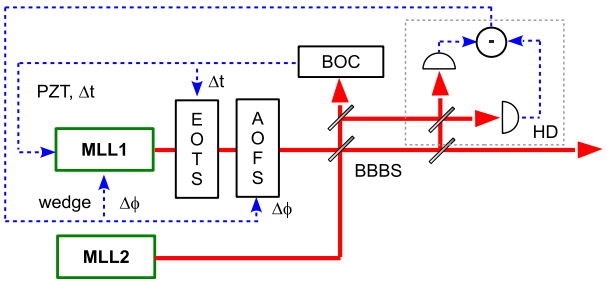

Figure 18 General schematic for coherent pulse synthesis from two independent femtosecond lasers. EOTS: electro-optical timing shifter; AOFS: acousto-optical frequency shifter; BOC: balanced optical cross-correlator; BBBS: broadband beam splitter; HD: homodyne detector.

pulse synthesis and similarly for the residual relative CEP. Such tight synchronization only became possible by the invention of the BOC technique by Schibli *et al.* [62] as discussed in Section 3.2, which reduced the timing jitter between two lasers to this level. This was done specifically for the purpose of pulse synthesis using the output of an octave-spanning Ti:sapphire laser and a broadband Cr:forsterite laser resulting in a coherent spectrum spanning from 600 nm to 1500 nm [157]. Thus the coherent synthesis of pulses from independent few-cycle ultrafast lasers presents unique challenges. It requires attosecond-precision measurement and control of the optical oscillators driven by uncorrelated technical and quantum noise to the sub-cycle level, such that a coherent frequency comb is formed, and more importantly coherent addition of the pulses in the time domain occurs with sub-cycle precision. Single-cycle optical pulse synthesis based on the coherent combination of multi-channel, nonlinear spectral generation from a single master oscillator is in that respect a technically much simpler path [64] (see Section 5.3). Such an approach renders the high-speed fluctuations in carrier phase and pulse timing between spectral channels as common mode. Attosecond-precision synchronization between uncorrelated few-cycle sources is challenging due to the requirement for high-speed detection and orthogonal control of both CEP and pulse timing with long-term stability [61, 157]. Figure 18 shows the general scheme for the synthesis of the outputs from two mode-locked lasers, MLL1 and MLL2. In one case, as we discuss below in some detail, MLL1 is a 1550 nm erbium fiber laser mode locked by nonlinear polarization evolution and MLL2 a broadband Kerr-lens mode-locked (KLM) Ti:sapphire laser. Since the noise properties of a solid-state laser are much better than those of a fiber laser due to the much higher stored pulse energy inside the laser cavity, it is better to lock the fiber laser to the Ti:sapphire cavity. In addition, the fiber laser is much more robust to intracavity pulse parameter changes. Therefore, one end-mirror of the fiber laser is moved by a piezoelectric actuator (PZT) for repetition-rate locking and a wedge is inserted into the free-space section of the laser for rough CEO frequency control. Via the PZT a coarse synchronization of both laser pulse trains within a few tenths of a femtosecond can easily be achieved and long-term drifts of ν_{CEO} can be taken out by the intracavity wedge. However, fiber lasers typically show significant high-frequency timing jitter and CEP noise, which is beyond the bandwidth of the intracavity PZT and also a wedge cannot be moved fast enough to suppress the high-frequency CEP noise. Therefore an external electro-optic timing shifter (EOTS) and an AOFS are used for fast control of pulse timing and CEO up to a few hundred kilohertz to eliminate residual high-frequency few-femtosecond timing jitter and CEO drifts. The latter technique for relative CEP locking in a feed-forward scheme by an AOFS was pioneered by Koke *et al.* [114] and allows, among other benefits, complete decoupling of the CEP control from repetition-rate control, which is for example not the case if the CEP were controlled via intracavity power, i.e. by modulating the pump power of MML2. This leads to undesired interaction of the repetition-rate lock with the CEP lock, which makes high-precision locking very difficult. Timing jitter detection is performed by a BOC and relative phase detection by a homodyne detector. Both relative pulse timing and phase are referenced to the broadband beam splitter (BBBS), where both pulse trains are combined. Therefore, once the system is locked, the synthesized output is long-term stable. This scheme was implemented using a 78 MHz repetition rate KLM Ti:sapphire laser [149, 158, 159] and a fiber supercontinuum source based on an erbium fiber laser [160] at the same pulse repetition rate, producing 6 fs and 8 fs pulses, respectively, as sketched in Fig. 19. These pulses are combined on a 50% BBBS with flat group delay and transmission characteristics from 600 nm to 1500 nm [62, 161]. The output of the Ti:sapphire master oscillator, spanning 700–1000 nm, is compressed with double-chirped mirrors (DCMs) to 6 fs, close to the TL duration. Since the Ti:sapphire laser is known to exhibit exceptionally low high-frequency timing jitter at the few-attosecond level [162], all feedback is performed upon the fiber supercontinuum source to lock it to the lower-noise Ti:sapphire laser oscillator. The fiber supercontinuum source is driven by a stretched-pulse, passively mode-locked erbium fiber laser [163]. The timing jitter of this laser was previously determined to be 2.6 fs rms from 10 kHz to the Nyquist frequency [164], by measuring the jitter between two nearly identical fiber lasers. The fiber laser pulses are amplified to 4.5 nJ in an erbium-doped fiber amplifier (EDFA) and then compressed to 60 fs duration with a silicon prism pair. An octave-spanning supercontinuum is subsequently generated in a germanium-doped, small-core highly nonlinear fiber (HNLF) as described in [160]. The short-wavelength portion of this supercontinuum (below 1.4 μm) is filtered with a knife-edge and compressed to 8 fs duration by a pair of SF10 prisms. The remaining output power is 25 to 30 mW. Half of the light combined on the BBBS is coupled into a BOC for timing synchronization [105, 106, 165]. Curved mirrors, instead of aspheric lenses, are used for focusing into the lithium triborate (LBO) crystals to avoid spatiotemporal effects that would cause the BOC to lock the pulses with a 500 fs offset. Also, a 1 μm notch filter suppresses SHG in the LBO crystals of the BOC, which would otherwise corrupt the

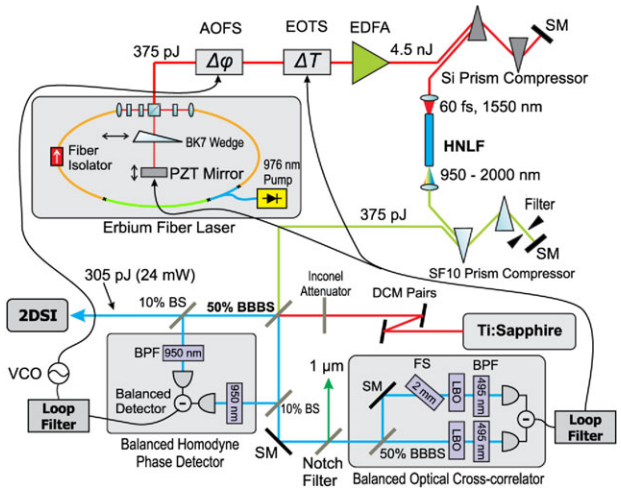

Figure 19 Schematic of coherent synthesis system which combines 8 fs fiber supercontinuum and 6 fs Ti:sapphire pulses on the 50% BBBS (center). The pulse envelope timing error is detected by a BOC and corrected via feedback upon the intracavity piezo-actuated mirror and EOTS. The CEP error is corrected by the intracavity BK7 glass wedge (slow feedback) and the AOFS (fast feedback), after detection by the balanced homodyne detector. AOFS: acousto-optic frequency shifter; EOTS: electro-optic timing shifter; SM: silver mirror; BS: beam splitter; BBBS: broadband beam splitter; FS: fused silica; BPF: bandpass filter; VCO: voltage-controlled oscillator; DCM: double-chirped mirror; 2DSI: two-dimensional spectral shearing interferometer; EDFA: erbium-doped fiber amplifier. Image from [63].

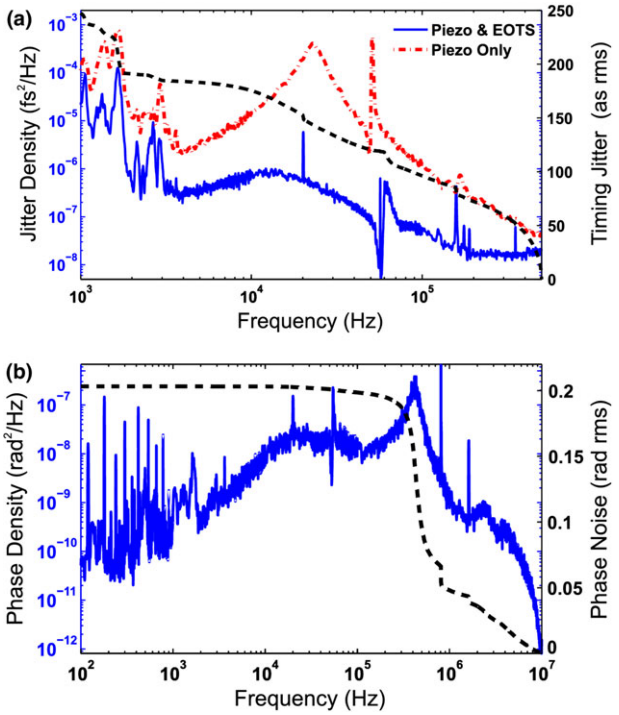

Figure 20 (a) Timing jitter spectral density and cumulatively integrated timing jitter between a fiber supercontinuum source and a Ti:sapphire master laser oscillator. The integrated timing jitter after only the intracavity piezo-actuated mirror lock (dash-dotted red) yields 2.2 fs rms residual jitter. After enabling the extracavity waveguide EOTS (solid blue), the jitter is reduced to 250 as rms, as shown by the integrated timing jitter (dashed black). (b) The residual CEP noise between the fiber supercontinuum and Ti:sapphire master laser, as measured using a balanced homodyne detector. The CEP is locked to zero offset, yielding a residual noise of only 220 mrad rms from DC to 5 MHz (detector gain bandwidth). Image from [63].

timing signal at 495 nm. As shown in Fig. 20a, feedback upon the fiber laser's intracavity piezo-actuated mirror results in 2.2 fs rms jitter [10 kHz, 1 MHz], in good agreement with previously reported results for a pair of fiber lasers [164]. Further reduction of the timing jitter to 250 as rms [1 kHz, 1 MHz], well below the single-cycle level, is obtained via fast feedback upon a waveguide lithium niobate EOTS external to the fiber laser cavity, providing a locking range of few femtoseconds. Fortunately, the electro-optic modulator imparts minimal CEP shift since the bulk of the timing jitter is at low frequencies (which is removed by the fast CEP feedback), and because the phase and group delays are to within 4% of each other for lithium niobate. After obtaining a tight timing lock, the relative CEP slip between the fiber laser and Ti:sapphire frequency comb is detected at 950 nm with a balanced homodyne detector. The difference in CEO frequencies is coarsely adjusted by varying the insertion of a BK7 glass wedge in the fiber laser. Then, fast feedback upon a low-noise, voltage-controlled oscillator (VCO) at 175 MHz is used to drive an AOFS and lock the relative CEP slip to zero. The AOFS achieves a ν_{CEO} shift of ± 5 MHz without resorting to a double-pass configuration to cancel angular walk-off. Moreover, since the narrowband optical (60 nm) output of the fiber laser is coupled into the AOFS before the EDFA and HNLF, diffractive broadening is eliminated [114]. Equally as important, feedback CEP stabilization eliminates the slow drift associated with the feed-forward stabilization. As a result, long-term stable synchronization within 220 mrad rms is achieved with 450 kHz closed-loop bandwidth, as shown in Fig. 20b. CEP shifting via pump power modulation is not possible since a nonlinear timing shift of at least 0.1 fs per round trip results from it, breaking the timing lock [166]. The BOC and balanced homodyne detector provide attosecond resolution measurement of timing and CEP difference. Precise measurement of the resulting pulse envelope is necessary to confirm proper temporal overlap and pulse compression. Accurately characterizing a nearly single-cycle pulse with conventional techniques is challenging because increasingly complex pulse characterization schemes are required to reach single-cycle resolution [64, 167, 168]. On the other hand, 2DSI has been successfully adopted for the measurement of few-cycle pulses, since it is largely unconstrained to bandwidth limitations and provides a direct measurement of spectral group delay without de-convolution ambiguities (see Section 3.2 and [66]). The 2DSI apparatus for measurement from 650 nm to 1400 nm incorporates a 30 μm thick, type-II phase-matched BBO crystal. An

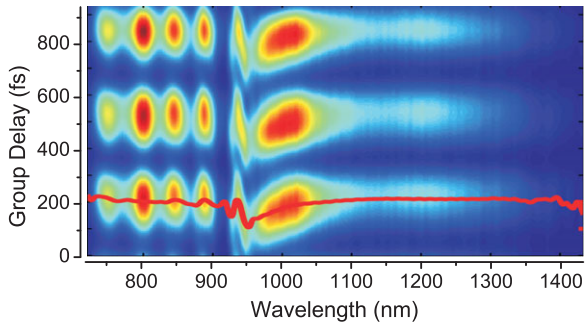

Figure 21 2DSI after laser synchronization. Spectral group delay (red line) is directly retrieved from the location of the interference fringes. When group delay information and directly measured optical spectrum are combined, the Fourier transform yields the pulse envelope.

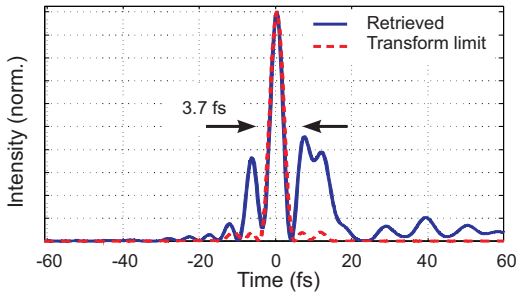

Figure 22 Retrieved pulse intensity (blue solid line) as measured by 2DSI. Pulse duration is 3.7 fs FWHM, or 1.1 cycles at the carrier wavelength of 1 μm. For comparison, the TL temporal intensity profile $I(t)$ is shown (red dotted line).

interferogram of the synchronized output is shown in Fig. 21 and reveals spectrally flat group delay over the entire bandwidth, with the exception of the portion near 950 nm, where the third-order dispersion of the SF10 prisms and DCMs increases. The spectral group delay retrieved from 2DSI is combined with a measurement of the fundamental optical power spectral density to yield the complex spectrum. As shown in Fig. 22, the central peak of the pulse coincides with the TL temporal intensity profile, and has a full width at half maximum (FWHM) intensity duration of only 3.7 fs, or 1.1 optical cycles at 1 μm. Such single-cycle pulses have been pursued for a long time to study phase-sensitive nonlinear optics, including optically driven field emission [169] and carrier-wave Rabi flopping [43, 170].

5.2. Coherent synthesis of fiber lasers

An alternative route toward nanojoule-level single-cycle waveforms different from bulk solid-state oscillators is based on fiber technology [64]. Due to their excellent inherent stability and multi-megahertz repetition rates, such nanojoule-level fiber-based waveform synthesizers are very attractive for many experiments in extreme nonlinear optics and attoscience in solids, nanophotonics, and quantum op-

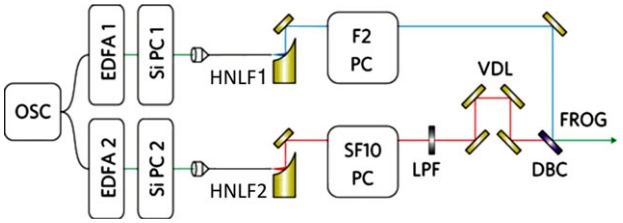

Figure 23 Scheme of a fiber-based single-cycle waveform synthesizer. OSC: femtosecond erbium-doped fiber oscillator; EDFA: erbium-doped fiber amplifier; Si PC: silicon prism compressor; HNLF: bulk highly nonlinear fiber; F2/SF10 PC: pulse compressors using F2 and SF10 Brewster prisms; LPF: low-pass filter (1600 nm cutoff wavelength); VDL: variable delay line; DBC: dichroic beam combiner. Figure adapted from [64].

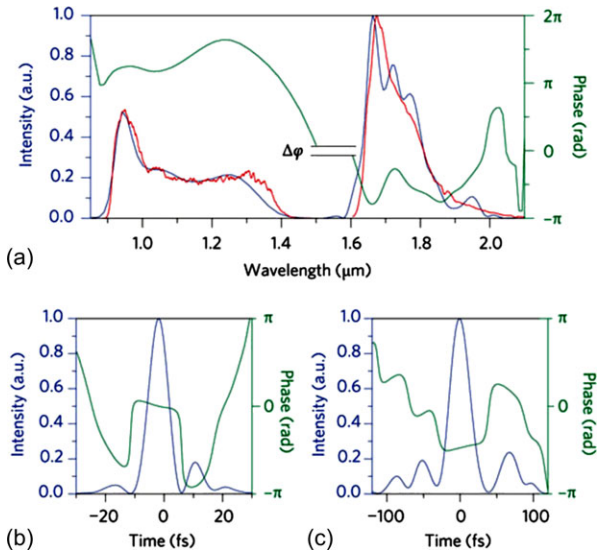

Figure 24 Interferometric SHG-FROG characterization of the two channels. (a) Measured spectra (red curves), retrieved spectral intensity (blue), and phase (green) of the dispersive wave centered at 1125 nm and soliton at 1770 nm. The retrieved temporal intensity (blue) and phase profiles (green) of the (b) dispersive wave and (c) soliton exhibit 7.8 fs and 31 fs FWHM durations, respectively. Figure from [64].

tics. Recently, Krauss *et al.* [64] reported synthesis of 4.3 fs single-cycle waveforms based on erbium-doped fiber technology. As shown in Fig. 23, a common 40 MHz erbium-doped fiber oscillator seeds two parallel channels. In both channels the seed pulses are then amplified in EDFA1,2 to $\approx$ 8.2 nJ energy and compressed in free space using silicon prism compressors. To obtain broad optical bandwidths required for ultrashort waveform synthesis, these amplified pulses are spectrally broadened in two different germanosilicate HNLFs. A careful choice of the pre-chirp of the prism compressors in combination with different zero-dispersion wavelengths of the HNLF1,2 results in a dispersive wave centered at 1125 nm and a broadband soliton at 1770 nm, as shown in Fig. 24a. The outputs of both channels were compressed using prism pairs and individually characterized

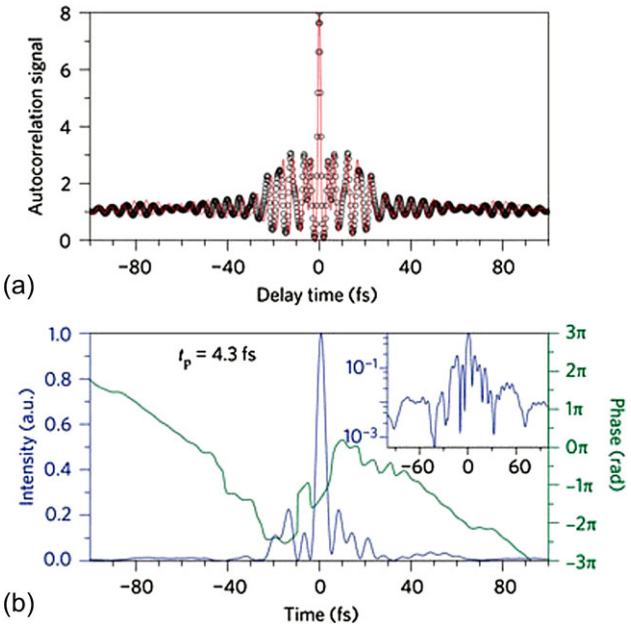

Figure 25 Optimum synthesized 4.3 fs single-cycle waveform. (a) Second-order autocorrelation trace measured for optimum temporal overlap (red curve) and computed from the FROG results in Fig. 24a and a least-squares fit varying Δt and $\Delta\varphi$ (black circles), yielding $\Delta t = 400$ as and $\Delta\varphi = -0.5$ rad. (b) Temporal intensity profile (blue) and phase (green) of the synthesized 4.3 fs waveform. The inset shows the temporal intensity profile on a logarithmic scale. Figure from [64].

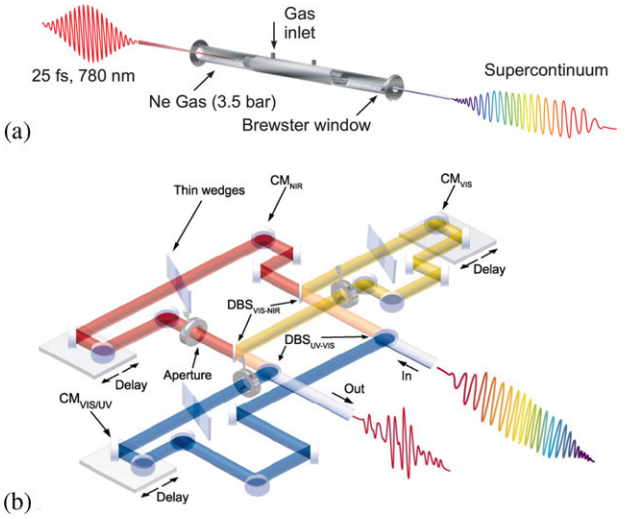

Figure 26 (a) Supercontinuum generation in a neon-filled hollow-core fiber. From [139]. (b) Schematic representation of a three-channel light-field synthesizer. From [48]. DBS: dichroic beam splitter; CM: chirped mirror.

by interferometric SHG-FROG, yielding the pulse retrieval results depicted in Fig. 24. A convenient aspect of this two-channel fiber synthesizer is that the timing jitter between the two channels in free-running operation is already < 50 as rms (1 Hz up to the Nyquist frequency of 20 MHz), i.e. no active feedback stabilization of the relative timing is required for the synthesis. The next task was to set the optimum conditions (for the intensity ratio I_1/I_2, time delay Δt, relative phase $\Delta\varphi$) for the synthesis of the shortest possible waveforms and to fully reconstruct them in amplitude and phase. As discussed above, the individual channels were already individually characterized by FROG, and the intensity ratio could readily be obtained using a calibrated spectrometer. To obtain the time delay Δt and relative phase $\Delta\varphi$, Krauss and co-workers measured the interferometric second-order autocorrelation (see Fig. 25a) using the two-photon-absorption photocurrent from a GaAs photodiode. By means of a least-squares fit to the experimental autocorrelation trace, optimum values of $\Delta t = 400$ as and $\Delta\varphi = -0.5$ rad were obtained resulting in the optimum synthesized 4.3 fs single-cycle waveform shown in Fig. 25.

5.3. Passive waveform synthesizers

One strategy towards sub-cycle waveform synthesis consists of the generation of super-octave spanning spectra, followed by division of the huge bandwidth into several spectral channels, which are individually compressed by dispersive delay lines and coherently recombined to synthesize sub-cycle optical waveforms [48, 139]. The scheme starts with an amplified Ti:sapphire laser, generating 25 fs pulses (with 70 nm bandwidth) at 780 nm with energy $> 800\,\mu$J and repetition rate of a few kilohertz. These pulses are focused into a hollow-core fiber [6] (1.1 m in length, 250 μm inner diameter) filled with neon (Fig. 26a). The gas pressure is kept rather high (3 to 4 bar) to maximize spectral broadening by triggering in the hollow-core fiber, in addition to SPM, other nonlinear processes, such as optical shock-front formation or four-wave mixing between remote spectral components of the pulse [171]. The resulting output pulses have energy $> 500\,\mu$J and a spectrum spanning more than two octaves, with content in the wavelength range from 260 to 1100 nm (Fig. 27a). The CEP of the pulses is actively stabilized using a double-feedback loop: a first "fast" (kilohertz bandwidth) loop acting on the Ti:sapphire oscillator and stabilizing ν_{CEO}, and a second "slow" (a few tens of hertz bandwidth) loop after the hollow-core fiber compensating for CEP drifts induced by the amplification and the nonlinear spectral broadening processes. The second loop uses a compact f–$2f$ interferometer exploiting the multi-octave nature of the hollow-core fiber pulse. The resulting rms CEP fluctuations are <100 mrad. The spectrum at the output of the hollow fiber is divided, by custom-designed chirped dichroic beam splitters (DBSs), into three channels: a NIR one ($\mathrm{Ch_{NIR}}$, 700–1100 nm), a visible one ($\mathrm{Ch_{VIS}}$, 500–700 nm), and a visible–UV one ($\mathrm{Ch_{VIS-UV}}$, 350–500 nm), as sketched in Fig. 26b. Pulses in the three channels are compressed individually by multiple bounces on pairs of CMs, designed for the respective wavelength range. Since each CM pair must work over a relatively narrow bandwidth (less than half an octave), their design

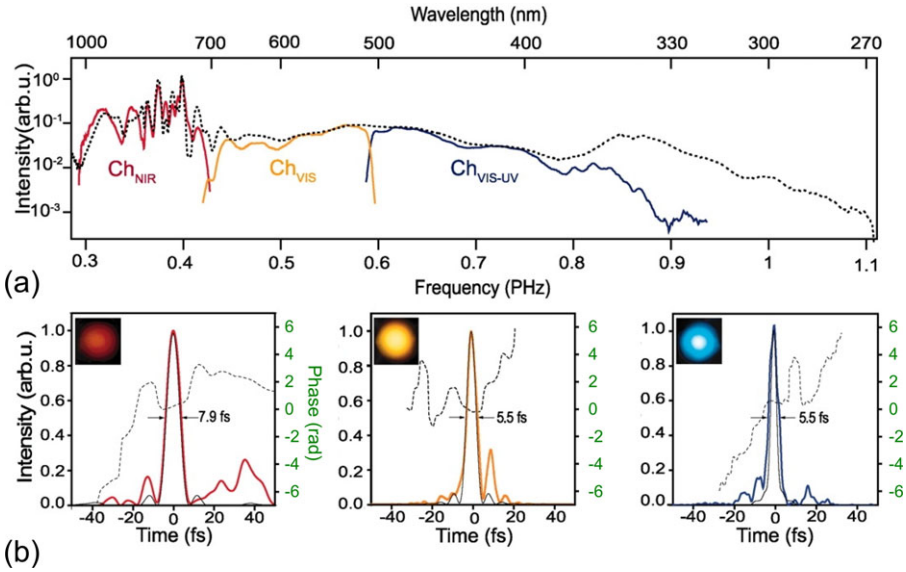

Figure 27 Three-channel hollow-core fiber-based synthesizer. (a) Dotted line: spectrum generated by the hollow-core fiber; solid lines: spectra from the three channels Ch_{NIR} (red line), Ch_{VIS} (orange line), and Ch_{VIS-UV} (blue line). Insets are beam profiles of the individual channels. (b) Temporal intensity (solid lines) and phase (dotted lines) profiles retrieved from transient-grating FROG measurements of the three channels, and corresponding TL intensity profiles (shown as thin black lines). Figure from [48].

is quite relaxed and they feature a high-energy throughput. In addition to the CMs, a pair of thin fused silica wedges is inserted in each channel to finely tune the dispersion as well as the CEP of the individual sub-pulses. Each channel is characterized by transient-grating FROG [172], which is a technique working over a very broad wavelength range, and thus suitable for characterizing all three channels. After optimization, the resulting FWHM pulse durations for the three channels are $\tau_{NIR} = 7.9$ fs, $\tau_{VIS} = 5.5$ fs, and $\tau_{VIS-UV} = 5.5$ fs (Fig. 27b), very close to their TL values, indicating nearly optimum compression of the pulses. The same set of DBSs is used to recombine the pulses after spectral phase manipulation, resulting in an overall energy of 300 μJ (250 μJ in Ch_{NIR}, 36 μJ in Ch_{VIS}, and 14 μJ in Ch_{VIS-UV}). In order to phase-lock the different sub-pulses, a delay line is present in each channel, which consists of a manual translation stage (for coarse delay adjustment) and a piezoelectric stage (for fine adjustment). Delay stabilization is first of all achieved passively, by building the three-channel interferometer in a compact, quasi-monolithic setup shielded from atmospheric turbulences and temperature stabilized within 0.1°. As this is not sufficient to prevent long-term drifts, active stabilization is implemented, exploiting the partial spectral superposition of adjacent channels enabled by the imperfect polarization of the broadband pulse at the output of the hollow fiber and by the broader transmission bandwidth of the DBS for the *s* with respect to the *p* polarization. By projecting the two transmitted *p* and *s* polarizations, which are also time delayed due to the polarization-dependent dispersive properties of the dielectric optics, along the same polarization direction through a Glan–Thompson polarizer, spectral interference fringes are obtained, which contain information on the relative phase between adjacent channels (see Section 4.2.1). Fringes between Ch_{NIR} and Ch_{VIS} as well as those between Ch_{VIS} and Ch_{VIS-UV} are detected by a spectrometer and used to generate error signals for the feedback loops acting on the piezoelectric stages, allowing one to achieve long-term phase locking between different channels.

A crucial point for the synthesis over such ultrabroad bandwidth is the spatial superposition of the different channels, which should be wavefront-matched in order to focus in the same spatial plane. For this purpose, any wavefront distortion introduced on the individual channels by the DBSs, mirrors, and wedges must be carefully compensated for. The DBSs are carefully designed to avoid spatial curvature effects introduced by the coating strain, which may result in different radii of curvature for the reflected and transmitted beams; the thickness of the anti-reflection coating on the back side of a DBS is optimized to minimize this effect. For finer divergence adjustment, each channel is equipped with a nominally flat mirror, whose curvature can be adjusted using a micrometer screw. This allows one to achieve nearly perfect matching of the beam waists and the focal planes in the focus of a spherical mirror. Once the synthesis is complete, full characterization of the optical waveform is achieved by the technique of attosecond streaking (see Section 4.1.3), which uses an isolated attosecond XUV pulse to sample the electric field of the optical waveform [29, 173]. In the experimental setup, shown in Fig. 28, the synthesized pulse is focused to an intensity of $\approx 10^{14}$W/cm^2 into a vacuum chamber containing a quasi-static cell filled with neon (at 200 mbar pressure). Interaction with the gas produces, by the HHG process, an XUV pulse which propagates collinearly with the synthesized light transient. The XUV pulse is bandpass filtered (13 eV bandwidth centered at 85 eV) by a combination of multilayer optics and thin metal foils, resulting in the generation of an isolated attosecond pulse. Both the XUV and the optical pulses impinge on a two-component delay mirror module, which allows varying (because of a piezoelectric stage attached to the inner mirror) their relative delay with attosecond precision. The pulses are finally focused on a second neon gas jet and the kinetic energy of the photoelectrons is measured by a TOF spectrometer

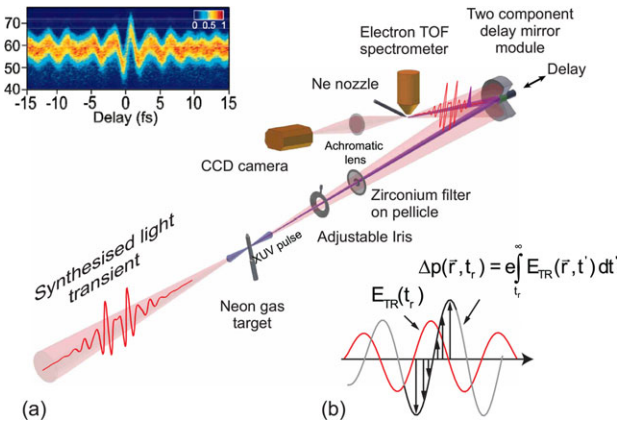

Figure 28 Characterization of the synthesized optical waveform by the attosecond streaking technique. (a) An isolated attosecond XUV pulse, generated by HHG in a neon-filled gas cell and propagating collinearly with the optical waveform, ionizes a second gas target and (b) the kinetic energy of the photoelectrons is measured with a TOF spectrometer as a function of the delay between XUV and optical pulses. Inset: example of a streaking spectrogram. Figure adapted from [139].

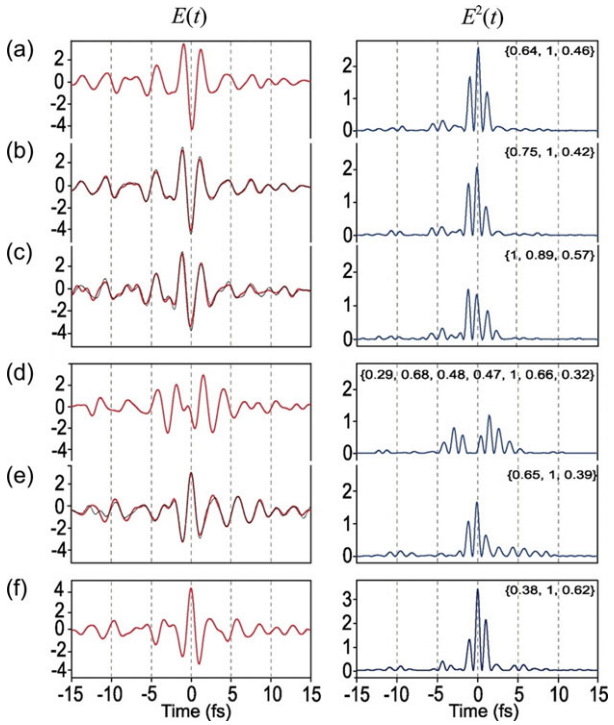

Figure 29 Electric field retrieved from attosecond streaking spectrograms (left-hand panels) and corresponding $E^2(t)$ profiles (right-hand panels). Relative intensities for the most intense field crests – normalized to the maximum – are given in brackets. (a–c) The delay of Ch_{VIS-UV} is varied in steps of 200 as ($\approx \pi/4$). (d) Relative delays and CEPs of the individual channels are adjusted so as to create twin transients with a field minimum between them. (e) Ch_{NIR} is delayed by 1.45 fs ($\approx \pi$), resulting in a high-frequency leading transient followed by a low-frequency tail. (f) The pulse carries less than one optical cycle in its FWHM envelope intensity profile, corresponding to a 2.1 fs pulse width. Figure from [48].

as a function of the delay between XUV and optical pulses, thus obtaining a laser-field-streaked photoelectron spectrogram. In this spectrogram the attosecond pulses sample the electric field of the optical waveform in a way analogous to electro-optic sampling commonly used for terahertz radiation [174]. The retrieved duration of the XUV pulse, which is less than 200 as, indicates that it can accurately sample even the highest frequency component of the synthesized pulse (which is 900 THz, corresponding to a period of 1.1 fs). Attosecond streaking allows, on the one hand, full characterization of the synthesized optical waveform and, on the other hand, the extraction of the parameters required for on-demand synthesis of the optical field. Figure 29 shows a series of temporal profiles of the electric field $E(t)$ and the corresponding $E^2(t)$. From 29a–c the relative delay of the channel Ch_{VIS-UV} is increased in steps of 200 as (corresponding to a phase shift of $\pi/4$); the excellent agreement between the measured electric field profiles in Figs. 29b and c (solid lines) and the calculated ones (dotted lines) demonstrates the capability of optical waveform shaping, according to a predefined pattern, at the sub-cycle level. The $E^2(t)$ profiles, shown in the right-hand panels of Fig. 29, demonstrate substantial changes in the relative intensities of the subsequent sub-cycles obtained with the shaping. In Fig. 29d the delays and the CEPs of the channels are adjusted in such a way so as to create two peaks separated by 4.5 fs with nearly zero in between. Finally the transient in Fig. 29f has the shortest duration, with an envelope intensity FWHM of 2.1 fs. The synthesizer has meanwhile been upgraded by the addition of a fourth channel, Ch_{UV-VUV}, which covers the wavelength range from 260 to 350 nm [175]. This corresponds to a very large additional bandwidth ($\approx$ 400 THz), leading to a bandwidth of the synthesized pulse which covers more than two octaves. For pursuing the synthesis of the shortest possible pulses within this four-channel scheme, the total output energy is limited mainly by the VUV channel containing the smallest pulse energy, which might not be sufficient for many interesting applications in attoscience.

A potential solution is the application of induced-phase modulation (IPM) [176] based on the interaction between two (or more) co-propagating optical pulses of different color and relatively long pulse duration in a gas-filled hollow-core fiber. The IPM technique offers control over the spectral shape by adjusting the relative intensity ratio and the relative delay between the input pulses and allows a more efficient generation of ultrabroadband optical pulses than those produced solely by SPM. A synthesizer in which the broadband pulses are obtained with IPM instead of SPM only is expected to greatly relieve the energy-scaling bottleneck due to the weak UV region [177, 178], and the enhanced spectral broadening of the UV region is particularly appealing for the realization of ultrahigh-harmonic generation conversion efficiencies in bright tabletop HHG sources. An IPM-based optical waveform synthesizer powered by a

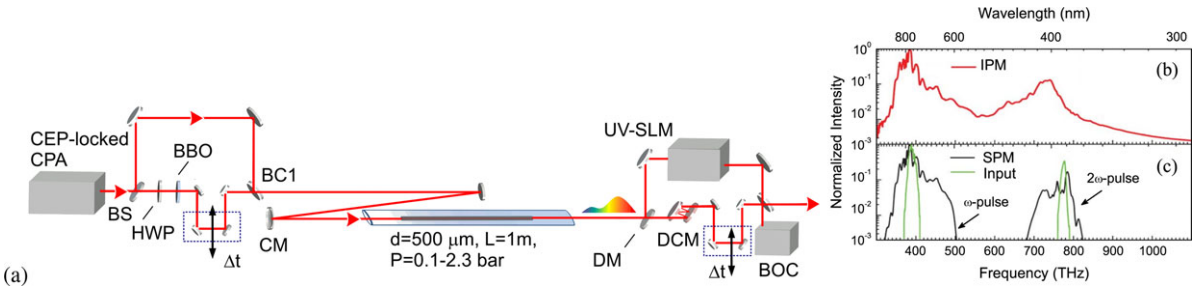

Figure 30 Sub-femtosecond IPM-based optical waveform synthesizer. (a) Experimental setup: BS, beam splitter; BBO: β-barium borate crystal; HWP: half-wave plate; BC: beam combiner; CM: concave mirror; DM: dichroic mirror; DCM: double-chirped mirror; SLM: spatial light modulator; BOC: balanced optical cross-correlator. (b) Experimental output spectrum when FF and SH pulses are co-propagating at optimal delay time. (c) The corresponding experimental spectra for SPM only (black line) and for input pulses (green lines). Data from [179].

CEP-stabilized Ti:sapphire chirped-pulse amplifier (CPA) system is shown in Fig. 30a. One replica of the laser beam is guided into a type-I BBO crystal for the generation of the SH pulse. The SH pulse is then temporally and spatially overlapped with the other portion of the FF pulse, and both pulses are focused into a gas-filled hollow fiber. Harmonic separators (HSs) filter out the residual FF pulses from the SH pulses, and adjust the time delay Δt for optimum IPM spectrum. The supercontinuum broadened by SPM and IPM in the hollow fiber is steered into two different wavelength channels by using a broadband dichroic mirror; the different spectral regions are subsequently individually compressed by custom-designed DCMs and a UV-SLM [180]. In addition to the attosecond streaking, the $>$ 2-octave sub-cycle optical waveforms can also be fully characterized using 2DSI [134, 181]. By employing the advantages of IPM, an isolated 1.3-cycle pulse with 2.6 fs duration and 3.6 μJ energy centered at 600 nm was first demonstrated in 2007 [176]. Later, much broader spectra (270–1000 nm; Fig. 30b and c) with 800 μJ have been generated, supporting 1.5 fs TL pulses [179]. Most recently, an above-mJ IPM-based waveform synthesizer driven by a CEP-stabilized CPA system was demonstrated for the first time. Using a neon-filled fused silica hollow-core fiber, a 1.7 mJ CEP-locked supercontinuum spanning the range 340–950 nm was achieved [178], which is straightforwardly compressible to terawatt optical waveforms. We foresee that this high-energy sub-femtosecond synthesizer will become a versatile tool for nonlinear attosecond optics experiments [21].

5.4. Coherent synthesis of OPCPAs

OPCPAs provide numerous advantages for ultrashort pulse amplification [182, 183]. In addition to the advantages of OPAs, such as gain bandwidths exceeding those achievable with conventional stimulated-emission-based amplifiers or in spectral regions where no such gain media exist, high gain in a short path length, thus minimizing the B-integral, amplification only when a pump pulse is present, thus minimizing amplified spontaneous emission pre-pulse pedestals, and low thermal loading, thus reducing spatial aberration of the beams and CEP drift, the use of a chirped signal pulse has several advantages. One is the scalability to higher pulse energies, since the maximum intensity and beam size are determined by damage and self-focusing thresholds, and maximum crystal aperture sizes, respectively. Another advantage is a reduction in sensitivity to material dispersion during amplification, since the pulses, though possessing ultrabroad bandwidth, are already picoseconds in duration. Finally, OPCPAs allow one to use today's picosecond high-average-power lasers as pump sources. These amplifiers can deliver hundreds of watts and even up to kilowatt level, well above the average power ceiling of Ti:sapphire amplifier technology. Together, these attributes allow OPCPAs to push the limits of high-peak-power and high-average-power pulse generation into spectral regions in which broadband laser amplification has not been developed, thus making them an important enabling technology for future strong-field and attosecond science.

In addition to the inherent advantages of OPCPAs as broadband amplifiers, the use of multiple OPCPAs in a coherent waveform synthesis architecture has a number of distinct advantages over other technologies. One of the primary advantages is the ability to seamlessly extend the dispersion management systems of the individual OPCPAs for phase shaping of the synthesized pulse. The requirement of an OPCPA system to have picosecond-scale chirp management of the signal pulses entails that the system already contains the means to both coarsely and finely control the chirp of the synthesized pulse, with the phase control devices (e.g. an AOPDF) built into the individual amplifiers. The average-power scalability of OPCPA technology is another key advantage, since the average power of the synthesizer should scale with that of the individual OPCPAs. The only additional requirements of the synthesizer are that the high-average-power amplification stages do not introduce significant timing jitter and that the beam combiner can scale to high average power and without introducing excessive B-integral.

The first demonstration of an OPCPA-based pulse synthesizer was reported in [66, 184]. The system, sketched in Fig. 31, demonstrates the coherent synthesis of two ultrabroadband OPCPAs for the generation of fully controlled

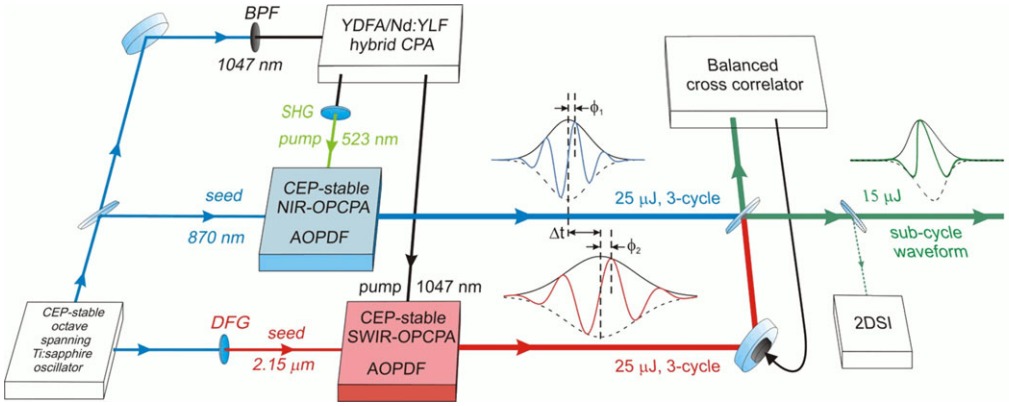

Figure 31 Scheme of the high-energy OPCPA waveform synthesizer from [66]. BPF: bandpass filter; SHG: second-harmonic generation crystal; DFG: intrapulse difference-frequency generation module; AOPDF: acousto-optic programmable dispersive filter.

high-energy non-sinusoidal optical waveforms with spectra spanning close to two octaves. This work was motivated by the prior successful implementation of ultrabroadband OPCPA systems at $\approx 0.8\ \mu$m and $\approx 2.1\ \mu$m wavelengths that were seeded by a Ti:sapphire oscillator front-end and pumped by NIR, picosecond-duration amplifiers. The short-wavelength infrared (SWIR) design employed periodically poled lithium niobate and lithium tantalate OPCPA stages in a degenerate, collinear geometry, with amplification at $\approx 2.1\ \mu$m pumped by a picosecond pulse at $\approx 1.05\ \mu$m wavelength [127,185,186]. The NIR design employed BBO OPCPA stages in a non-collinear geometry, with amplification at ≈ 800 nm pumped by a visible picosecond pulse produced by frequency doubling a picosecond amplifier at $\approx 1.05\ \mu$m wavelength [187–190]. These results suggest that the two wavelengths of operation can employ common seed and pump lasers. The synthesizer design of [66, 184] is further motivated by the ability to scale to higher-power pump lasers based on cryo-Yb:YAG, as discussed in Section 5.6. The OPCPA-based pulse synthesizer combines two CEP-controlled few-cycle pulses obtained from the mentioned NIR and SWIR OPCPAs. The NIR OPCPA produces 25 μJ, 9 fs pulses centered at 870 nm; the SWIR OPCPA provides 25 μJ, 24 fs pulses at 2.15 μm. The coherence of the two OPCPA pulses to within environmental fluctuations and drifts on subsequent beam paths is ensured by the use of a single, actively CEP-stabilized, octave-spanning Ti:sapphire oscillator as the front-end for both OPCPAs. The inclusion of an AOPDF in each OPCPA allows independent spectral phase and amplitude adjustment of each pulse, enabling control and optimization of the synthesized sub-cycle waveform. Outputs from the two OPCPAs are combined in a broadband neutral beam splitter.

The resulting spectrum spans over 1.8 octaves (blue lines in Fig. 32a), and the energy of the synthesized pulse is 15 μJ, at a repetition rate of 1 kHz. Besides the spectral phases (controlled by the AOPDFs), three other independent parameters determine the synthesized electric field waveform: the CEP of the NIR OPCPA pulse (ϕ_1), the CEP of the SWIR OPCPA pulse (ϕ_2), and the relative timing between the two OPCPA pulses (Δt). Precise stabilization

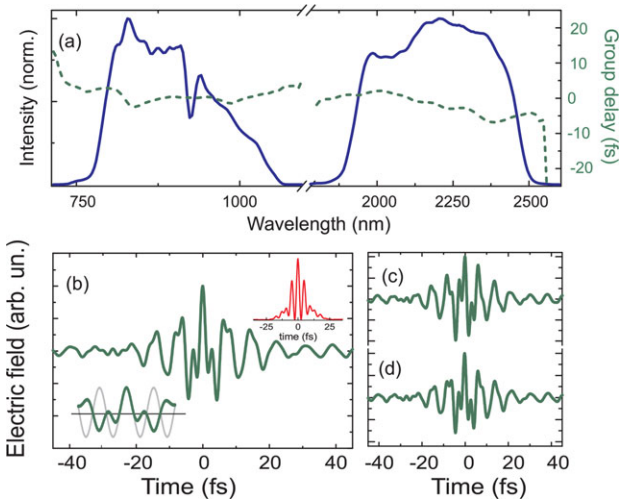

Figure 32 (a) The optical spectrum (blue lines) and the wavelength-dependent group delay (green dashed lines) of the synthesized waveform. (b) The synthesized electric field waveform assuming CEPs ($\phi_1 = 650$ mrad, $\phi_2 = -750$ mrad) optimal for achieving the shortest high-field transient, with an amplitude FWHM which lasts only 0.8 cycles of the centroid frequency. Lower inset: the synthesized waveform is superimposed with the electric field oscillating at the centroid period of 4.2 fs. Upper inset: profile of the corresponding intensity. (c) A synthesized waveform by adding 500 mrad to both ϕ_1 and ϕ_2. (d) A synthesized waveform by adding 1 fs to Δt. Data from [66].

of these three parameters is required for coherent synthesis of the two OPCPA pulses (see Section 3), and subsequent control of each parameter allows precise waveform shaping. Although the CEP of the SWIR OPCPA is passively stabilized due to the intrapulse DFG [116] used to produce its seed, an active feedback loop on the oscillator ensures the CEP stability of the NIR OPCPA. The CEP stability of the two individual pulses shows fluctuations with standard deviations as low as 135 mrad and 127 mrad, respectively. A feedback loop based on a BOC (see Section 3.2) synchronizes the two pulses, allowing relative timing stability

with attosecond precision. With the feedback control of the SWIR OPCPA's path length over a bandwidth of 30 Hz, the relative timing drift is reduced to 250 as, less than 5% of the oscillation period of the SWIR OPCPA (7.2 fs). Once the BOC-based feedback loop stabilizes the relative timing between the two OPCPA pulses, 2DSI (see Section 4.1) is used to measure the frequency-dependent group delay of the synthesized waveform. Figure 32a shows (green dashed lines) the extracted frequency-dependent group delay of the synthesized field, which is the derivative of the spectral phase with respect to frequency. The 2DSI measurement shows that each OPCPA pulse is well compressed to within 10% of its TL pulse duration.

Figure 32b shows a synthesized electric field waveform and intensity profile assuming CEPs optimal for achieving the shortest high-field transient, with an amplitude FWHM which lasts only 0.8 cycles of the carrier (centroid) frequency, 1.26 μm. The lower inset of Fig. 32b shows that the synthesized electric field waveform is non-sinusoidal, and the main feature lasts less than an optical cycle. As an example of waveform sculpting made possible by tuning the parameters of the system, Fig. 32c,d shows two non-sinusoidal waveforms as the CEP and relative timing are changed. Because of the large gap in the combined spectrum, there are two wings at $\pm$4.8 fs from the central peak, as shown in Fig. 32b. For processes initiated by strong-field ionization near the peaks of the pulse, these wings have a negligible effect due to the exponential dependence of the tunneling rate on electric field strength. For more demanding applications, the wings could be suppressed by extension of the coherent wavelength multiplexing scheme to include a third OPCPA, centered at 1.5 μm [9], to fill the spectral gap.

5.5. Coherent synthesis of OPAs

Coherent combination of ultrabroadband OPAs is a promising route to single-cycle and even sub-cycle waveform synthesis. OPAs are powerful tools for the generation of tunable few-cycle light pulses [191]. Broadband gain in an OPA is achieved when the group velocities of signal and idler are matched [14]; this condition is satisfied either in the case of a degenerate OPA (DOPA) with type-I phase matching or in the case of a non-collinear OPA (NOPA), where the idler group velocity projected along the signal propagation direction is matched to the signal group velocity. Using these concepts, a variety of broadband OPA schemes, pumped by either the FF or the SH of Ti:sapphire and Yb-based lasers, have been demonstrated. In particular, with Ti:sapphire sources sub-10 fs visible pulses (500–700 nm) are routinely generated by the SH-pumped NOPA [13], and sub-7 fs pulses have been obtained in the 650–950 nm spectral region by the SH-pumped DOPA [192]. Tunability can be extended even more by pumping with the SH and the third harmonic (TH) of Yb-based lasers, which allows the generation of pulses shorter than 20 fs throughout a spectral range spanning from 395 to 970 nm [193], at

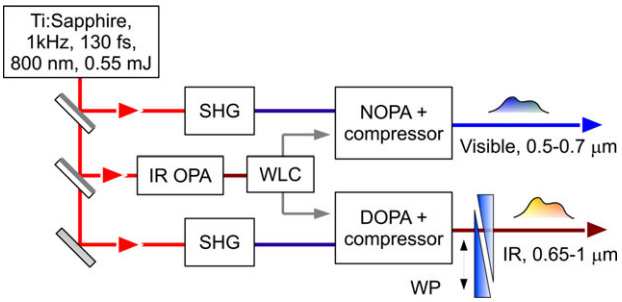

Figure 33 Setup for parallel amplification and compression of visible and IR pulses with OPAs. SHG: second-harmonic generation; WP: fused silica wedge pairs for the tuning of the visible–IR relative carrier phase.

repetition rates up to 1 MHz. In the following subsections, we provide examples of waveform synthesizers based on OPAs. We explore various architectures employing parallel and sequential approaches, powered by Ti:sapphire and Yb-based lasers.

5.5.1. Low-energy OPAs

The coherent synthesis of ultrabroadband low-energy OPAs has been reported by Manzoni *et al.* [65]. In this scheme, coherent synthesis is obtained within a parallel approach. The parent pulses are derived from two spectrally adjacent ultrabroadband NOPA and DOPA powered by a Ti:sapphire laser and seeded by the same WLC; coherent synthesis from these sources results in ultrabroadband (520–1000 nm) spectra supporting nearly single-cycle sub-4 fs pulses. After compressing the individual sub-pulses with CMs, the synthesized pulse has a nearly TL 3.8 fs duration (1.6 cycles at 700 nm).

The experimental setup for coherent synthesis of OPAs, summarized in the block diagram of Fig. 33, consists of (i) a WLC seed generation stage, (ii) two broadband OPAs seeded by distinct portions of the WLC. The system is powered by an amplified Ti:sapphire laser providing 550 μJ, 130 fs pulses at 800 nm and 1 kHz. Since the WLC presents highly structured intensity and spectral phase profiles around the driving pulse wavelength, it is not possible to use the WLC directly generated by the FF to seed the DOPA. Therefore an additional stage is necessary to shift the WLC driving wavelength to the IR, thus generating a well-behaved WLC around 800 nm [192]. This two-stage IR OPA, using type-II BBO crystals, is pumped by the FF of Ti:sapphire (250 μJ) and seeded by the supercontinuum generated in a sapphire plate [194]. Both the signal and the passively CEP-stable idler [116, 195] from the IR OPA can be used to generate the WLC seed [196]. For this preliminary experiment the seed is generated by the signal at 1.3 μm in a 3 mm thick sapphire plate; for the synthesis of a pulse with reproducible electric field, the seed has to be generated from the CEP-stable idler. The short-wavelength portion of this seed ranges from 500 to 1000 nm, and

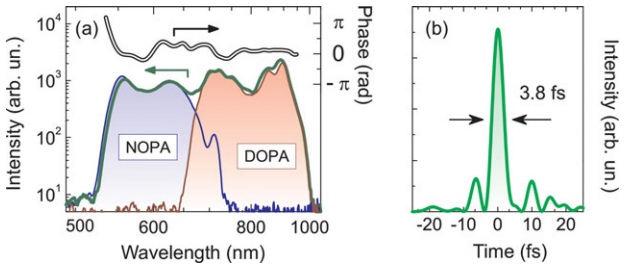

Figure 34 Parametric waveform synthesizer. (a) Spectra of the light delivered by each OPA and of the synthesized beam. Right vertical axis: spectral phase deduced from 2DSI measurement of the synthesized pulse. (b) Temporal intensity profile $I(t)$ of the pulse envelope deduced from the spectrum and phase of (a).

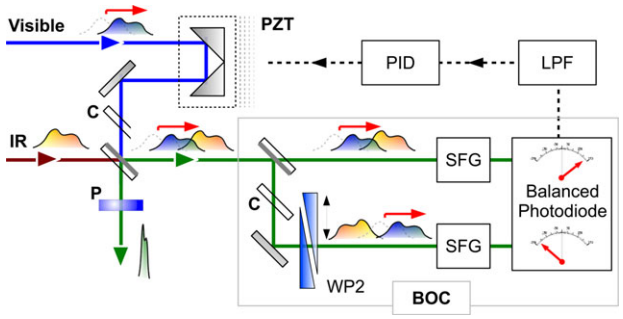

Figure 35 Schematic of the synthesizer and the BOC. PZT: piezoelectric actuator; WP2: CaF_2 wedge pair for delay tuning; P: 2 mm thick CaF_2 plate; C: compensation plates; LPF: electronic low-pass filter; SFG: sum-frequency generation; PID: proportional–integral–derivative controller.

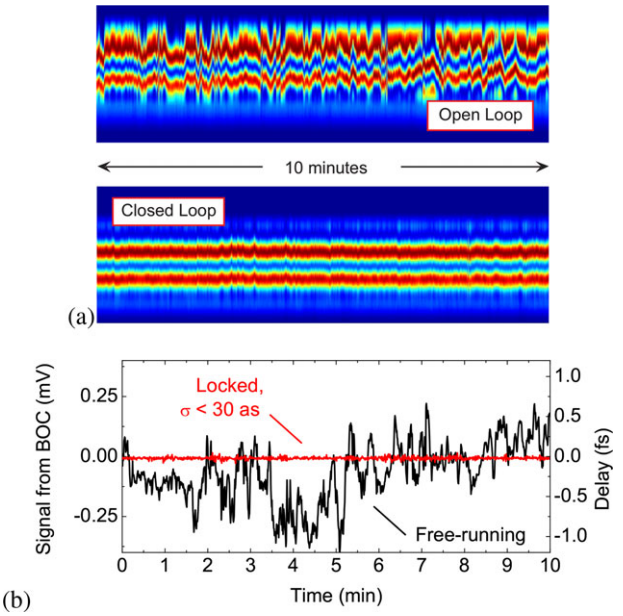

Figure 36 Characterization of the relative delay between the parent pulses. (a) Spectral interference pattern in the overlapping spectral region of the parent pulses. Upper panel: the relative delay between the pulses is not stabilized; lower panel: the feedback loop locks the relative delay. (b) Signal from the BOC in the two configurations (from [65]).

covers the gain range of the visible NOPA and SH-pumped DOPA. The seed is split with a neutral-density ultrathin beam splitter, and the two replicas are amplified with the blue-pumped visible NOPA and DOPA. Each OPA generates pulses with 1–2 μJ energy and with spectra shown in Fig. 34a as shaded areas. The two OPA outputs are individually compressed by broadband visible [197] and IR [62] CMs, which provide pulse durations close to the TL values ($\approx$ 7 fs for both OPAs). The two amplified pulses are then synchronized with a delay line equipped with a PZT, and collinearly combined with an ultrathin metallic beam splitter with spectrally flat 50:50 splitting ratio. Figure 34a also shows the gap-free spectrum arising from the combination of the two pulses: it ranges from 520 to 1000 nm with very good spectral uniformity and supports a TL 3.65 fs pulse duration.

The last step of the pulse synthesis is the coherent combination of the two pulses, which calls for careful control of their chirp and AP. The AP can be finely tuned by the wedge pair WP1. The relative delay between the two pulses is detected with the BOC [157] sketched in Fig. 35, where two replicas of the synthesized pulse with opposite chirp are cross-correlated in 1 mm thick BBO crystals, phase matched for SFG of 600 nm light from the NOPA and 800 nm light from the DOPA. The compensating plates C have the same substrates as the beam splitters, and provide equal replicas in the two BOC arms; plate P compensates for the negative chirp and allows one to obtain compressed synthesized waveforms. Because of balanced detection, finely adjusted by the wedge pair WP2, the BOC allows attosecond-precision relative timing measurement. The low-pass filtered ($<$ 30 Hz) BOC signal feeds a loop based on a proportional–integral–derivative controller driving the PZT. The feedback locks the relative delay between the pulses; when the delay is detuned from zero by WP2, in the overlapping spectral region of the two OPAs a clear fringe pattern arises from interference. The pattern allows the detection, through the FTSI technique, of any shift between the AP of the pulses.

Figure 36a shows a set of interference patterns collected over 10 minutes. The strong fluctuations observed when the loop is open are ascribed to the jitter of the relative delay between the pulses, mainly due to the instabilities in the long optical paths of the two OPAs. When the delay is actively adjusted by the closed loop fed by the BOC signal, the interference pattern reveals that the AP is locked. This is achieved by locking the delay of the pulses: Fig. 36b shows the delay shift in the two configurations. When delay locking is active, fluctuations below 30 as rms over a measurement time of 10 minutes are observed, corresponding to less than one-eightieth of an optical cycle. Exact calibration of the relative delay as a function of the BOC voltage was deduced from interferometric measurements of Fig. 36a.

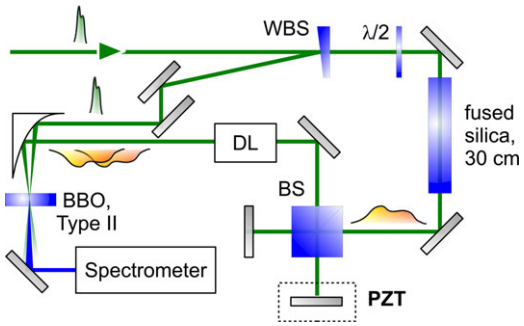

Figure 37 2DSI schematic diagram. BS: cube beam splitter; WBS: wedged beam splitter; DL: delay line. Figure from [65].

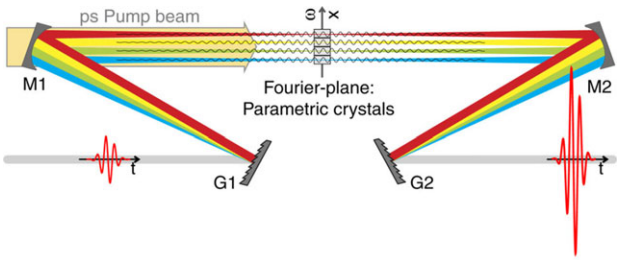

Figure 38 Scheme of the FOPA approach. G1, G2: diffraction gratings; M1, M2: spherical mirrors. Figure from [156].

Temporal characterization of the synthesized waveform is performed with the 2DSI setup [131] sketched in Fig. 37. Here the 2DSI system up-converts the pulse to be measured with two strongly chirped and time-delayed replicas of the IR portion of the spectrum. The 40 μm type-II BBO up-conversion crystal guarantees a broad acceptance bandwidth along the ordinary axis. The 2DSI measurement of the whole synthesized spectrum and the retrieved frequency-dependent group delay give the spectral phase shown in Fig. 34a: the phase is essentially flat over the whole pulse bandwidth; the residual oscillations in the visible spectral range are attributed to the large number of bounces on the CMs having imperfections in the targeted group delay design. The corresponding retrieved temporal envelope intensity profile is shown in Fig. 34b. The FWHM of the intensity profile is 3.8 fs, indicating that the pulse is compressed to within 4% of the TL duration; in addition, 70 to 80% of the pulse energy is in the main peak, and the oscillation of the electric field in the side lobes is small enough to have negligible contribution to strong-field processes, like CEP-sensitive field emission from nanotips [39]. This system combines the broadband light from two OPAs; in principle, further energy scaling and an extension of the synthesized bandwidth are possible by the coherent addition of other ultrabroadband OPAs [18, 92], which requires an additional feedback loop for the synchronization of other channels.

5.5.2. Frequency-domain OPA

One of the challenges inherent to the parallel approach for waveform synthesis is inevitably the need to lock the carrier phase (or the CEP and the delay) of the parent pulses. In the parallel scheme the two parent pulses travel along different paths, where they get amplified and suitably prepared for the coherent synthesis: the two paths typically include amplification stages and dispersion management which are tailored for broadband operation in a specific spectral region. The optical paths introduce linear and nonlinear fluctuations in the carrier phase of the pulses, which are typically considered as intrinsic challenges of the parallel approach. Recently a frequency-domain OPA (FOPA) [156] was demonstrated, which features (positive and negative) aspects of both parallel and sequential synthesis schemes: the scheme is parallel with respect to the amplification process; it is sequential with respect to dispersion management, bandwidth limitations (e.g. originating from the diffraction efficiency curve of the gratings), and the intrinsic stability of the relative timing and phase (i.e. carrier and pulse delay locking is warranted without active feedback stabilization). The approach is based on the spatially dispersed amplifier [198], which was introduced to reduce the gain narrowing effects in laser amplifiers. The original idea was to spatially disperse the seed beam in the gain medium and to amplify each component with a spatially tailored pump beam. The scheme was successfully applied to regenerative [199] and multipass [200] Ti:sapphire amplifiers, and recently to Yb:KYW systems [201]. However, the amplification bandwidth in these systems is ultimately limited by the fixed transition bands of the gain media; broadening of the bandwidth can be achieved using nonlinear crystals, where diverse phase-matching conditions allow tuning of the amplification process. Combination of the spatially dispersed design with parametric amplification leads to the FOPA scheme [156].

The system, sketched in Fig. 38, generates two-cycle pulses at 1.8 μm wavelength: it is based on a 4-f setup [202], which acts as a zero-dispersion pulse shaper. The grating stretcher maps the spectral components of the input pulse on the Fourier plane; when both gratings are placed at the focal distance from the collimating mirrors (M1 and M2) and the mirror distance is $2f$, the system is symmetric and does not alter the spectral and spatial phase of the input pulse. A set of OPA crystals are placed in the Fourier plane to selectively boost the power of specific spectral portions of the dispersed seed light. Ultrabroadband phase matching is achieved by spreading the spectrum over many individually tunable nonlinear crystals, and thus is not limited by the bandwidth acceptance of a single crystal; in this sense, the approach is very similar to the parallel scheme, since the components of the incoming pulse are spatially separated, simultaneously amplified by multiple narrowband OPAs in the Fourier plane, and coherently combined. All the pulse components travel over the common 4-f path, and hence their carrier phases are always automatically locked. On the other hand, it seems that precise dispersion compensation (e.g. using DCMs), if required, needs to be performed on the whole recombined bandwidth. All these aspects are characteristic features of the sequential synthesis approach. The system is powered

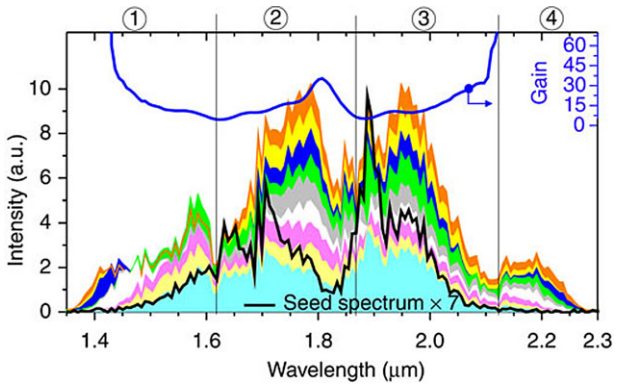

Figure 39 Amplified spectra recorded for different pump levels (colored spectra); the magnified seed spectrum is displayed as the black curve. The experimentally obtained gain curve is also indicated (blue line). Figure from [156].

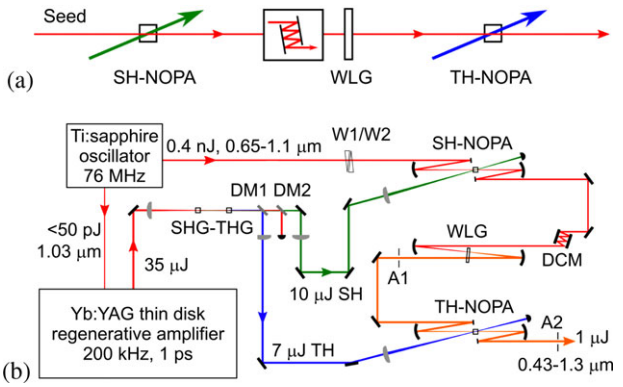

Figure 40 Sequential two-color-pumped OPA synthesizer. (a) Conceptual overview of the three main parts of the system. (b) Detailed setup of the OPCPA. W1/W2: BK7 wedges; DM1, DM2: dichroic beam splitters; DCM: double-chirped mirror pair; A1, A2: apertures. Figure from [67].

by a 25 mJ, 45 fs, 100 Hz Ti:sapphire laser. A fraction of this light pumps a white-light-seeded OPA, which delivers 50 fs, passively CEP-stabilized idler pulses at 1.8 μm wavelength. This light is then spectrally broadened in a hollow-core fiber, compressed close to the TL, and used as seed for the FOPA. Figure 39 shows the spectrum of the seed beam at the input (black line) of the FOPA, when the pump beam is blocked; comparison with the seed spectrum transmitted by the shaper reveals no significant reshaping effect of the FOPA, which exhibits a total throughput of 48% over the full bandwidth, corresponding to 75% transmission of one half of the 4-f setup. The diffraction gratings G1 and G2 have a groove density of 75 lines/mm, and the collimating mirrors M1 and M2 have a focal length of 800 mm; they give rise to a spectral spread of about 60 mm in the Fourier plane, and effective pulse duration in each focal spot in the picosecond range. For this reason, the FOPA needs to be pumped by picosecond pulses: pulses from the FF laser source are stretched to roughly 2 ps duration by a grating pair. The elongated shape of the pump in the focal plane is achieved by a combination of an aspheric Powell lens and cylindrical lenses [203], which enhances the pump intensity at the edge of the dispersed seed and equalizes the gain across the entire seed spectrum. Amplification is obtained by four identical (except for the phase-matching angle) type-I BBO crystals in the Fourier plane, indicated by circled numbers in Fig. 39. To avoid any mismatch of the optical path in the 4-f setup, all the crystals were polished in one batch to ensure their same optical thickness. When pumped by 12.8 mJ, 800 nm pulses, the system delivers 1.43 mJ amplified pulses. The amplified pulse spectrum does not show relevant dependence on pump energies ranging from 2.9 to 12.8 mJ, as shown in Fig. 39. The amplified pulse duration, measured by SHG-FROG, is around 12 fs, corresponding to less than two optical cycles at 1.8 μm. As expected, the FOPA is also able to preserve the CEP: f–$2f$ measurements reveal that the rms of the CEP evaluated averaging over 10 laser shots increases from 320 mrad after the hollow-core fiber to 460 mrad after the amplifier.

5.5.3. Sequential two-color-pumped OPA synthesizer

In addition to parallel coherent combination of ultrabroadband OPCPAs or OPAs [65,66], a compact sequential two-color-pumped OPA synthesizer supporting pulses in the single-cycle regime at high repetition rates was demonstrated by Morgner's group [67]. The system starts with a commercial Ti:sapphire oscillator (optionally CEP stabilized) which delivers both the broadband seed for the OPA stages and the narrowband seed for the Yb:YAG amplifier with a repetition rate of 200 kHz [204]. It produces pulses with 35 μJ energy and 1.5 ps duration at 1030 nm. The FF 1030 nm radiation is converted to its SH (515 nm) and subsequently to its TH (343 nm) by SFG, and provides the pump pulses for the two NOPA stages. Two DBSs separate the three beams for independent collimation; in addition, the ratio between the SH and TH output power can easily be adjusted. After a first amplification stage (SH-NOPA in Fig. 40) the spectral bandwidth is extended to the blue wavelength region by white-light generation in a bulk material. A second OPA stage amplifies the visible part while the IR is transmitted nearly unchanged in the same beam (TH-NOPA in Fig. 40). The main structures of the seed are conserved during the first NOPA stage, which delivers pulses with 1 μJ of pulse energy in broadband spectra supporting pulse durations below 7 fs. The signal of the SH-NOPA is compressed down to sub-20 fs and further focused down into a 3 mm long BaF_2 plate for white-light generation spanning from 430 to 1300 nm at the −40 dB level. The second NOPA stage amplifies the visible components of the supercontinuum seed, whereas the remaining spectrum is transmitted unaltered being out of phase matching. The final spectrum shows a prominent peak around the central frequency at 450 THz, containing 1 μJ of pulse energy at a repetition rate of 200 kHz. The dispersion compensation scheme employs 23 bounces on octave-spanning DCMs (500 to 1000 nm) and some wedges for dispersion fine control. Figure 41 shows a SPIDER measurement of this inner part of the spectrum yielding the spectral phase

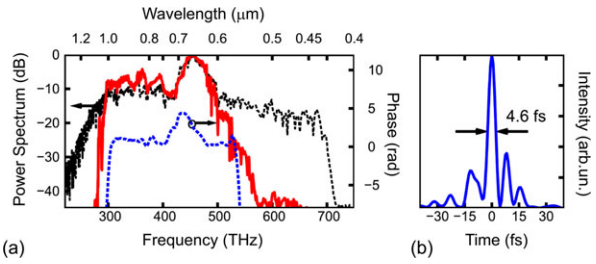

Figure 41 SPIDER measurement. (a) Inner part of the spectrum behind the dispersive mirrors (red solid curve), measured spectral phase (blue dashed curve), and the full spectral output of the two-color-pumped OPCPA (black dashed curve). (b) Temporal intensity profile with a FWHM of 4.6 fs.

and the temporal pulse envelope with a FWHM of 4.6 fs. However, to achieve the 2.5 fs TL pulse duration of the whole output spectrum, adaptive phase-control methods, e.g. a 4-f SLM pulse-shaper setup [88, 94], will have to be considered in the future.

5.5.4. Multicycle waveform synthesizers

Following the theoretical prediction of the so-called *perfect waveform for HHG* [25], many pioneering studies have been reported, e.g. combination of a fundamental with an optical harmonic [205–207], or an incommensurate two-color field synthesis based on OPA to generate intense isolated attosecond XUV pulses for XUV-pump/XUV-probe spectroscopy [20, 21]. These experiments have shown that optimized waveform synthesis will markedly enhance HHG in terms of increased cutoff energy and higher conversion efficiency [25, 26]. Nevertheless, to realize such optimized waveforms, a *stably phase-locked* multi-color synthesizer is much desired. Recently, a step towards this goal was made by Haessler *et al.* [27] based on the dual CEP-locked multi-color parametric synthesizer schematically shown in Fig. 42. In this system, the pump (1030 nm), signal (1545 nm), and idler (3090 nm) pulses of a type-II KTP OPA plus the second harmonic of the pump (515 nm) can be used for multi-color field superpositions. To realize reproducible phase-stable superpositions of all these colors, a combination of active CEP locking of the diode-pumped Yb:KGW MOPA pump [208] with passive CEP stabilization of the 3090 nm idler pulses is required [116].

In a first proof-of-principle three-color experiment, HHG driven by a three-color superposition (515 nm + 1030 nm + 1545 nm) demonstrated an increase in XUV flux by two orders of magnitude, similar to that seen for two-color fields [209], together with indications for an extension of the HHG cutoff (compared to HHG driven by single-color 1030 nm or 1545 nm pulses).

The waveform synthesizer (Fig. 42) is pumped by an actively CEP-stabilized Yb:KGW MOPA [208], which delivers 1 kHz, 6 mJ, 180 fs output pulses at the central wavelength of 1030 nm. An rms CEP jitter of ≈ 950 mrad of the 1030 nm pump pulses was achieved in [27]. The passive stability of the interferometer used for implementing the superposition (resulting in an upper bound for the rms phase jitter of 170 as between the 1545 nm and 1030 nm pulses) could in principle be reduced by implementing active feedback stabilization in the future.

The group velocity delay between the pump pulses and the SH is compensated by inserting a calcite plate; the fine tuning of the phase delay between the fundamental 1030 nm pulse and its 515 nm SH pulse is done by rotating a thin fused silica plate. The white-light seed for the OPA is generated in a sapphire plate. The OPA consists of three stages with type-II phase matching in KTP crystals and is tuned to amplify a signal pulse at 1545 nm. An interference filter after the first OPA stage narrows the bandwidth around 1545 nm, so that the final amplified signal pulse is nearly as long (170 fs) as the pump pulses and, most importantly, is close to the Fourier limit. The signal wave is separated from the OPA output and then combined with the fundamental and its SH via dichroic mirrors. The phase delay of the 1545 nm signal pulse relative to the 1030 nm fundamental pulse is scanned by varying the CEP locking point of the pump laser amplifier slow loop. The three spatially and temporally superposed pulses are then focused into a static gas cell for XUV generation. Finally, 0.5 mJ waveforms were synthesized. This Fourier synthesis recurs with a 10.3 fs period under the envelope of the 180 fs laser pulse. Haessler *et al.* used this three-color synthesizer to investigate HHG cutoff extension and efficiency enhancement. In the near future, a high-energy sub-cycle parametric waveform synthesizer [18] will become a versatile tool for the most important challenges in attosecond science.

5.6. Energy scaling

Waveform synthesizers of high energy have the potential to revolutionize attosecond science, strong-field physics, and the study of relativistic laser–plasma interactions because they provide the capability of coherently manipulating high-energy electron trajectories. For example, the HHG yield can be markedly enhanced and isolated attosecond pulse generation is possible with properly sculpted waveforms [20,21,26]. The energy scaling of pulse synthesizers beyond the multi-millijoule level can open up many new applications in strong-field laser science. The ultimate energy obtainable from a multichannel synthesizer is determined by how much energy each individual channel contains before they are coherently combined. Most pulse synthesis techniques rely on laser sources at high repetition rates, in the kHz–MHz range, because of the feedback loop required for timing and/or CEP stabilization. Therefore, a high repetition rate is beneficial for pulse synthesizers when energy scaling is considered. However, handling a high average power resulting from the increased energy at a high repetition rate is very demanding in terms of pump laser development. In fact, it is possible to decrease the repetition rate to an approximately 10 Hz level to achieve a high energy in the amplifier stages seeded by kHz–MHz

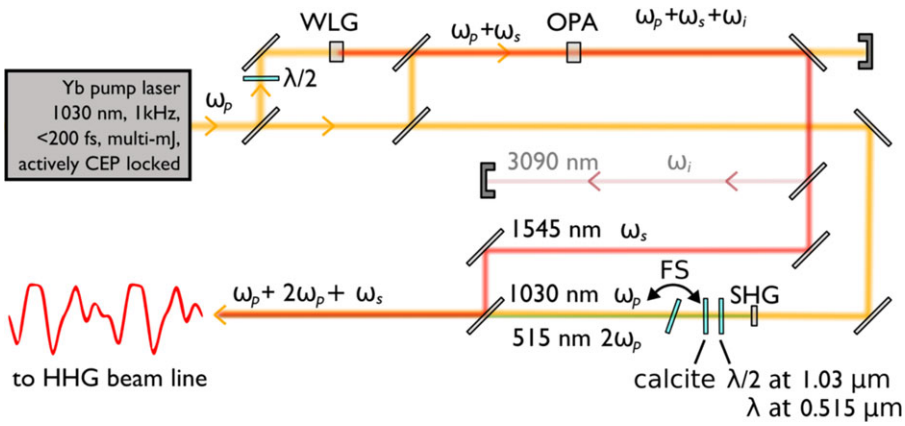

Figure 42 Layout of the dual CEP-locked multi-color parametric waveform synthesizer. A CEP-stabilized, multi-millijoule, diode-pumped femtosecond Yb:KGW pump laser and a collinear white-light-seeded type-II KTP OPA are followed by a multi-color interferometer relying solely on passive stability and a SHG crystal in the 1 μm arm. WLG: white-light generation; FS: fused silica. Figure from [27].

ultrabroadband pulses if feedback control is not necessary as in the sequential waveform synthesis scheme [32]. In this section, we describe a multi-millijoule kilohertz waveform synthesizer and then briefly discuss a high-energy 10 Hz synthesizer recently demonstrated [32].

Among the waveform synthesis techniques discussed in this review, the OPCPA-based method has the highest potential for energy scaling. For example, the passive waveform synthesis based on post-compression techniques with spectral broadening in gas-filled hollow-core fibers or highly nonlinear fibers (see Section 5.3) is inherently unsuitable for energy scaling beyond the few-millijoule level. On the other hand, most OPA-based systems rely on well-established femtosecond Ti:sapphire amplifier technology whose pump energy is limited to the approximately 20 mJ level at kilohertz repetition rates and cannot be further increased because of the thermo-optic properties of Ti:sapphire amplifier crystals. Besides the pump laser limitation, the OPA technique cannot handle too much energy due to the short pump pulse duration in the femtosecond range unless the beam size is significantly enlarged. Compared to the other techniques, OPCPA can easily handle energies much higher than multi-millijoule, provided that high-energy narrowband picosecond or sub-picosecond pump lasers are available. However, this also means that energy scaling of OPCPA-based waveform synthesizers is a nontrivial task without a suitable high-power pump laser source. Early works on kilohertz few-cycle mid-IR OPCPA systems [185, 186] and the OPCPA-based waveform synthesizer in Section 5.4 [66] relied on picosecond Nd:YLF lasers providing a pump energy of 5–11 mJ at 1 kHz repetition rate. Recently, new high-power pump laser technologies based on Yb:YAG gain media at 1.03 μm have been explored. In 2009, Metzger *et al.* [210] reported a 25 mJ, $\approx$ 1 ps thin-disk Yb:YAG amplifier at 3 kHz, which recently enabled the generation of 1.2 mJ, 2.1 μm OPCPA pulses [211]. Most recently, amplification of 1.03 μm pulses to more than 40 mJ of energy from thin-disk amplifiers [212,213] has been reported. High-power lasers can be also obtained using the Innoslab design, initially established for neodymium-doped laser crystals, and now applied to ytterbium-doped gain materials. An Innoslab amplifier delivering 1.9 mJ, 1.03 μm, 800 fs pulses at 188 kHz repetition rate [214] has recently been applied to drive a two-stage NOPA centered at 800 nm, and to generate 180 μJ, 15 fs pulses at a wavelength of 800 nm [215]. In 2010, Hong *et al.* [216] demonstrated the amplification of uncompressed picosecond pulses to 40 mJ at 2 kHz from a two-stage cryogenic Yb:YAG CPA laser. A modified cryogenic Yb:YAG laser with 15 mJ of compressed output energy was used for pumping a sub-millijoule, 2.1 μm OPCPA system at 1 kHz repetition rate [217]. In more recent work, Hong *et al.* [218] further upgraded this pump laser by adding a single-pass amplifier stage and reconfiguring the amplifier chain and obtained an amplified pulse energy of 56 mJ and compressed pulse energy of 42 mJ at 1 kHz repetition rate. In this section, we review this pump laser system and discuss a multi-millijoule pulse synthesizer currently under development including the multi-millijoule OPCPA result at 2.1 μm.

The system layout of the 42-mJ 1-kHz cryogenic Yb:YAG pump laser system is illustrated in Fig. 43a. The seed from a Ti:sapphire oscillator, which also provides the seed signal for the OPCPA stages, is pre-amplified in Yb-doped fiber amplifiers, stretched by a chirped volume Bragg grating pair to $\approx$ 560 ps with 0.7 nm of bandwidth at 1029 nm, and then amplified by a 1-kHz 6 mJ regenerative amplifier and two multipass amplifiers that are all based on cryogenically cooled Yb:YAG as gain medium. The first two-pass amplifier employs a 1% doped 10 mm long Yb:YAG crystal, whereas the second single-pass amplifier uses 2% doped 20 mm long crystals. Each crystal has 2 mm of an undoped YAG end cap on the pumping side. The crystals are indium-bonded to a heat sink and cooled to 77 K by liquid nitrogen in a vacuum chamber connected to an auto-refilling system. The beam size and the divergence at each stage have been carefully matched to the pump beams using telescopes. The periscope after the two-pass amplifier helps compensate the thermally induced astigmatism induced by both amplifiers. The maximum energy from the second and third amplifiers is 30 and 56 mJ, respectively, with excellent beam profiles, as shown in Fig. 43b and c. The pump powers from two fiber-coupled continuous wave $\approx$ 940 nm laser diodes at the maximum output energy are both 240 W, while the absorption is $\approx$ 75% at Crystal 1 and $\approx$ 95% at Crystal 2. The amplified pulse with a

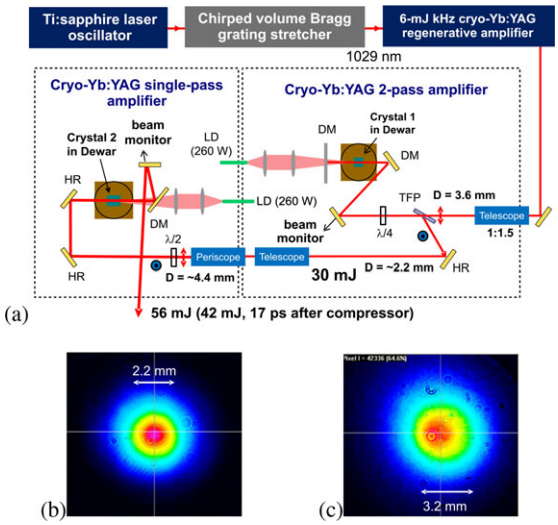

Figure 43 (a) Optical layout of the three-stage 1-kHz picosecond cryogenic Yb:YAG CPA laser and the beam profiles from (b) the two-pass and (c) the single-pass amplifiers [218]. The circular fringes in the beam profiles are a measurement artifact from neutral density filters. Crystal 1: 1% doped, 10 mm long Yb:YAG; Crystal 2: 2% doped, 20 mm long Yb:YAG; D: diameter; HR: high reflector; DM: dichroic mirror; TFP: thin-film polarizer; $\lambda/2$: half waveplate; $\lambda/4$: quarter waveplate; LD: laser diode at 940 nm.

spectral bandwidth of 0.2 nm is compressed to 17 ps using a multilayer dielectric grating pair with a throughput of 75%, delivering a compressed energy of 42 mJ. It should be noted that the pulse duration before the compression is $\approx$ 150 ps which is shortened from $\approx$ 560 ps due to the gain narrowing in the regenerative amplifier. Currently, the amplified pulse energy of 56 mJ is limited by the combined effect of B-integral and thermal lensing. Simulations [219] show that 100 mJ of energy could be obtained if the stretched pulse were stretched to about twice the length of $\approx$ 300 ps by fiber Bragg gratings.

The improved pump laser can be used for upscaling the energy of the waveform synthesizer described in Section 5.4 [66, 184] based on 2.1 μm and 870 nm OPCPA systems whose optical layout is illustrated in Fig. 44.

As reported for the energy scaling of the 2.1 μm OPCPA [217,220], the OPCPA systems are pumped by two picosecond lasers: (i) a 1047 nm 11 ps Nd:YLF amplifier and (ii) a 1029 nm 17 ps cryogenic Yb:YAG amplifier. Both pump lasers are seeded by the same CEP-stable octave-spanning Ti:sapphire laser for achieving optical synchronization. The Nd:YLF CPA laser pumps the first two OPCPA stages in both 2.1 μm and 870 nm channels (each OPA 1, 2 in Fig. 44) with a total pump energy of 3.5 mJ [184]. The 42 mJ cryogenic Yb:YAG laser pumps the final OPCPA stages of both channels for power amplification. Even though the energy from the Nd:YLF laser is only $\approx$ 10% of that from the cryogenic Yb:YAG pump laser, we maintain this pump laser because the first two stages of both channels were carefully optimized with Nd:YLF laser pulses. However, eventually the OPCPA systems can be operated without the Nd:YLF pump laser. For the energy scaling of individual channels, we first used the maximum pump energy of 42 mJ to pump the final stage of the 2.1 μm OPCPA and obtained a record-high energy of 2.6 mJ at 1 kHz repetition rate [218]. The compressed pulses successfully generated high-flux soft-X-ray HHG pulses from Ar with a cutoff energy extended to 190 eV [218]. In this experiment, the TL pulse duration of the amplified spectrum is 29 fs or four optical cycles at 2.1 μm because of the reduced phase-matching bandwidth in the thick BBO crystal. We expect to recover the pulse duration as short as three optical cycles that is suitable for sub-single-cycle pulse synthesis, using a large-aperture MgO-doped periodically poled lithium tantalate crystal or a bulk $LiNbO_3$ crystal [211]. The pump energy has to be split into two channels for operating the waveform synthesizer. Considering a typical conversion efficiency of $\approx$ 7% from the pump laser to the 2.1 μm output, 18 mJ of pump energy can produce $\approx$ 1.3 mJ of output energy at 2.1 μm for the waveform synthesis. The rest of the pump energy (24 mJ) can be directed to the 870 nm OPCPA channel. Recently we frequency-doubled 30 mJ picosecond pulses from this laser and generated more than 15 mJ of green (515 nm) picosecond pulses in a noncritically phase-matched LBO crystal. We expect to generate $\approx$ 1.3 mJ pulses from the 870 nm OPCPA stage if we use 12 mJ (SHG of 24 mJ) of pump energy at 515 nm. Our broadband dichroic beam combiner has a combined efficiency of $\approx$ 80% for two channels, making it feasible to generate $\approx$ 2 mJ of synthesized waveforms. For long-term stable operation of each OPCPA channel as well as the waveform synthesizer with low energy fluctuations, it is of critical importance that the pump laser has low shot-to-shot energy and pointing fluctuations. There are still many engineering issues regarding pump lasers, OPCPA stages, and timing stabilization using BOC that have to be solved. The cryogenic Yb:YAG regenerative amplifier provides an excellent shot-to-shot energy stability as low as 0.3% rms; after the beam goes through two multipass Yb:YAG amplifiers and the grating compressor, the relative energy fluctuations increase to $\approx$ 1.5% rms due to air fluctuations along the beam path. The resulting shot-to-shot stability of the amplified multi-millijoule 2.1 μm pulses is currently $\approx$5% rms. The shot-to-shot energy stability and the beam pointing stability of the pump pulses are directly coupled with the energy stability of OPCPA output pulses. Active beam pointing stabilizers are used for both pump lasers and the beam path is shortened to minimize the influence of air fluctuations. A compact design and environmental protection through packaging will further improve system stability while energy scaling is continued.

At moderate average power, energy scaling of an OPCPA-based sequential waveform synthesizer is possible when low-repetition-rate high-energy picosecond pump lasers are used. Veisz *et al.* [32] generated 80 mJ, 5 fs pulses in the visible-to-NIR range at 10 Hz repetition rate using a sequential two-color-pumped OPCPA technique [190] described in Fig. 40. In that work, a commercial picosecond Nd:YAG laser operating at 10 Hz pumps four OPCPA stages seeded by a 1-kHz continuum generated from a

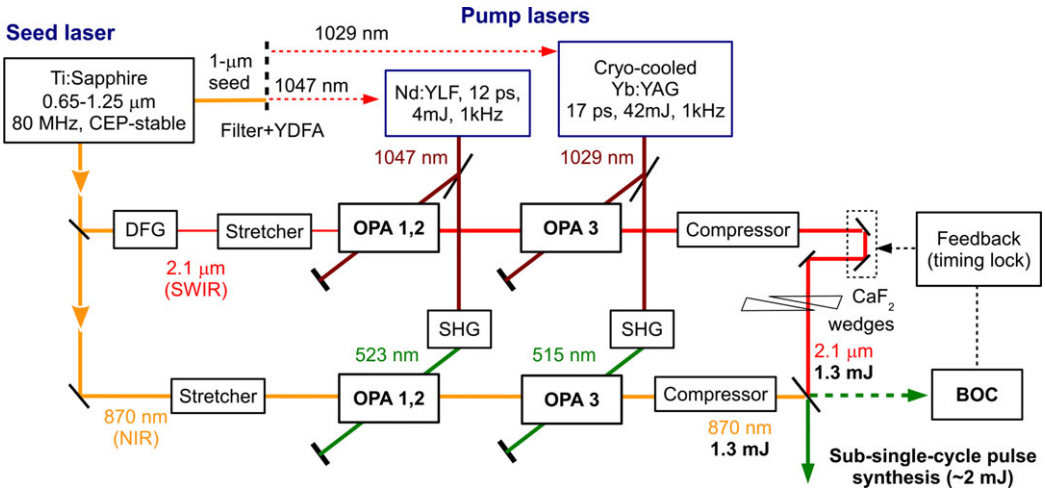

Figure 44 Schematic diagram of the multi-millijoule OPCPA-based waveform synthesizer pumped by a cryogenic picosecond Yb:YAG laser.

conventional Ti:sapphire amplifier-pumped hollow-core fiber system. Since all the spectral components share a common beam path along multiple OPCPA stages, timing and relative phase lock is not necessary, as confirmed by successful pulse compression.

6. Conclusions and future perspectives

In this paper we have reviewed the new technology and challenges in realizing sub-cycle waveform synthesizers, which have not been available at optical frequencies so far. Such systems overcome the traditional bandwidth limitations of ultrafast amplifiers, such as CPAs, OPAs and OPCPAs. In addition, OPA- and OPCPA-based synthesizers will in the future overcome energy and average power bottlenecks. Currently, because of the greater availability of Ti:sapphire pump laser technology for OPAs, synthesizers employing Ti:sapphire pump lasers are closer to operation [18,221–223], but in the future these synthesis schemes can be directly transferred to Yb-doped pump laser technology, especially with cryogenically cooled, Innoslab, or thin-disk lasers [216,218,224,225]. High-energy single-cycle pulses can be used for the direct generation of energetic isolated attosecond pulses for attosecond XUV-pump/XUV-probe spectroscopy [20, 21], for HHG cutoff extension, and efficiency enhancement by sub-cycle electric waveform sculpting [25–27]. Moreover, sub-cycle waveforms open up new horizons in strong-field recollision physics including laser-induced electron diffraction and holography [226–228]. Due to the extremely short pulse durations, relativistic intensities can be reached at relatively modest energies of the order of millijoules, allowing average-power scaling of terawatt lasers, which is extremely useful for direct electric field acceleration of electrons [229]. Low-energy high-repetition-rate synthesizers have intriguing applications for controlling ballistic electron transport in solids and concomitant emission of higher harmonics [42, 44, 45], or in combination with tip-enhanced nanoscale electron sources may lead to the construction of high-repetition-rate single-electron sources with sub-femtosecond duration and few-nanometer spatial confinement. This can be applied to electron diffraction and to electron microscopy [230].

List of abbreviations

2DSI	two-dimensional spectral shearing interferometry
AMP	amplitude module
AOFS	acousto-optic frequency shifter
AOM	acousto-optic modulator
AOPDF	acousto-optic programmable dispersive filter
AP	absolute phase
BBBS	broadband beam splitter
BBO	β-barium borate
BOC	balanced optical cross-correlation
CEO	carrier–envelope offset
CEP	carrier–envelope phase
CM	chirped mirror
CPA	chirped-pulse amplifier
DBS	dichroic beam splitter
DCM	double-chirped mirror
DF	difference frequency
DFG	difference-frequency generation
DM	deformable mirror
DOPA	degenerate optical parametric amplifier
EDFA	erbium-doped fiber amplifier
EOTS	electro-optic timing shifter
FF	fundamental frequency

FOPA	frequency-domain optical parametric amplifier
FROG	frequency-resolved optical gating
FROG-CRAB	frequency-resolved optical gating for complete reconstruction of attosecond bursts
FTSI	Fourier transform spectral interferometry
FWHM	full width at half maximum
FWM	four-wave mixing
GDD	group-delay dispersion
HHG	high-harmonic generation
HNLF	highly nonlinear fiber
HS	harmonic separator
IAP	isolated attosecond pulse
IPM	induced-phase modulation
KLM	Kerr-lens mode-locked
LBO	lithium triborate
LC-SLM	liquid-crystal spatial light modulator
NEP	noise equivalent power
NIR	near-infrared
NOPA	non-collinear optical parametric amplifier
OAWG	optical arbitrary waveform generation
OPA	optical parametric amplifier
OPCPA	optical parametric chirped-pulse amplifier
PLL	phase-lock loop
PM	phase module
PPKTP	periodically poled potassium titanyl phosphate
PROOF	phase retrieval algorithm by omega oscillation filtering
PZT	piezoelectric actuator
SEA	spatially encoded arrangement
SF	sum frequency
SFG	sum-frequency generation
SHG	second-harmonic generation
SPIDER	spectral phase interferometry for direct electric field reconstruction
SPM	self-phase modulation
SWIR	short-wavelength infrared
TH	third harmonic
TL	transform-limited
TOD	third-order dispersion
TOF	time-of-flight
TS	time-swap module
VCO	voltage-controlled oscillator
WLC	white-light continuum
XUV	extreme ultraviolet

Acknowledgements. This work was supported by the Air Force Office of Scientific Research under grants FA8655-09-1-3101, FA9550-12-1-0080, FA9550-13-1-0159, FA9550-14-1-0255 and FA9550-12-1-0499, Progetto Rocca, the Center for Free-Electron Laser Science at DESY, the excellence cluster "The Hamburg Centre for Ultrafast Imaging- Structure, Dynamics and Control of Matter at the Atomic Scale" of the Deutsche Forschungsgemeinschaft and by JRA-INREX from LASERLAB-EUROPE (grant agreement no. 284464, ECS Seventh Framework Programme). GCe acknowledges support by the European Research Council Advanced Grant STRATUS (ERC-2011-AdG no. 291198). CM acknowledges support by MIUR FIRB grant no. RBFR12SW0J. SF acknowledges support by the National Key Basic Research Program of China (No. 2013CB922401).

Received: 1 August 2014, **Revised:** 8 October 2014, **Accepted:** 16 October 2014

Published online: 30 December 2014

Key words: Ultrabroadband sources, pulse synthesis, parametric oscillators and amplifiers, frequency conversion, ultrafast nonlinear optics, ultrafast measurements, phase measurement.

Cristian Manzoni received a PhD in physics at Politecnico di Milano, Italy, where he studied passive CEP stabilization, generation of broadband IR pulses, and time-resolved spectroscopy of nanostructures. Since 2010 he has been a researcher at the Institute for Photonics and Nanotechnology of the National Research Council of Italy.

Oliver D. Mücke received a diploma (1999) and PhD degree (2003) in physics from Universität Karlsruhe (TH), Germany. He was a postdoc at the Massachusetts Institute of Technology Research Laboratory of Electronics (2003–2007) and Photonics Institute at TU Vienna, Austria (2007–2011). Since 2011 he has been a Senior Scientist at DESY CFEL. His research interests include CEP-stable few-cycle pulse generation and sub-cycle waveform synthesis, frequency-comb technology for optical clocks, strong-field physics and attoscience, and extreme nonlinear optics in solids.

Giovanni Cirmi received a PhD in physics in 2008 from Politecnico di Milano, Italy. He was postdoctoral fellow and associate at Massachusetts Institute of Technology, USA. He is currently a research scientist at DESY CFEL, Germany. His main research interests are extreme nonlinear optics and applications to spectroscopy in the femtosecond and attosecond time scales.

Shaobo Fang received bachelor and doctoral degrees from Tianjin University, China and Hokkaido University, Japan, respectively. Since 2011 he has been a research scientist in the framework of the Helmholtz Association Young Scientist Program at DESY CFEL. His research interests include sub-cycle waveform synthesis and novel monocycle pulse generation for attosecond science. He is a member of the Optical Society of America.

Jeffrey Moses is an assistant professor in the School of Applied and Engineering Physics at Cornell University, with interests in ultrafast nonlinear optical technologies, dynamics, and spectroscopy. As a research scientist at Massachusetts Institute of Technology from 2009 to 2014, he worked on ultrafast sources and strong-field physics, and was named an AFOSR Young Investigator in 2013.

Shu-Wei Huang is a research scientist at Columbia University, with research interests in ultrafast optical technologies, ultrafast nanophotonics, terahertz technologies, coherent imaging technologies, and nonlinear spectroscopy. He received a BS degree from National Taiwan University (2005) and a PhD degree from Massachusetts Institute of Technology (2012), both in electrical engineering.

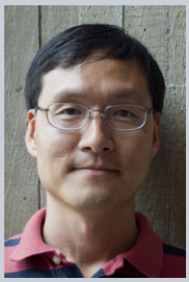

Kyung-Han Hong is a Principal Research Scientist and Principal Investigator at the Massachusetts Institute of Technology Research Laboratory of Electronics. He was educated at KAIST, South Korea, where he completed BA (1996), MS (1998), and PhD (2003) degrees, all in physics. His recent research interests include high-power ultrafast lasers, mid-IR OPCPAs, soft X-ray HHG and spectroscopy, attosecond pulse generation, and terahertz-pulse-driven electron acceleration.

Giulio Cerullo is Full Professor at the Physics Department, Politecnico di Milano, Italy. His research focuses on the broad area known as ultrafast optical science, and concerns the generation of few-optical-cycle tunable light pulses and their use to capture the dynamics of ultrafast events in molecular and solid-state systems.

Franz X. Kärtner heads the Ultrafast Optics and X-rays Division at the Center for Free-Electron Laser Science (CFEL) at DESY, Hamburg, and is Professor of Physics at University of Hamburg, and Adjunct Professor of Electrical Engineering at Massachusetts Institute of Technology. His research interests include noise in electronic and optical sources, ultrashort pulse lasers, high-energy sub-cycle waveform synthesis and its use in precision timing in advanced accelerators and light sources, attosecond physics, and free-electron lasers.

References

[1] L. E. Hargrove, R. L. Fork, and M. A. Pollack, Appl. Phys. Lett. **5**(1), 4–5 (1964).
[2] E. P. Ippen, C. V. Shank, and A. Dienes, App. Phys. Lett. **21**(8), 348–350 (1972).
[3] R. L. Fork, C. H. Brito Cruz, P. C. Becker, and C. V. Shank, Opt. Lett. **12**(7), 483–485 (1987).
[4] I. D. Jung, F. X. Kärtner, N. Matuschek, D. H. Sutter, F. Morier-Genoud, G. Zhang, U. Keller, V. Scheuer, M. Tilsch, and T. Tschudi, Opt. Lett. **22**(13), 1009–1011 (1997).
[5] R. Ell, U. Morgner, F. X. Kärtner, J. G. Fujimoto, E. P. Ippen, V. Scheuer, G. Angelow, T. Tschudi, M. J. Lederer, A. Boiko, and B. Luther-Davies, Opt. Lett. **26**(6), 373–375 (2001).
[6] M. Nisoli, S. De Silvestri, and O. Svelto, App. Phys. Lett. **68**(20), 2793 (1996).
[7] M. Nisoli, S. De Silvestri, O. Svelto, R. Szipöcs, K. Ferencz, C. Spielmann, S. Sartania, and F. Krausz, Opt. Lett. **22**(8), 522–524 (1997).
[8] A. Baltuška, Z. Wei, M. S. Pshenichnikov, and D. A. Wiersma, Opt. Lett. **22**(2), 102–104 (1997).
[9] O. D. Mücke, S. Ališauskas, A. J. Verhoef, A. Pugžlys, A. Baltuška, V. Smilgevičius, J. Pocius, L. Giniūnas, R. Danielius, and N. Forget, Opt. Lett. **34**(16), 2498–2500 (2009).
[10] C. P. Hauri, W. Kornelis, F. W. Helbing, A. Heinrich, A. Couairon, A. Mysyrowicz, J. Biegert, and U. Keller, Appl. Phys. B **79**(6), 673–677 (2004).
[11] C. P. Hauri, A. Guandalini, P. Eckle, W. Kornelis, J. Biegert, and U. Keller, Opt. Express **13**(19), 7541–7547 (2005).
[12] G. Stibenz, N. Zhavoronkov, and G. Steinmeyer, Opt. Lett. **31**(2), 274–276 (2006).
[13] A. Baltuška, T. Fuji, and T. Kobayashi, Opt. Lett. **27**(5), 306–308 (2002).
[14] D. Brida, C. Manzoni, G. Cirmi, M. Marangoni, S. Bonora, P. Villoresi, S. De Silvestri, and G. Cerullo, J. Optics **12**(1), 013001 (2010).
[15] T. Brabec and F. Krausz, Rev. Mod. Phys. **72**, 545–591 (2000).
[16] D. J. Jones, S. A. Diddams, J. K. Ranka, A. Stentz, R. S. Windeler, J. L. Hall, and S. T. Cundiff, Science **288**(5466), 635–639 (2000).

[17] A. Apolonski, A. Poppe, G. Tempea, Ch Spielmann, Th Udem, R. Holzwarth, T. W. Hänsch, and F. Krausz, Phys. Rev. Lett. **85**, 740–743 (2000).
[18] G. M. Rossi, G. Cirmi, S. Fang, S.-H. Chia, O. D. Mücke, F. Kärtner, C. Manzoni, P. Farinello, and G. Cerullo, Spectro-temporal characterization of all channels in a sub-optical-cycle parametric waveform synthesizer, in: CLEO: 2014, (Optical Society of America, 2014), p. SF1E.3.
[19] F. Krausz and M. Ivanov, Rev. Mod. Phys. **81**, 163–234 (2009).
[20] E. J. Takahashi, P. Lan, O. D. Mücke, Y. Nabekawa, and K. Midorikawa, Phys. Rev. Lett. **104**, 233901 (2010).
[21] E. J. Takahashi, P. Lan, O. D. Mücke, Y. Nabekawa, and K. Midorikawa, Nature Commun. **4**, 2691 (2013).
[22] M. Y. Kuchiev, JETP Lett. **45**(7), 404–406 (1987).
[23] P. B. Corkum, Phys. Rev. Lett. **71**, 1994–1997 (1993).
[24] K. J. Schafer, B. Yang, L. F. DiMauro, and K. C. Kulander, Phys. Rev. Lett. **70**, 1599–1602 (1993).
[25] L. E. Chipperfield, J. S. Robinson, J. W. G. Tisch, and J. P. Marangos, Phys. Rev. Lett. **102**, 063003 (2009).
[26] C. Jin, G. Wang, H. Wei, A.-T. Le, and C. D. Lin, Nature Commun. **5**, 4033 (2014).
[27] S. Haessler, T. Balčiunas, G. Fan, G. Andriukaitis, A. Pugžlys, A. Baltuška, T. Witting, R. Squibb, A. Zaïr, J. W. G. Tisch, J. P. Marangos, and L. E. Chipperfield, Phys. Rev. X **4**, 021028 (2014).
[28] A. Baltuška, T. Udem, M. Uiberacker, M. Hentschel, E. Goulielmakis, C. Gohle, R. Holzwarth, V. S. Yakovlev, A. Scrinzi, T. W. Hänsch, and F. Krausz, Nature **421**(6923), 611–615 (2003).
[29] E. Goulielmakis, M. Uiberacker, R. Kienberger, A. Baltuska, V. Yakovlev, A. Scrinzi, T. Westerwalbesloh, U. Kleineberg, U. Heinzmann, M. Drescher, and F. Krausz, Science **305**(5688), 1267–1269 (2004).
[30] M. Hofstetter, M. Schultze, M. Fieß, B. Dennhardt, A. Guggenmos, J. Gagnon, V. S. Yakovlev, E. Goulielmakis, R. Kienberger, E. M. Gullikson, F. Krausz, and U. Kleineberg, Opt. Express **19**(3), 1767–1776 (2011).
[31] G. Sansone, L. Poletto, and M. Nisoli, Nature Photon. **5**(11), 655–663 (2011).
[32] L. Veisz, D. Rivas, G. Marcus, X. Gu, D. Cardenas, J. Mikhailova, A. Buck, T. Wittmann, C. M. S. Sears, S.-W. Chou, J. Xu, G. Ma, D. Herrmann, O. Razskazovskaya, V. Pervak, and F. Krausz, Generation and applications of sub-5-fs multi-10-TW light pulses, in: 2013 Pacific Rim Conference on Lasers and Electro-Optics, (Optical Society of America, 2013), p. TuD2_3.
[33] S. P. D. Mangles, C. D. Murphy, Z. Najmudin, A. G. R. Thomas, J. L. Collier, A. E. Dangor, E. J. Divall, P. S. Foster, J. G. Gallacher, C. J. Hooker, D. A. Jaroszynski, A. J. Langley, W. B. Mori, P. A. Norreys, F. S. Tsung, R. Viskup, B. R. Walton, and K. Krushelnick, Nature **431**(7008), 535–538 (2004).
[34] C. G. R. Geddes, C. Toth, J. van Tilborg, E. Esarey, C. B. Schroeder, D. Bruhwiler, C. Nieter, J. Cary, and W. P. Leemans, Nature **431**(7008), 538–541 (2004).
[35] J. Faure, Y. Glinec, A. Pukhov, S. Kiselev, S. Gordienko, E. Lefebvre, J.-P. Rousseau, F. Burgy, and V. Malka, Nature **431**(7008), 541–544 (2004).
[36] L. J. Wong and F. X. Kärtner, Opt. Express **18**(24), 25035–25051 (2010).
[37] V. Marceau, C. Varin, T. Brabec, and M. Piché, Phys. Rev. Lett. **111**, 224801 (2013).
[38] S. Payeur, S. Fourmaux, B. E. Schmidt, J. P. MacLean, C. Tchervenkov, F. Légaré, M. Piché, and J. C. Kieffer, Appl. Phys. Lett. **101**(4), 041105 (2012).
[39] M. Krüger, M. Schenk, and P. Hommelhoff, Nature **475**(7354), 78–81 (2011).
[40] G. Herink, D. R. Solli, M. Gulde, and C. Ropers, Nature **483**(7388), 190–193 (2012).
[41] B. Piglosiewicz, S. Schmidt, D. J. Park, J. Vogelsang, P. Groß, C. Manzoni, P. Farinello, G. Cerullo, and C. Lienau, Nature Photon. **8**(1), 37–42 (2014).
[42] O. D. Mücke, Phys. Rev. B **84**, 081202 (2011).
[43] O. D. Mücke, T. Tritschler, and M. Wegener, Resonant nonperturbative extreme nonlinear optics with two-cycle pulses: carrier-wave Rabi flopping and role of the carrier-envelope offset phase, in: Few-Cycle Laser Pulse Generation and Its Applications, edited by F. X. Kärtner, Topics in Applied Physics Vol. 95 (Springer, Berlin, 2004), 379–410.
[44] A. Schiffrin, T. Paasch-Colberg, N. Karpowicz, V. Apalkov, D. Gerster, S. Mühlbrandt, M. Korbman, J. Reichert, M. Schultze, S. Holzner, J. V. Barth, R. Kienberger, R. Ernstorfer, V. S. Yakovlev, M. I. Stockman, and F. Krausz, Nature **493**(7430), 70–74 (2013).
[45] M. Schultze, E. M. Bothschafter, A. Sommer, S. Holzner, W. Schweinberger, M. Fiess, M. Hofstetter, R. Kienberger, V. Apalkov, V. S. Yakovlev, M. I. Stockman, and F. Krausz, Nature **493**(7430), 75–78 (2013).
[46] M. F. Kling, C. Siedschlag, A. J. Verhoef, J. I. Khan, M. Schultze, T. Uphues, Y. Ni, M. Uiberacker, M. Drescher, F. Krausz, and M. J. J. Vrakking, Science **312**(5771), 246–248 (2006).
[47] F. Remacle, M. Nest, and R. D. Levine, Phys. Rev. Lett. **99**, 183902 (2007).
[48] A. Wirth, M. T. Hassan, I. Grguraš, J. Gagnon, A. Moulet, T. T. Luu, S. Pabst, R. Santra, Z. A. Alahmed, A. M. Azzeer, V. S. Yakovlev, V. Pervak, F. Krausz, and E. Goulielmakis, Science **334**(6053), 195–200 (2011).
[49] A. J. DeMaria, W. H. Glenn, M. J. Brienza, and M. E. Mack, Proc. IEEE **57**(1), 2–25 (1969).
[50] T. W. Hänsch, Opt. Commun. **80**(1), 71–75 (1990).
[51] S. E. Harris and A. V. Sokolov, Phys. Rev. Lett. **81**, 2894–2897 (1998).
[52] A. V. Sokolov, D. R. Walker, D. D. Yavuz, G. Y. Yin, and S. E. Harris, Phys. Rev. Lett. **85**, 562–565 (2000).
[53] W. J. Chen, Z. M. Hsieh, S.-W. Huang, H. Y. Su, C.-J. Lai, T. T. Tang, C. H. Lin, C. K. Lee, R. P. Pan, C. L. Pan, and A. H. Kung, Phys. Rev. Lett. **100**, 163906 (2008).
[54] Z. M. Hsieh, C.-J. Lai, H. S. Chan, S. Y. Wu, C. K. Lee, W. J. Chen, C. L. Pan, F. G. Yee, and A. H. Kung, Phys. Rev. Lett. **102**, 213902 (2009).
[55] H. S. Chan, Z. M. Hsieh, W. H. Liang, A. H. Kung, C. K. Lee, C.-J. Lai, R. P. Pan, and L. H. Peng, Science **331**(6021), 1165–1168 (2011).
[56] H. S. Chan, Z. M. Hsieh, L. H. Peng, and A. Kung, Opt. Lett. **37**(14), 2805–2807 (2012).

[57] N. K. Fontaine, R. P. Scott, L. Zhou, F. M. Soares, J. P. Heritage, and S. J. B. Yoo, Nature Photon. **4**(4), 248–254 (2010).
[58] S. T. Cundiff and A. M. Weiner, Nature Photon. **4**(11), 760–766 (2010).
[59] F. Ferdous, H. Miao, D. E. Leaird, K. Srinivasan, J. Wang, L. Chen, L. T. Varghese, and A. M. Weiner, Nature Photon. **5**(12), 770–776 (2011).
[60] Z. Jiang, C.-B. Huang, D. E. Leaird, and A. M. Weiner, Nature Photon. **1**(8), 463–467 (2007).
[61] R. K. Shelton, L.-S. Ma, H. C. Kapteyn, M. M. Murnane, J. L. Hall, and J. Ye, Science **293**(5533), 1286–1289 (2001).
[62] T. R. Schibli, J. Kim, O. Kuzucu, J. T. Gopinath, S. N. Tandon, G. S. Petrich, L. A. Kolodziejski, J. G. Fujimoto, E. P. Ippen, and F. X. Kärtner, Opt. Lett. **28**(11), 947–949 (2003).
[63] J. A. Cox, W. P. Putnam, A. Sell, A. Leitenstorfer, and F. X. Kärtner, Opt. Lett. **37**(17), 3579–3581 (2012).
[64] G. Krauss, S. Lohss, T. Hanke, A. Sell, S. Eggert, R. Huber, and A. Leitenstorfer, Nature Photon. **4**(1), 33–36 (2010).
[65] C. Manzoni, S.-W. Huang, G. Cirmi, P. Farinello, J. Moses, F. X. Kärtner, and G. Cerullo, Opt. Lett. **37**(11), 1880–1882 (2012).
[66] S.-W. Huang, G. Cirmi, J. Moses, K.-H. Hong, S. Bhardwaj, J. R. Birge, L. J. Chen, E. Li, B. J. Eggleton, G. Cerullo, and F. X. Kärtner, Nature Photon. **5**(8), 475–479 (2011).
[67] A. Harth, M. Schultze, T. Lang, T. Binhammer, S. Rausch, and U. Morgner, Opt. Express **20**(3), 3076–3081 (2012).
[68] H.-S. Tan, E. Schreiber, and W. S. Warren, Opt. Lett. **27**, 439–441 (2002).
[69] S. Shimizu, Y. Nabekawa, M. Obara, and K. Midorikawa, Optics Express **13**(17), 6345–6353 (2005).
[70] B. E. Schmidt, A. D. Shiner, P. Lassonde, J.-C. Kieffer, P. B. Corkum, D. M. Villeneuve, and F. Légaré, Opt. Express **19**(7), 6858–6864 (2011).
[71] O. E. Martinez, J. P. Gordon, and R. L. Fork, J. Opt. Soc. Am. A **1**(10), 1003–1006 (1984).
[72] R. L. Fork, O. E. Martinez, and J. P. Gordon, Opt. Lett. **9**(5), 150–152 (1984).
[73] A. Shirakawa, I. Sakane, and T. Kobayashi, Opt. Lett. **23**(16), 1292–1294 (1998).
[74] E. B. Treacy, IEEE J. Quantum Electron. **QE-5**, 454–458 (1969).
[75] S. Kane and J. Squier, J. Opt. Soc. Am. B **14**(3), 661–665 (1997).
[76] A. Ricci, A. Jullien, N. Forget, V. Crozatier, P. Tournois, and R. Lopez-Martens, Opt. Lett. **37**(7), 1196–1198 (2012).
[77] R. Szipöcs, C. Spielmann, F. Krausz, and K. Ferencz, Opt. Lett. **19**(3), 201–203 (1994).
[78] F. X. Kärtner, N. Matuschek, T. Schibli, U. Keller, H. A. Haus, C. Heine, R. Morf, V. Scheuer, M. Tilsch, and T. Tschudi, Opt. Lett. **22**(11), 831–833 (1997).
[79] N. Matuschek, F. X. Kärtner, and U. Keller, IEEE J. Quantum Electron. **33**(3), 295–302 (1997).
[80] N. Matuschek, F. X. Kärtner, and U. Keller, IEEE J. Select. Top. Quantum Electron. **4**(2), 197–208 (1998).
[81] N. Matuschek, F. X. Kärtner, and U. Keller, IEEE J. Quantum Electron. **35**(2), 129–137 (1999).
[82] J. R. Birge, F. X. Kärtner, and O. Nohadani, Appl. Opt. **50**(9), C36–C40 (2011).
[83] V. Pervak, Appl. Opt. **50**(9), C55–C61 (2011).
[84] G. Steinmeyer, Appl. Opt. **45**(7), 1484–1490 (2006).
[85] S.-H. Chia, G. Cirmi, S. Fang, G. M. Rossi, O. D. Mücke, and F. X. Kärtner, Optica **1**, 315–322 (2014).
[86] A. M. Weiner, Opt. Commun. **284**(15), 3669–3692 (2011).
[87] A. M. Weiner, Rev. Sci. Instrum. **71**(5), 1929–1960 (2000).
[88] T. Binhammer, E. Rittweger, R. Ell, F. X. Kärtner, and U. Morgner, IEEE J. Quantum Electron. **41**(12), 1552–1557 (2005).
[89] S.-H. Shim, D. B. Strasfeld, and M. T. Zanni, Opt. Express **14**(26), 13120–13130 (2006).
[90] M. A. Dugan, J. X. Tull, and W. S. Warren, J. Opt. Soc. Am. B **14**(9), 2348–2358 (1997).
[91] E. Zeek, K. Maginnis, S. Backus, U. Russek, M. Murnane, G. Mourou, H. Kapteyn, and G. Vdovin, Opt. Lett. **24**(7), 493–495 (1999).
[92] D. Brida, G. Cirmi, C. Manzoni, S. Bonora, P. Villoresi, S. De Silvestri, and G. Cerullo, Opt. Lett. **33**(7), 741–743 (2008).
[93] K.-H. Hong and C. H. Nam, Japn. J. Appl. Phys. **43**(8R), 5289–5293 (2004).
[94] M. Yamashita, K. Yamane, and R. Morita, IEEE J. Select. Top. Quantum Electron. **12**(2), 213–222 (2006).
[95] B. J. Pearson and T. C. Weinacht, Opt. Express **15**(7), 4385–4388 (2007).
[96] S. Bonora, D. Brida, P. Villoresi, and G. Cerullo, Opt. Express **18**(22), 23147–23152 (2010).
[97] J. Garduño-Mejía, A. H. Greenaway, and D. T. Reid, J. Opt. Soc. Am. B **21**(4), 833–843 (2004).
[98] A. Cartella, S. Bonora, M. Först, G. Cerullo, A. Cavalleri, and C. Manzoni, Opt. Lett. **39**(6), 1485–1488 (2014).
[99] P. Tournois, Opt. Commun. **140**(4-6), 245–249 (1997).
[100] F. Verluise, V. Laude, Z. Cheng, C. Spielmann, and P. Tournois, Opt. Lett. **25**(8), 575–577 (2000).
[101] A. Monmayrant, A. Arbouet, B. Girard, B. Chatel, A. Barman, B. J. Whitaker, and D. Kaplan, Appl. Phys. B **81**(2–3), 177–180 (2005).
[102] S. Coudreau, D. Kaplan, and P. Tournois, Opt. Lett. **31**(12), 1899–1901 (2006).
[103] R. Maksimenka, P. Nuernberger, K. F. Lee, A. Bonvalet, J. Milkiewicz, C. Barta, M. Klima, T. Oksenhendler, P. Tournois, D. Kaplan, and M. Joffre, Opt. Lett. **35**(21), 3565–3567 (2010).
[104] L. Veisz, D. Rivas, G. Marcus, X. Gu, D. Cardenas, J. Mikhailova, A. Buck, T. Wittmann, C. M. S. Sears, J. Xu, D. Herrmann, O. Razskazovskaya, V. Pervak, and F. Krausz, Sub-5-fs multi-TW optical parametric synthesizer, in: Conference on Lasers and Electro-Optics Europe and International Quantum Electronics Conference (CLEO EUROPE/IQEC), (European Optical Society, 2013), p. CG_4.
[105] J. Kim, J. Chen, Z. Zhang, F. N. C. Wong, F. X. Kärtner, F. Loehl, and H. Schlarb, Opt. Lett. **32**(9), 1044–1046 (2007).
[106] J. Kim, J. A. Cox, J. Chen, and F. X. Kärtner, Nature Photon. **2**(12), 733–736 (2008).
[107] M. Xin, K. Şafak, M. Y. Peng, P. T. Callahan, and F. X. Kärtner, Opt. Express **22**(12), 14904–14912 (2014).
[108] J. Kim, F. X. Kärtner, and F. Ludwig, Opt. Lett. **31**(24), 3659–3661 (2006).

[109] J. A. Armstrong, N. Bloembergen, J. Ducuing, and P. S. Pershan, Phys. Rev. **127**, 1918–1939 (1962).
[110] G. P. Agrawal, Fiber-Optic Communication Systems, 4th edition (Wiley, 2010).
[111] R. R. Alfano and S. L. Shapiro, Phys. Rev. Lett. **24**, 592–594 (1970).
[112] E. Moon, H. Wang, S. Gilbertson, H. Mashiko, M. Chini, and Z. Chang, Laser Photon. Rev. **4**(1), 160–177 (2010).
[113] C. Li, E. Moon, H. Mashiko, C. M. Nakamura, P. Ranitovic, C. M. Maharjan, C. L. Cocke, Z. Chang, and G. G. Paulus, Opt. Express **14**(23), 11468–11476 (2006).
[114] S. Koke, C. Grebing, H. Frei, A. Anderson, A. Assion, and G. Steinmeyer, Nature Photon. **4**(7), 462–465 (2010).
[115] F. Lücking, A. Assion, A. Apolonski, F. Krausz, and G. Steinmeyer, Opt. Lett. **37**(11), 2076–2078 (2012).
[116] G. Cerullo, A. Baltuška, O. D. Mücke, and C. Vozzi, Laser Photon. Rev. **5**(3), 323–351 (2011).
[117] S. Adachi, P. Kumbhakar, and T. Kobayashi, Opt. Lett. **29**(10), 1150–1152 (2004).
[118] T. Fuji, J. Rauschenberger, A. Apolonski, V. S. Yakovlev, G. Tempea, T. Udem, C. Gohle, T. W. Hänsch, W. Lehnert, M. Scherer, and F. Krausz, Opt. Lett. **30**(3), 332–334 (2005).
[119] T. Fuji, A. Apolonski, and F. Krausz, Opt. Lett. **29**(6), 632–634 (2004).
[120] C. Kübler, R. Huber, S. Tübel, and A. Leitenstorfer, Appl. Phys. Lett. **85**(16), 3360–3362 (2004).
[121] K. Liu, J. Xu, and X.-C. Zhang, Appl. Phys. Lett. **85**(6), 863–865 (2004).
[122] T. Witte, K. L. Kompa, and M. Motzkus, Appl. Phys. B **76**(4), 467–471 (2003).
[123] D. J. Kane and R. Trebino, IEEE J. Quantum Electron. **29**(2), 571–579 (1993).
[124] R. Trebino, K. W. DeLong, D. N. Fittinghoff, J. N. Sweetser, M. A. Krumbügel, B. A. Richman, and D. J. Kane, Rev. Sci. Instrum. **68**(9), 3277–3295 (1997).
[125] R. Trebino, Frequency-Resolved Optical Gating: The Measurement of Ultrashort Laser Pulses (Springer, 2000).
[126] T. Tsang, M. A. Krumbügel, K. W. DeLong, D. N. Fittinghoff, and R. Trebino, Opt. Lett. **21**(17), 1381–1383 (1996).
[127] X. Gu, G. Marcus, Y. Deng, T. Metzger, C. Teisset, N. Ishii, T. Fuji, A. Baltuska, R. Butkus, V. Pervak, H. Ishizuki, T. Taira, T. Kobayashi, R. Kienberger, and F. Krausz, Opt. Express **17**(1), 62–69 (2009).
[128] N. Ishii, K. Kaneshima, K. Kitano, T. Kanai, S. Watanabe, and J. Itatani, Opt. Lett. **37**(20), 4182–4184 (2012).
[129] C. Iaconis and I. A. Walmsley, Opt. Lett. **23**(10), 792–794 (1998).
[130] I. A. Walmsley and C. Dorrer, Adv. Opt. Photon. **1**(2), 308–437 (2009).
[131] J. R. Birge, H. M. Crespo, and F. X. Kärtner, J. Opt. Soc. Am. B **27**(6), 1165–1173 (2010).
[132] E. M. Kosik, A. S. Radunsky, I. A. Walmsley, and C. Dorrer, Opt. Lett. **30**(3), 326–328 (2005).
[133] T. Witting, F. Frank, C. A. Arrell, W. A. Okell, J. P. Marangos, and J. W. G. Tisch, Opt. Lett. **36**(9), 1680–1682 (2011).
[134] J. R. Birge, R. Ell, and F. X. Kärtner, Opt. Lett. **31**(13), 2063–2065 (2006).
[135] R. B. Varillas, A. Candeo, D. Viola, M. Garavelli, S. De Silvestri, G. Cerullo, and C. Manzoni, Opt. Lett. **39**(13), 3849–3852 (2014).
[136] J. Ratner, G. Steinmeyer, T. C. Wong, R. Bartels, and R. Trebino, Opt. Lett. **37**(14), 2874–2876 (2012).
[137] M. Rhodes, M. Mukhopadhyay, J. Birge, G. Steinmeyer, S. Rahaman, and R. Trebino, The coherent artifact in interferometric pulse-measurement techniques, in: CLEO: 2014, (Optical Society of America, 2014), p. SF1E.5.
[138] Z. Chang, Fundamentals of Attosecond Optics (CRC Press, Boca Raton, FL, 2011).
[139] M. T. Hassan, A. Wirth, I. Grguraš, A. Moulet, T. T. Luu, J. Gagnon, V. Pervak, and E. Goulielmakis, Rev. Sci. Instrum. **83**(11), 111301 (2012).
[140] Y. Mairesse and F. Quéré, Phys. Rev. A **71**, 011401 (2005).
[141] J. Gagnon, E. Goulielmakis, and V. Yakovlev, Appl. Phys. B **92**(1), 25–32 (2008).
[142] J. Gagnon and V. S. Yakovlev, Opt. Express **17**(20), 17678–17693 (2009).
[143] M. Chini, S. Gilbertson, S. D. Khan, and Z. Chang, Opt. Express **18**(12), 13006–13016 (2010).
[144] L. Lepetit, G. Chériaux, and M. Joffre, J. Opt. Soc. Am. B **12**(12), 2467–2474 (1995).
[145] A. Baltuška, M. Uiberacker, E. Goulielmakis, R. Kienberger, V. S. Yakovlev, T. Udem, T. W. Hänsch, and F. Krausz, IEEE J. Select. Top. Quantum Electron. **9**(4), 972–989 (2003).
[146] C. Corsi and M. Bellini, Appl. Phys. B **78**(1), 31–34 (2004).
[147] U. Morgner, R. Ell, G. Metzler, T. R. Schibli, F. X. Kärtner, J. G. Fujimoto, H. A. Haus, and E. P. Ippen, Phys. Rev. Lett. **86**, 5462–5465 (2001).
[148] T. M. Fortier, D. J. Jones, and S. T. Cundiff, Opt. Lett. **28**(22), 2198–2200 (2003).
[149] L. Matos, D. Kleppner, O. Kuzucu, T. R. Schibli, J. Kim, E. P. Ippen, and F. X. Kaertner, Opt. Lett. **29**(14), 1683–1685 (2004).
[150] O. D. Mücke, R. Ell, A. Winter, J.-W. Kim, J. R. Birge, L. Matos, and F. Kärtner, Opt. Express **13**(13), 5163–5169 (2005).
[151] C. Feng, J.-F. Hergott, P.-M. Paul, X. Chen, O. Tcherbakoff, M. Comte, O. Gobert, M. Reduzzi, F. Calegari, C. Manzoni, M. Nisoli, and G. Sansone, Opt. Express **21**(21), 25248–25256 (2013).
[152] M. Kakehata, H. Takada, Y. Kobayashi, K. Torizuka, Y. Fujihira, T. Homma, and H. Takahashi, Opt. Lett. **26**(18), 1436–1438 (2001).
[153] K.-H. Hong, J. Lee, B. Hou, J. A. Nees, E. Power, and G. A. Mourou, Appl. Phys. Lett. **89**(3), 031113 (2006).
[154] C. Li, E. Moon, H. Mashiko, H. Wang, C. M. Nakamura, J. Tackett, and Z. Chang, Appl. Opt. **48**(7), 1303–1307 (2009).
[155] H. Wang, M. Chini, E. Moon, H. Mashiko, C. Li, and Z. Chang, Opt. Express **17**(14), 12082–12089 (2009).
[156] B. E. Schmidt, N. Thiré, M. Boivin, A. Laramée, F. Poitras, G. Lebrun, T. Ozaki, H. Ibrahim, and F. Légaré, Nature Commun. **5**, 3643 (2014).

[157] T. R. Schibli, O. Kuzucu, J.-W. Kim, E. P. Ippen, J. G. Fujimoto, F. X. Kärtner, V. Scheuer, and G. Angelow, IEEE J. Select. Top. Quantum Electron. **9**(4), 990–1001 (2003).
[158] L. J. Chen, M. Y. Sander, and F. X. Kärtner, Opt. Lett. **35**(17), 2916–2918 (2010).
[159] U. Morgner, F. X. Kärtner, S. H. Cho, Y. Chen, H. A. Haus, J. G. Fujimoto, E. P. Ippen, V. Scheuer, G. Angelow, and T. Tschudi, Opt. Lett. **24**(6), 411–413 (1999).
[160] A. Sell, G. Krauss, R. Scheu, R. Huber, and A. Leitenstorfer, Opt. Express **17**(2), 1070–1077 (2009).
[161] J.-W. Kim, Master thesis, Massachusetts Institute of Technology (USA) (2004).
[162] A. J. Benedick, J. G. Fujimoto, and F. X. Kärtner, Nature Photon. **6**(2), 97–100 (2012).
[163] H. A. Haus, K. Tamura, L. E. Nelson, and E. P. Ippen, IEEE J. Quantum Electron. **31**(3), 591–598 (1995).
[164] J. A. Cox, A. H. Nejadmalayeri, J. Kim, and F. X. Kärtner, Opt. Lett. **35**(20), 3522–3524 (2010).
[165] J. Kim, J. Chen, J. Cox, and F. X. Kärtner, Opt. Lett. **32**(24), 3519–3521 (2007).
[166] M. Y. Sander, E. P. Ippen, and F. X. Kärtner, Opt. Express **18**(5), 4948–4960 (2010).
[167] F. Adler, A. Sell, F. Sotier, R. Huber, and A. Leitenstorfer, Opt. Lett. **32**, 3504–3506 (2007).
[168] A. Baltuška, M. S. Pshenichnikov, and D. A. Wiersma, IEEE J. Quantum Electron. **35**(4), 459–478 (1999).
[169] P. Hommelhoff, Y. Sortais, A. Aghajani-Talesh, and M. A. Kasevich, Phys. Rev. Lett. **96**, 077401 (2006).
[170] O. D. Mücke, T. Tritschler, M. Wegener, U. Morgner, and F. X. Kärtner, Phys. Rev. Lett. **89**, 127401 (2002).
[171] E. Goulielmakis, V. S. Yakovlev, A. L. Cavalieri, M. Uiberacker, V. Pervak, A. Apolonski, R. Kienberger, U. Kleineberg, and F. Krausz, Science **317**(5839), 769–775 (2007).
[172] J. N. Sweetser, D. N. Fittinghoff, and R. Trebino, Opt. Lett. **22**(8), 519–521 (1997).
[173] R. Kienberger, E. Goulielmakis, M. Uiberacker, A. Baltuska, V. Yakovlev, F. Bammer, A. Scrinzi, T. Westerwalbesloh, U. Kleineberg, U. Heinzmann, M. Drescher, and F. Krausz, Nature **427**(6977), 817–821 (2004).
[174] Q. Wu and X.-C. Zhang, Appl. Phys. Lett. **71**(10), 1285–1286 (1997).
[175] T. T. Luu, M. T. Hassan, A. Moulet, O. Razskazovskaya, N. Kaprowicz, V. Pervak, F. Krausz, and E. Goulielmakis, Isolated optical attosecond pulses, in: CLEO: 2013, (Optical Society of America, 2013), p. QF1C.6.
[176] E. Matsubara, K. Yamane, T. Sekikawa, and M. Yamashita, J. Opt. Soc. Am. B **24**(4), 985–989 (2007).
[177] S. Fang, H. Ye, G. Cirmi, S.-H. Chia, S. Carbajo, O. D. Mücke, and F. X. Kärtner, High-energy carrier-envelope phase-stable optical waveforms compressible to <1 fs using induced-phase modulation in argon-filled hollow-core fiber, in: Research in Optical Sciences, (Optical Society of America, 2014), p. HW1C.2.
[178] S. Fang, H. Ye, G. Cirmi, G. M. Rossi, S.-H. Chia, O. D. Mücke, and F. X. Kärtner, Above-millijoule optical waveforms compressible to sub-fs using induced-phase modulation in a neon-filled hollow-core fiber, in: Ultrafast Phenomena, (Optical Society of America, 2014), p. 09.Wed.P3.60.
[179] S. Fang, K. Yamane, J. Zhu, C. Zhou, Z. Zhang, and M. Yamashita, IEEE Photon. Technol. Lett. **23**(11), 688–690 (2011).
[180] T. Tanigawa, Y. Sakakibara, S. Fang, T. Sekikawa, and M. Yamashita, Opt. Lett. **34**(11), 1696–1698 (2009).
[181] K. Yamane, M. Katayose, and M. Yamashita, IEEE Photon. Technol. Lett. **23**(16), 1130–1132 (2011).
[182] A. Dubietis, R. Butkus, and A. P. Piskarskas, IEEE J. Select. Top. Quantum Electron. **12**(2), 163–172 (2006).
[183] S. Witte and K. S. E. Eikema, IEEE J. Select. Top. Quantum Electron. **18**(1), 296–307 (2012).
[184] S.-W. Huang, G. Cirmi, J. Moses, K.-H. Hong, S. Bhardwaj, J. R. Birge, L.-J. Chen, I. V. Kabakova, E. Li, B. J. Eggleton, G. Cerullo, and F. X. Kärtner, J. Phys. B **45**(7), 074009 (2012).
[185] T. Fuji, N. Ishii, C. Y. Teisset, X. Gu, T. Metzger, A. Baltuška, N. Forget, D. Kaplan, A. Galvanauskas, and F. Krausz, Opt. Lett. **31**(8), 1103–1105 (2006).
[186] J. Moses, S.-W. Huang, K.-H. Hong, O. D. Mücke, E. L. Falcão-Filho, A. Benedick, F. Ö. Ilday, A. Dergachev, J. A. Bolger, B. J. Eggleton, and F. X. Kärtner, Opt. Lett. **34**(11), 1639–1641 (2009).
[187] S. Witte, R. Th. Zinkstok, W. Hogervorst, and K. S. E. Eikema, Opt. Express **13**(13), 4903–4908 (2005).
[188] N. Ishii, L. Turi, V. S. Yakovlev, T. Fuji, F. Krausz, A. Baltuška, R. Butkus, G. Veitas, V. Smilgevičus, R. Danielius, and A. Piskarskas, Opt. Lett. **30**(5), 567–569 (2005).
[189] S. Adachi, N. Ishii, T. Kanai, A. Kosuge, J. Itatani, Y. Kobayashi, D. Yoshitomi, K. Torizuka, and S. Watanabe, Opt. Express **16**(19), 14341–14352 (2008).
[190] D. Herrmann, L. Veisz, R. Tautz, F. Tavella, K. Schmid, V. Pervak, and F. Krausz, Opt. Lett. **34**(16), 2459–2461 (2009).
[191] G. Cerullo and S. De Silvestri, Rev. Sci. Instrum. **74**(1), 1–18 (2003).
[192] A. M. Siddiqui, G. Cirmi, D. Brida, F. X. Kärtner, and G. Cerullo, Opt. Lett. **34**(22), 3592–3594 (2009).
[193] M. Bradler and E. Riedle, Opt. Lett. **39**(9), 2588–2591 (2014).
[194] R. A. Kaindl, M. Wurm, K. Reimann, P. Hamm, A. M. Weiner, and M. Woerner, J. Opt. Soc. Am. B **17**(12), 2086–2094 (2000).
[195] A. Baltuška, T. Fuji, and T. Kobayashi, Phys. Rev. Lett. **88**, 133901 (2002).
[196] G. Cirmi, C. Manzoni, D. Brida, S. De Silvestri, and G. Cerullo, J. Opt. Soc. Am. B **25**(7), B62–B69 (2008).
[197] M. Zavelani-Rossi, G. Cerullo, S. De Silvestri, L. Gallmann, N. Matuschek, G. Steinmeyer, U. Keller, G. Angelow, V. Scheuer, and T. Tschudi, Opt. Lett. **26**(15), 1155–1157 (2001).
[198] M. B. Danailov and I. P. Christov, Opt. Commun. **77**(5-6), 397–401 (1990).
[199] J. Faure, J. Itatani, S. Biswal, G. Chériaux, L. R. Bruner, G. C. Templeton, and G. Mourou, Opt. Commun. **159**(1-3), 68–73 (1999).
[200] C. P. Hauri, M. Bruck, W. Kornelis, J. Biegert, and U. Keller, Opt. Lett. **29**(2), 201–203 (2004).

[201] N. B. Chichkov, U. Bünting, D. Wandt, U. Morgner, J. Neumann, and D. Kracht, Opt. Express **17**(26), 24075–24083 (2009).
[202] A. M. Weiner, Progr. Quantum Electron. **19**(3), 161–237 (1995).
[203] I. Powell, Appl. Opt. **26**(17), 3705–3709 (1987).
[204] M. Schultze, T. Binhammer, A. Steinmann, G. Palmer, M. Emons, and U. Morgner, Opt. Express **18**(3), 2836–2841 (2010).
[205] S. Watanabe, K. Kondo, Y. Nabekawa, A. Sagisaka, and Y. Kobayashi, Phys. Rev. Lett. **73**, 2692–2695 (1994).
[206] F. Ehlotzky, Phys. Rep. **345**(4), 175–264 (2001).
[207] C. Vozzi, F. Calegari, F. Frassetto, L. Poletto, G. Sansone, P. Villoresi, M. Nisoli, S. De Silvestri, and S. Stagira, Phys. Rev. A **79**, 033842 (2009).
[208] T. Balčiūnas, O. D. Mücke, P. Mišeikis, G. Andriukaitis, A. Pugžlys, L. Giniūnas, R. Danielius, R. Holzwarth, and A. Baltuška, Opt. Lett. **36**(16), 3242–3244 (2011).
[209] I J. Kim, C. M. Kim, H. T. Kim, G. H. Lee, Y. S. Lee, J. Y. Park, D. J. Cho, and C. H. Nam, Phys. Rev. Lett. **94**, 243901 (2005).
[210] T. Metzger, A. Schwarz, C. Y. Teisset, D. Sutter, A. Killi, R. Kienberger, and F. Krausz, Opt. Lett. **34**(14), 2123–2125 (2009).
[211] Y. Deng, A. Schwarz, H. Fattahi, M. Ueffing, X. Gu, M. Ossiander, T. Metzger, V. Pervak, H. Ishizuki, T. Taira, T. Kobayashi, G. Marcus, F. Krausz, R. Kienberger, and N. Karpowicz, Opt. Lett. **37**(23), 4973–4975 (2012).
[212] C. Y. Teisset, M. Schultze, R. Bessing, M. Häfner, J. Rauschenberger, D. Sutter, and T. Metzger, Picosecond thin-disk regenerative amplifier with high average power for pumping optical parametric amplifiers, in: CLEO: 2013, (Optical Society of America, 2013), p. CTh5C.6.
[213] M. Chyla, T. Miura, M. Smrz, H. Jelinkova, A. Endo, and T. Mocek, Opt. Lett. **39**(6), 1441–1444 (2014).
[214] P. Russbueldt, T. Mans, G. Rotarius, J. Weitenberg, H. D. Hoffmann, and R. Poprawe, Opt. Express **17**(15), 12230–12245 (2009).
[215] M. Pergament, M. Kellert, K. Kruse, J. Wang, G. Palmer, L. Wissmann, U. Wegner, and M. J. Lederer, Opt. Express **22**(18), 22202–22210 (2014).
[216] K.-H. Hong, J. T. Gopinath, D. Rand, A. M. Siddiqui, S.-W. Huang, E. Li, B. J. Eggleton, J. D. Hybl, T. Y. Fan, and F. X. Kärtner, Opt. Lett. **35**(11), 1752–1754 (2010).
[217] K.-H. Hong, S.-W. Huang, J. Moses, X. Fu, C.-J. Lai, G. Cirmi, A. Sell, E. Granados, P. Keathley, and F. X. Kärtner, Opt. Express **19**(16), 15538–15548 (2011).
[218] K.-H. Hong, C.-J. Lai, J. P. Siqueira, P. Krogen, J. Moses, C. L. Chang, G. J. Stein, L. E. Zapata, and F. X. Kärtner, Opt. Lett. **39**(11), 3145–3148 (2014).
[219] X. Fu, K.-H. Hong, L. J. Chen, and F. X. Kärtner, J. Opt. Soc. Am. B **30**(11), 2798–2809 (2013).
[220] K.-H. Hong, C.-J. Lai, V. M. Gkortsas, S.-W. Huang, J. Moses, E. Granados, S. Bhardwaj, and F. X. Kärtner, Phys. Rev. A **86**, 043412 (2012).
[221] G. Cirmi, S. Fang, S.-H. Chia, O. D. Mücke, F. X. Kärtner, C. Manzoni, P. Farinello, and G. Cerullo, Towards parametric synthesis of millijoule-level two-octave-wide optical waveforms for strong-field experiments, in: Ultrafast Optics (Switzerland, 2013), p. We3.3.
[222] S. Fang, G. Cirmi, S.-H. Chia, O. D. Mücke, F. X. Kärtner, C. Manzoni, P. Farinello, and G. Cerullo, Multi-mJ parametric synthesizer generating two-octave-wide optical waveforms, in: 2013 Pacific Rim Conference on Lasers and Electro-Optics, (Optical Society of America, 2013), p. WB3-1.
[223] O. D. Mücke, S. Fang, G. Cirmi, S.-H. Chia, F. X. Kärtner, C. Manzoni, P. Farinello, and G. Cerullo, Millijoule-level parametric synthesizer generating two-octave-wide optical waveforms for strong-field experiments, in: CLEO: 2013, (Optical Society of America, 2013), p. CTh3H.3.
[224] H. Fattahi, H. G. Barros, M. Gorjan, T. Nubbemeyer, B. Alsaif, C. Y. Teisset, M. Schultze, S. Prinz, M. Haefner, M. Ueffing, A. Alismail, L. Vámos, A. Schwarz, O. Pronin, J. Brons, X. T. Geng, G. Arisholm, M. Ciappina, V. S. Yakovlev, D.-E. Kim, A. M. Azzeer, N. Karpowicz, D. Sutter, Z. Major, T. Metzger, and F. Krausz, Optica **1**(1), 45–63 (2014).
[225] M. Schulz, R. Riedel, A. Willner, T. Mans, C. Schnitzler, P. Russbueldt, J. Dolkemeyer, E. Seise, T. Gottschall, S. Hädrich, S. Duesterer, H. Schlarb, J. Feldhaus, J. Limpert, B. Faatz, A. Tünnermann, J. Rossbach, M. Drescher, and F. Tavella, Opt. Lett. **36**(13), 2456–2458 (2011).
[226] M. Meckel, D. Comtois, D. Zeidler, A. Staudte, D. Pavičić, H. C. Bandulet, H. Pépin, J. C. Kieffer, R. Dörner, D. M. Villeneuve, and P. B. Corkum, Science **320**(5882), 1478–1482 (2008).
[227] C. I. Blaga, J. Xu, A. D. DiChiara, E. Sistrunk, K. Zhang, P. Agostini, T. A. Miller, L. F. DiMauro, and C. D. Lin, Nature **483**(7388), 194–197 (2012).
[228] M. Meckel, A. Staudte, S. Patchkovskii, D. M. Villeneuve, P. B. Corkum, R. Dörner, and M. Spanner, Nature Phys. **10**, 594–600 (2014).
[229] L. J. Wong and F. X. Kärtner, Opt. Lett. **36**(6), 957–959 (2011).
[230] M. Gulde, S. Schweda, G. Storeck, M. Maiti, H. K. Yu, A. M. Wodtke, S. Schäfer, and C. Ropers, Science **345**(6193), 200–204 (2014).